Effects of magnetic field, doping and local strain on excitons in two-dimensional semiconductors

Jonathan Förste

München 2024

Effects of magnetic field, doping and local strain on excitons in two-dimensional semiconductors

Jonathan Förste

Dissertation
der Fakultät für Physik
der Ludwig-Maximilians-Universität
München

vorgelegt von
Jonathan Förste
aus Potsdam

München, den 07.05.2024

Erstgutachter: Prof. Dr. Alexander Högele
Zweitgutachter: Prof. Dr. Achim Hartschuh
Tag der mündlichen Prüfung: 12.07.2024

Zusammenfassung

Zweidimensionale Materialien sind Nanostrukturen, die aus wenigen Lagen geschichteter Materialien hergestellt werden. Eine wichtige Untergruppe stellen halbleitende Übergangsmetalldichalkogenide dar, die im Extremfall einer Einzellage einen Übergang zu einem direkten Halbleiter erfahren. Diese Materialien zeigen mehrere einzigartige optische Eigenschaften wie starke Licht-Materie-Wechselwirkung, stark gebundene Exzitonen und zirkularen Dichroismus.

In dieser Arbeit wurden Einzel- und Doppellagen aus Wolframdiselenid und Wolframdisulfid mithilfe optischer Spektroskopie untersucht. Zunächst wurde das Spektrum einer ladungsdurchstimmbaren Einzel- und Doppellage aus Wolframdiselenid im Magnetfeld untersucht um deren Spektrallinien im neutralen und negativ geladenen Regime durch ihre charakteristische Aufsspaltung zu charakterisieren. Diese wurde mit einem theoretischen Modell auf Basis von Dichtefunktionaltheorie verglichen, welches es erreicht, die magnetische Verschiebung innerhalb der gesamten Bandstruktur zu berechnen. Die numerischen Berechnungen zeigen exzellente quantitative Übereinstimmung mit vorangegangenen Studien und erweitern diese um Vorhersagen für impulsindirekte Exzitonen. Anschließend wurden diese Erkenntnisse angewandt um das Spektrum von einzellagigem Wolframdisulfid zu untersuchen welches in eine Feldeffektstruktur aus Graphen eingebettet wurde. Dadurch wurde es erreicht, sowohl negative als auch positive Ladungsträgerkonzentrationen zu induzieren. Es wurde gezeigt, dass das Spektrum sich unter Berücksichtigung der größeren Bandlücke analog zu dem von Wolframdiselenid verhält.

Zuletzt wurde das Verhalten einer freitragenden Einzellage aus Wolframdiselenid unter lokalen Verspannungen untersucht. Mithilfe eines kryogenen Rasterkraftmikroskops, bestehend aus einer Quarzstimmgabel und einer daran befestigten transparenten Diamandspitze, wurde es erreicht, in Echtzeit unter punktueller Krafteinwirkung das Photolumineszenzspektrum zu vermessen. Es zeigte sich, dass unter lokaler Einwirkung der Spitze das Spektrum eine Rotverschiebung erfährt, die für Zugverspannung charakteristisch ist. Bei hoher Verschiebung wurde eine Aufhellung dunkler Exzitonen durch Hybridisierung von dunklen Exzitonen mit lokalisierten Zuständen be-

obachtet. Bei noch höherer Krafteinwirkung verursachte die Spitze eine spontane und permanente Verformung der Probenstruktur, während das Spektrum in eine Gruppe schmaler, hell leuchtender Spektrallinien zerfiel, die auch nach Beendigung der Krafteinwirkung sichtbar blieben.

Abstract

Two-dimensional materials are nanostructures that consist of atomically thin sheets of layered materials. An important subgroup are semiconducting transition metal dichalcogenides, which in the limit of a single layer exhibit a transition from an indirect to a direct band gap. These materials show multiple unique optical properties such as a strong light-matter interaction, strongly bound excitons and circular dichroism.

In this thesis, mono- and bilayers of tungsten diselenide and tungsten disulfide were studied using optical spectroscopy. First, the spectrum of a charge tunable mono- and bilayer of tungsten diselenide was studied in magnetic field to characterize the exciton spectral lines in the neutral and negatively charged regime. These measurements were complemented by a theoretical model based on density functional theory, which is able to calculate the magnetic shift throughout the Brillouin zone. These numerical calculations showed excellent quantitative agreement with previous reports and extend those models by providing predictions for momentum-indirect excitons. Next, these findings were used to study the spectrum of monolayer tungsten disulfide. A sample was embedded in a field effect structure made from graphene, which achieved negative, neutral as well as positive charge carrier concentrations. It was shown, that apart from a shift in the band gap energy, the exciton spectrum can be described analogously to tungsten diselenide.

Finally, the behavior of a suspended monolayer of tungsten diselenide was studied under local strain. Using a low temperature atomic force microscope based on a quartz tuning fork with a transparent diamond tip, real-time measurement of the photoluminescence spectrum at simultaneous application of local force was achieved. It was shown that under local action of the tip the spectrum exhibits a redshift, characteristic for tensile strain. At high force, the brightening of dark excitons through the hybridization of dark excitons with localized states was observed. At even higher force, the tip caused a spontaneous and permanent deformation of the sample structure while the spectrum changed to a set of narrow, bright spectral lines, some of which remained present after release of the tip.

Contents

1 Introduction

"*The interface is the device*".

This famous statement from Herbert Kroemers Nobel lecture [1] illustrates how interesting effects in heterostructures often happen within the nanoscopically thin transition region between different materials. This is especially true for two-dimensional (2D) materials, sheets of layered or van der Waals materials as thin as a single atom. Similar to the interfaces of conventional heterostructures, 2D materials show remarkable properties, which are absent in their bulk counterparts. The first 2D material to be studied in detail was graphene, an atomically thin sheet of graphite [2, 3]. In graphene, the formation of the so-called dirac cones at the inequivalent K and K' points at the edge of the Brillouin zone leads to a plethora of interesting effects, including super high carrier mobility [2] and the fractional quantum hall effect [4]. Another major group of 2D materials are semiconducting transition metal dichalcogenides (TMDs), primarily sulfides and selenides of tungsten and molybdenum. Similar to graphite, bulk TMDs were well known before the emergence of their thin film counterparts. Molybednum disulfide (MoS_2), which is found in nature as the mineral molybdenite [5, 6] has long been used as a lubricant [7] and was studied for its potential to be used in solar cells [8, 9]. Remarkably however, MoS_2 as well as the similar materials $MoSe_2$, WSe_2 and WS_2 were found to exhibit a transition from an indirect [10, 11] to a direct band gap [12–14] in the limit of a single monolayer resulting in significantly altered optical properties. First, this results in strongly enhanced photoluminescence (PL) [12]. Next, due to reduced dielectric screening in two dimensions, 2D TMDs exhibit a very large exciton binding energy [15, 16], which results in excitons dominating the optical response even at room temperature. Further, a lack of inversion symmetry leads to different optical selection rules for different crystal momenta.The band minima at K/K'-points (the K/K'-valleys) at the Brillouin zone edge are thus selectively addressed with circularly polarized light of opposite helicity. Strong spin-orbit coupling in the heavy transition metal atoms further couples this valley degree of freedom to the spin, enabling its optical control and the potential application in so-called valleytronic devices [17, 18].

A special feature TMDs and other 2D materials is the ability to mechanically assemble complex van-der-Waals heterostructures by stacking monolayers of different materials on top of each other [19]. This enables the combination of materials with different properties such as magnets, metals, semiconductors or superconductors within one heterostructure.

This thesis focusses on the optical study of tungsten-based TMD mono- and bilayers. In contrast to molybdenum based TMDs, WSe_2 and WS_2 exhibit a reversed energetic ordering in the spin-polarized sub bands of the conduction band [20, 21]. As a result, dark excitons, whose radiative recombination is suppressed by a mismatch in spin or momentum, are energetically favored and the PL spectrum shows a rich and complex substructure [21]. The spectrum is further sensitive to magnetic fields, charge carrier density and strain, motivating the experiments performed in this thesis.

Scope of this thesis

The thesis is structured as follows: Chapter 2 discusses fundamentals of TMD mono- and bilayers. In the first part, the crystal structure and the resulting band structure is described with a focus on optical properties and excitons. This is followed by a summary of the influence of strain on the band structure which is first discussed from a theoretical perspective followed by a review of relevant experimental studies. Finally, the influence of magnetic field on excitons in WSe_2 is discussed in detail and a numerical model based on density functional theory (DFT) is introduced which was used to provide a quantitative interpretation of the spectrum later on.

Chapter 3 describes experimental methods used in subsequent experiments. First, methods to fabricate van der Waals heterostructures based on 2D materials are introduced, including mechanical exfoliation, optical determination of layer number of TMDs and graphene, control of interface quality, heterostructure assembly using temperature controlled viscoelastic stamping as well as electronic control of the doping level. This is followed by a description of confocal microscopy at low temperature and relevant modifications to allow concurrent optical spectroscopy and atomic force microscopy (AFM). Finally, fundamentals of quartz tuning fork (QTF) AFM are presented followed by technical details on its implementation for experiments in this thesis.

Chapter 4 describes experimental results on charge-controlled tungsten based dichalcogenides. In the first experiment, the magnetic splitting of spectral lines in WSe_2 mono- and bilayers is measured for both neutral and negative charge carrier densities and quantified by the exciton g-factor. These results are compared to the previously dis-

cussed DFT model. Subsequently, results from the study of charge controlled WS_2 are shown. The use of a gate based on few layer graphene allows an increased dynamic range, achieving positive as well as strong negative doping. These results show broad agreement with the data from WSe_2 when the energy shift due to a different band gap is taken into account.

Chapter 5 describes tip-assisted spectroscopy of a suspended WSe_2 monolayer. In this experiment, a transparent diamond tip mounted to a QTF is used to apply force to the sample to study the optical behavior under local strain. This includes tensile strain, showing a characteristic and reversible red shift of the PL spectrum as well as inelastic deformation that leads to the creation of bright, localized emitters.

2 Fundamentals of few-layer transition metal dichalcogenides

This chapter discusses the theoretical foundations and relevant background on the optical behavior of two-dimensional transition metal dichalcogenides. First, an overview of the crystal structure and resulting electronic band structure is given, including a brief discussion of exciton and valley physics. This is followed by a discussion on the influence of strain and magnetic field on those optical properties.

2.1 Crystal structure and symmetries

Group-VI transition metal dichalcogenides (TMDs) are so-called layered or van der Waals materials that are covalently bound in-plane while being held together out-of-plane by weak van der Waals forces. Crystals of TMDs form a tri-atomic base, consisting of one transition metal atom like tungsten (W) or molybdenum (Mo), and two chalcogen atoms such as sulfur (S) or selenium (Se). While there are several possible crystalline phases, the stable 2H-phase is of main interest. In this phase, every transition metal atom has six neighboring chalcogen atoms that arrange into a trigonal prismatic unit cell with the metal atom in the center, forming a hexagonal lattice structure in-plane (see Fig. 2.1a,b). A TMD monolayer exhibits $\mathcal{D}_{3h}^{1}$-symmetry which corresponds to invariance under threefold rotation and in-plane reflection. The difference to a monoatomic, hexagonal material like graphene is a broken inversion symmetry. When inverting the unit cell with the metal atom as the inversion center, all chalcogen atoms occupy previously empty locations with consequences for optical and electronic properties as discussed below. This broken symmetry is restored when adding a second layer to form a bilayer. TMDs that are not S/Se-based can show different phases of interest. The hexagonal lattice in WTe_2, for example is strongly distorted, resulting in unique electronic and magnetic properties [22]. Unless otherwise indicated, this thesis refers to the four semiconducting TMDs WS_2, WSe_2, MoS_2 and $MoSe_2$.

2.2 Electronic band structure and optical properties

TMDs are semiconductors. In bulk, all TMDs show an indirect band gap [11]. As the material thins, this gap widens because of quantum confinement in the out-of-plane direction [23]. Finally, in the monolayer limit, it widens enough such that the maximum of the valence band and minimum of the conduction band both shift to the corners of the hexagonal Brillouin zone at the K-point, forming a direct band gap [12, 13]. This has important consequences for the optical properties of TMDs. As a direct band gap facilitates efficient and fast radiative recombination [24], direct band gap semiconductors generally exhibit strong optical absorption [25, 26] and photoluminescence [24], increasing their potential use-cases in both scientific studies and practical applications as it pertains to optics and photonics [26–29]. Apart from the widening band gap, the 2D confinement also has an effect on the Coulomb interaction between electrons and holes and thus the formation of bound electron-hole pairs, so-called excitons. An exciton is understood analogous to a hydrogen atom, with a hole in place of a proton and parameters adjusted for the effective masses of the charges as well as their dielectric environment. In case of bulk material, the exciton binding energy behaves analogously to the Rydberg series of the 3D hydrogen atom [30] and reads:

$$E_{X,3\mathrm{D}}(n) = -\frac{\mu \mathrm{Ry}}{m_0 \epsilon_r^2} \frac{1}{n^2} \equiv -\frac{R_X}{n^2}, \tag{2.1}$$

with the reduced mass $\mu = (m_e^* m_h^*)/(m_e^* + m_h^*)$, relative permittivity ϵ_r, electron mass m_0 and Rydberg energy Ry. However, this relation changes in low-dimensional systems. In a TMD monolayer, it is a good first approximation to assume an ideal two-dimensional system with the binding energy of a 2D hydrogen atom given by [31]:

$$E_{X,2\mathrm{D}}(n) = -\frac{R_X}{(n - 1/2)^2}. \tag{2.2}$$

For the ground state with $n = 1$, Eq. 2.2 predicts a fourfold increase in exciton binding energy. However, this does not yet include contributions from the dielectric environment. As the electric field of a 2D exciton in a real material still extends in three dimensions, a big portion of the field lines will extend into the environment of the TMD. As the relative permittivity of TMDs [15, 33] is typically much higher than that of the sample environment such as air, vacuum, SiO_2 [34] or hBN [35], this results in a decrease in dielectric screening between electron and hole. This leads to a another enhancement of the exciton binding energy [15], which rises from ~ 50 meV

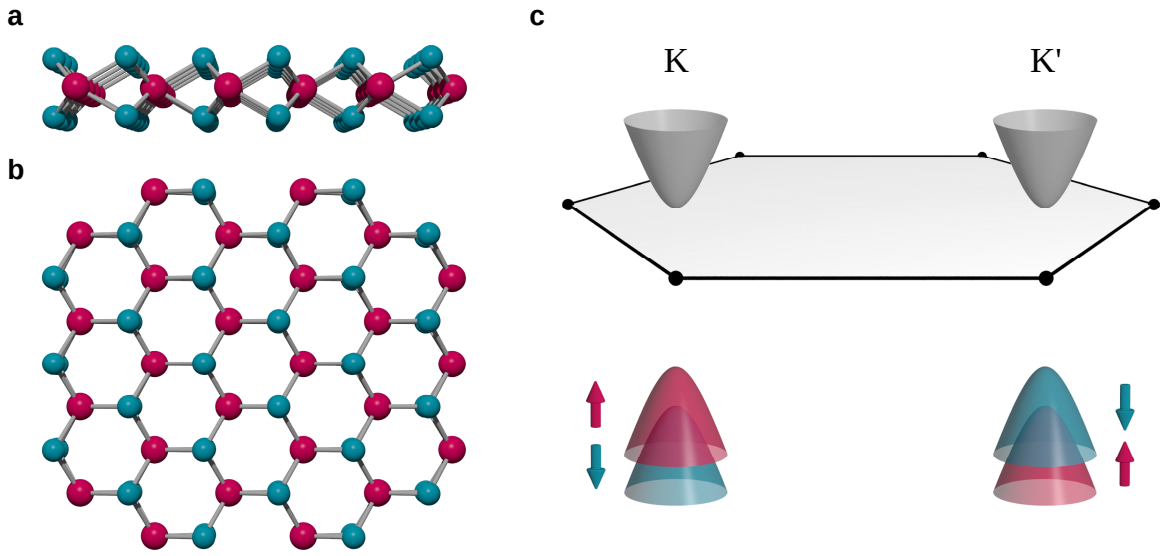

Figure 2.1 Crystal structure of monolayer TMDs. **a, b** Schematic of the real space crystal structure of a transition metal dichalcogenide monolayer in side (a) and top (b) view, consisting of one layer of transition metal atoms (red) inbetween two layers of chalcogen atoms (turquoise). **c,** Schematic of the first Brillouin zone with hyperbolic band dispersions at the K and K' symmetry points and strong spin-orbit splitting indicated in the valence band resulting in spin polarization. Figure adapted from [32].

in bulk up to $\sim$ 600 meV for a $MoSe_2$ monolayer with a similar order of magnitude being observed in other TMDs [36]. Also, as the portion of field lines extending into the environment grows with higher n and thus higher exciton radius, the dielectric enhancement of the exciton binding energy does not perfectly follow the curve of a 2D hydrogen atom but rather converges towards it with increasing values of n, where corrections due to ϵ_r of the TMD sheet become less relevant [15]. As a result of the enhanced binding energy, the optical response of TMDs is dominated by excitonic effects, which remain the primary radiative pathway until well above room temperature ($k_B T \sim 25$ meV). For comparison, GaAs, another direct band gap semiconductor, shows an exciton binding energy of only 4.2 meV [37], limiting excitonic processes to cryogenic temperatures. Another property of monolayer TMDs derives from their valley properties. Unlike in most conventional direct band gap semiconductors, the band gap of TMD monolayers is located at the edges of the Brillouin zone at the six inequivalent K (K') valleys. This gives band edge electrons and holes an additional degree of freedom through their crystal momentum k to be manipulated, similar to charge or spin in electronics or spintronics [40]. However, this idea did not originate in the context of TMDs but was already explored in graphene. It was proposed to ad-

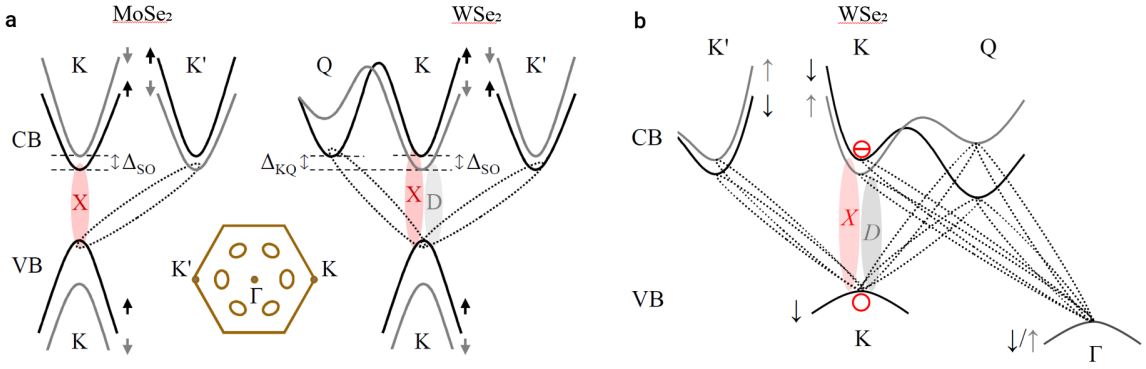

Figure 2.2 Exciton species in monolayer and bilayer TMDs. a, Band diagram of monolayer $MoSe_2$ (left) and WSe_2 (right) with inset showing high-symmetry points K, K' and Γ, as well as six inequivalent Q-points. Conduction band (CB) and valence band (VB) are shown with spin-up and spin-down electron sub-bands (shown in black and grey, respectively), spin-orbit splitting Δ_{SO}, and the energy separation Δ_{KQ} between the conduction band minima at K and Q. Momentum-direct spin-bright and spin-forbidden excitons (X and D, indicated by ellipses shaded in red and grey) are formed by electrons and unoccupied states in the K-valley. Momentum-dark excitons (dashed ellipses) with the empty state at K are formed with electrons at Q or K'. Figure adapted from [38]. **b,** Band diagram of the conduction (CB) and the valence bands (VB) of bilayer WSe_2. Zero-momentum spin-bright (X) and spin-dark (D) excitons are formed in the K valley by electrons from spin-up and spin-down conduction subbands indicated in black and gray, respectively, paired with a spin-up valence band empty state. Momentum-indirect excitons with electrons and unoccupied states in dissimilar valleys are indicated by dashed ellipses. Figure adapted from [39].

dress the k degree of freedom in graphene through valley-selective circular dichroism [41], which would allow optical control of the valley, creating a valleytronic device. However, this is incompatible with inversion symmetry, which is naturally present in graphene, leading to efforts to build devices and configurations to artificially break this symmetry [42, 43]. As explained in section 2.1, inversion symmetry is explicitly broken in TMD monolayers, which naturally leads to valley-contrasting optical selection rules [44–48], circular dichroism (see Fig. 2.1c) as well as strong non-linear effects such as second harmonic generation [49–52].

The valence and conduction bands of TMDs are dominated by the d-orbitals of the transition metal atoms, and therefore exhibit sizeable spin-orbit coupling [53, 54]. As the resulting energy shift in the spin-polarized subbands is reversed between K and K' valleys, the k degree of freedom is coupled to the spin [46]. When looking at interband transitions within one valley, this leaves four potential pathways for the radiative re-

combination of excitons, each involving one subband of valence and conduction band with a parallel or anti-parallel spin-component. As it turns out, only spin-parallel transitions are allowed in the out-of-plane direction, leaving two primary transitions, named A and B exciton by their energetic ordering . The energetically lower A exciton with parallel spin is called "bright" (typically denoted X or X_0), as it is observed through radiative recombination, while an exciton with an electron in the opposite spin conduction subband is called (spin) dark or gray (denoted X_D or D^0). The word "gray" refers to the fact, that this transition couples to light with z-polarization i.e. radiates in-plane [55] or by relaxing the optical selection rules through magnetic fields [21, 56]. The energetic ordering of bright and dark exciton states has a decisive influence on the spectrum (see Fig. 2.2a). In Mo-based TMDs the energetically lowest transition is bright, leading to the dominance of X_0 in the absence of additional free charge carriers. For W-based TMDs, the energetic ordering of bright and dark state is reversed, bringing the spin-aligned conduction subband close to the Q valley and above the spin-aligned but momentum-indirect K' valley. As a result, the spectrum of monolayer WSe_2 and WS_2 shows a rich substructure, that, in addition to X_0 shows signatures of phonon-sidebands of momentum-indirect excitons [38, 57, 58]. This naturally applies to the bilayer which, due to its indirect band gap, predominantly shows photoluminescence of momentum-indirect excitons [39]. The reservoir of spin-dark excitons with high radiative lifetime [55] also radiatively recombines with the assistance of strain defects [59, 60] and thus enables the realization of strain engineered single photon sources [61–63], that cannot be realized in Mo-based TMDs.

2.3 Effects of strain on the electronic band structure

Strain is an important parameter that allows tuning of many properties of semiconductors, including electron mobility, band splitting and warping as well as effective mass [64]. An important example is uniaxially strained silicon. By growing a thin film of SiGe on top of silicon, the strain of the silicon atoms at the interface to SiGe results in band warping that leads to a strong increase in electron mobility and faster switching times in strained silicon transistors [65].

However, the amount of strain applicable to a certain material is fundamentally limited by its elasticity. It has been argued that a defect free, elastic crystal can theoretically sustain strain of approximately one ninth its Young's modulus [66]. While silicon, despite a high Young's modulus of 160 GPa [67] typically breaks at a strain of $\leq$1.5%, 2D materials such as TMDs are shown to be much more resistant. For example,

a monolayer of MoS_2 has been shown to sustain a strain of between 6 and 11%, corresponding to an average breaking strength of 23 GPa [68]. With a Young's modulus of 270 $\pm$ 100 GPa [68], this value is close to the theoretical limit. Similarly, WS_2 and WSe_2 have been found to exhibit a Young's modulus of 302.4 $\pm$ 24.1 GPa and 258.6 $\pm$ 38.3 GPa, with a strength of 47.0 $\pm$ 8.6 GPa and 38.0 $\pm$ 6.0 GPa, respectively [69]. As a result, the dynamic range for tuning the optical and electronic properties of TMDs is potentially much higher than in conventional bulk semiconductors.

2.3.1 Theoretical description of strain in 2D materials

Theoretically, strain is understood as the modification of interatomic positions with respect to the unstrained material. As mentioned before, TMDs form a trigonal prismatic unit cell with a triatomic basis. Under strain, the bonds between atoms get modified in length, corresponding to a storage of elastic energy. This elastic energy is divided into stretching and bending energies [70]. The crystal structure of a strained 2D material can thus be described by a two-dimensional vector $\mathbf{r} = (x, y)$, parametrizing the unstrained crystal that experiences a displacement $\mathbf{u}(\mathbf{r}) + \hat{z}h(\mathbf{r})$, with the 2D vector field $\mathbf{u}(\mathbf{r}) = (u_x(\mathbf{r}), u_y(\mathbf{r}))$ corresponding to in-plane deformation (stretching) and the scalar field $h(\mathbf{r})$ describing out-of-plane deformation (bending). Strain is then described as a second-rank tensor field

$$\varepsilon_{ij} = \frac{1}{2}\left(\partial_i u_j + \partial_j u_i + \partial_i h \partial_j h\right), \tag{2.3}$$

with $i, j \in \{x, y\}$. The contribution of strain to the Hamiltonian of an unstrained 2D material is represented by the elastic energy density E_{el}. It is written as a sum of the stretching energy density E_{st} that represents in-plane deformation and the bending energy E_b that encodes an energy cost due to out-of-plane deformation, i.e. deviation from a flat plane:

$$E_{\mathrm{el}} = E_{\mathrm{st}} + E_{\mathrm{b}}. \tag{2.4}$$

The stretching and bending terms can be related to the Lamé parameters from continuum mechanics through:

$$E_{\mathrm{st}} = \frac{1}{2}\left(\lambda \varepsilon_{ii}^2 + 2\mu \varepsilon_{ij}\varepsilon_{ij}\right) \text{ and} \tag{2.5}$$

$$E_{\mathrm{b}} = \frac{1}{2}\kappa\left(\nabla^2 h\right)^2, \tag{2.6}$$

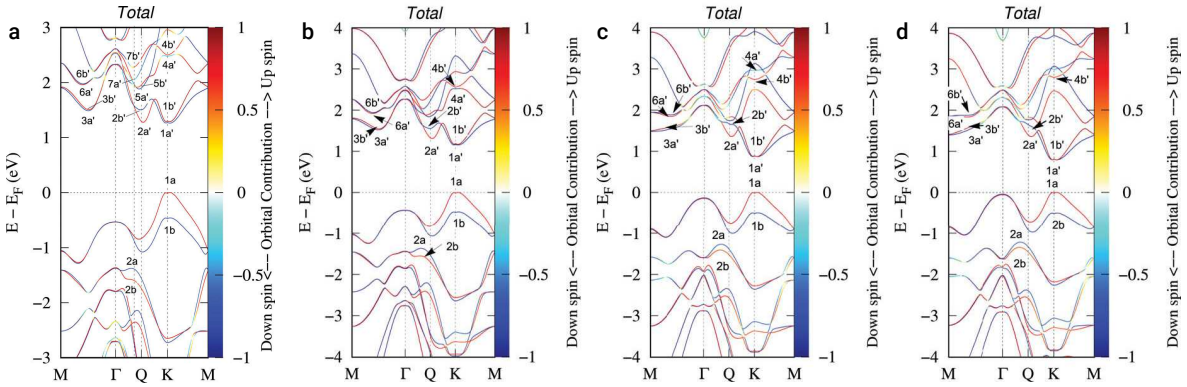

Figure 2.3 Band structure of strained monolayer WSe_2. Total spin projected band structures of monolayer WSe_2 under no strain (a) and under tensile strain of 1% (b), 4% (c) and 5% (d). Figure adapted from [72].

with λ, μ being the in-plane Lamé parameters and κ being the bending rigidity. Further, the stretching energy E_{st} is explicitly written as [71]

$$E_{\mathrm{st}} = \frac{Y_{2d}}{2\left(1-\nu^2\right)}\left[\varepsilon_{xx}^2 + \varepsilon_{yy}^2 + 2\nu\varepsilon_{xx}\varepsilon_{yy} + (1-\nu)\varepsilon_{xy}^2\right], \tag{2.7}$$

in terms of the two-dimensional Young's modulus Y_{2d} and the Poisson ratio ν, that derive from the Lamé parameters as

$$Y_{2d} = (\lambda + 2\mu)\left(1-\nu^2\right) \text{ and } \nu = \frac{\lambda}{\lambda + 2\mu}. \tag{2.8}$$

These equations are applied to the Hamiltonian of an unstrained 2D material to derive strain-induced changes to the electronic band structure that determines the optical properties of TMDs. There are multiple theoretical tools to calculate the band structure including tight binding (TB) models, $\mathbf{k}\cdot\mathbf{p}$ theory and density functional theory (DFT).

One major result of these calculations is a narrowing of the direct band gap under tensile strain [73, 74], i.e. an increase in interatomic distance in the x/y-plane. The band structure of unstrained and strained WSe_2 is seen in Fig. 2.3 [72]. Under vanishing strain, the direct band gap is located at the K point, with the spin-aligned sub band in K showing a slightly higher energy than the Q-valley, consistent with a high population of both spin-dark KK and momentum-dark QK excitons. Under tensile strain both conduction bands in K shift downwards, with a stronger shift in the spin-aligned sub band and both bands shifting away from the Q-valley, suppressing momentum indirect transitions. Finally, at high tensile strain the Γ-valley shifts upwards, suggesting

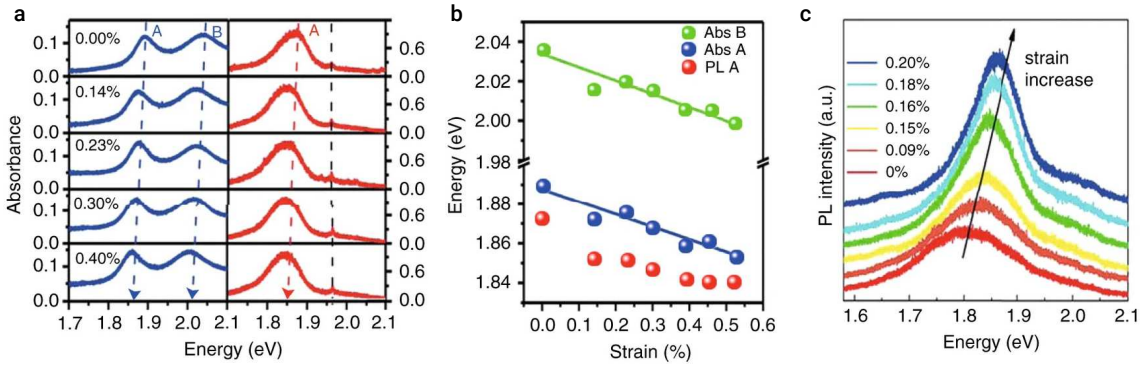

Figure 2.4 Exciton energy in strained monolayer TMDs. a, b Evolution of PL and absorption spectra (a) and peak positions (b) of monolayer MoS_2 under uniaxial tensile strain. Figure adapted from [75] **c,** Evolution of the PL spectrum of trilayer MoS_2 under biaxial compressive strain. Figure adapted from [76]. Strain-dependent PL spectra of monolayer WSe_2 (offset). Figure adapted from [77]

a direct-to-indirect band gap transition at strain above ~5%. This effect stems from the reduction in overlap between metal and chalcogen atoms as they are separated under strain [70].

2.3.2 Spectroscopy of strained 2D materials

Strain-dependent spectroscopy is utilized to measure this effect experimentally as shifts of spectral lines give a signature of changes in the band structure. Several techniques allow the application of strain in experiment. Uniaxial, homogeneous strain is applied by e.g. bending [75, 78, 79] or elongation [80] of a flexible sample substrate such as PDMS, PMMA, PC or PET. Biaxial, homogeneous strain is possible through e.g. a thermal expansion mismatch between TMD and substrate in a CVD growth process [81], the use of a piezoelectric substrate which is expanded or contracted through an applied voltage [76] or by embedding a suspended monolayer in a gated microdrum device [82]. Examples for experimental results in 2D MoS_2 and WSe_2 are shown in Fig. 2.4. Under homogeneous tensile strain, both PL and absorption spectra show a linear redshift in *A* and *B* exciton resonances (Fig. 2.4a,b) [75, 77] while compressive strain leads to a linear blueshift (Fig. 2.4c) [76].

While homogeneous strain is an interesting tool to create sample-wide changes in the band structure, a particularly interesting field of strain physics in TMDs is the interaction of strain with defect states. This applies to WSe_2 in particular, as the energetic

ordering of bright and dark states results in much of the exciton population residing in spin-dark and momentum-indirect states that, in an unstrained sample, contribute little to the optical spectrum in either PL or absorption. However, under strain, these excitons can under certain circumstances recombine radiatively much more efficiently. For example, it has been demonstrated that by straining a monolayer of WSe_2, dark excitons can hybridize with defect states that are less affected by strain and brighten up considerably [82]. Another route are local straining approaches that leverage strain-induced band modification to create localized potentials. Fox example, in WSe_2 mono- and bilayers, nanostructures like nanopillars can locally induce strain to funnel excitons into the resulting potential and result in bright PL [83]. By using a piezo-electric substrate, this local strain potential is controlled by first preparing a wrinkled WSe_2 monolayer on the substrate and subsequently applying a voltage to the piezo [61]. This results in strain-tunable single photon sources in the wrinkled regions. Of particular interest for this thesis are methods that use sharp tips to selectively strain a sample at different locations in-situ. For example, the sharp tip of an AFM may be used to create indentations in a monolayer of WSe_2 that is placed on an elastic polymer substrate, resulting in a similar effect of creating bright single-photon emitters [84]. Another approach uses a tapered optical fiber to create localized strain in a suspended WSe_2 monolayer in-situ, resulting in a funneling of spin-dark excitons into regions of maximum strain at the angled edges of the fiber [60].

2.4 WSe_2 mono- and bilayers in magnetic field

Part of this section is adapted from the publication

Förste, J. *et al.* Exciton g-factors in monolayer and bilayer WSe_2 from experiment and theory. *Nat. Commun.* **11,** 4539 (2020)

The response to an applied magnetic field plays a key role in the photophysics of TMDs. Just like orbitals in atoms, the energy bands inside a crystal exhibit a magnetic moment that leads to an energy shift inside a magnetic field. As inversion symmetry breaking and strong spin-orbit coupling inside TMDs leads to a spin polarization at the K and K' valley, this shift lifts their energetic degeneracy and leads to a splitting within the optical spectrum as well as the suppression of intervalley scattering that results in an increase of valley polarization [86]. This behavior is known as the valley Zeeman effect in analogy to the fine structure splitting of the hydrogen atom and is quantified by the exciton g-factor [87]. As the different valleys couple to light of or-

thogonal circular polarization, this splitting is defined by the relative energy positions of spectral lines when analyzed in an opposite circular basis:

$$\Delta_B = E_{\sigma^+} - E_{\sigma^-} = g\mu_B B_z, \tag{2.9}$$

with the magnetic splitting Δ_B, the energy of a spectral line E_{σ^+} (E_{σ^-}) measured in the σ^+ (σ^-) basis, the perpendicular magnetic flux B_z, the g-factor g and the Bohr magneton $\mu_B = |e|\hbar/(2m_0c)$, depending on the free electron charge e and mass m_0, the reduced Planck constant $\hbar$ and the speed of light c. The g-factor of the bright and spin-dark exciton was already theoretically predicted early on using tight-binding models, which give good approximations for the band-composition in the vicinity of the highly symmetric K/K'-points.

Around the K point, the band structure is mostly given by the large d-orbitals of the heavy transition metal atom, W in the case of WSe_2. In the valence band, the hybridized $d_{x^2-y^2} \pm id_{xy}$ orbitals dominate and lead to an orbital angular momentum along the z-axis of $l_z = 2\hbar$, corresponding to a magnetic moment of $\mu_K = 2\mu_B$. The origin of the conduction band lies in the d_{z^2} orbitals that have no out-of-plane angular momentum as well as no corresponding magnetic moment. Thus, in a magnetic field, valence and conduction band exhibit a differential shift leading to the modulation of the band gap energy. As the direction of the magnetic moment is reversed between K and K' valley, so is the energy-shift leading to a splitting between the valleys of $\Delta_{K,K'} = 4\mu_B B_z$ with the corresponding g-factor of $g_X = -4$ for the bright exciton. The sign of the g-factor, as defined in Eq. 2.9 depends on the definition of the circular basis and is therefore chosen by convention. Another contribution to the magnetic moment stems from the spin-component of electron and hole. For the bright transition, the parallel spins cancel each other and lead to a vanishing contribution to the g-factor. The spin-dark exciton however features anti-parallel spins of electron and hole that contribute with their spin $S = \pm\frac{1}{2}$ which is multiplied by the electron g-factor of $g_e \approx 2$. This yields a value of $g_D = -8$ for the spin-dark exciton. Both of these results are in agreement with experiments [55].

In the past, models to explain the numerical value of the exciton g-factors in TMDs mainly focused on direct, intravalley K-valley transitions, utilizing tight-binding models. While the results from these models align with experimental values for the bright and spin-dark excitons [55, 86, 87], the complex photoluminescence spectrum of WSe_2 shows different g-factors for various spectral lines such as phonon sidebands of momentum-dark excitons [38, 88]. As they are suspected to incorporate contributions from the

lower-symmetry Q-valley, simple tight-binding models break down and predict incorrect numerical values [89]. They also fail to explain the behavior of the WSe_2 bilayer which is exhibiting a clearly defined indirect band gap and is dominated by momentum-dark excitons.

2.4.1 Theoretical prediction of exciton g-factors

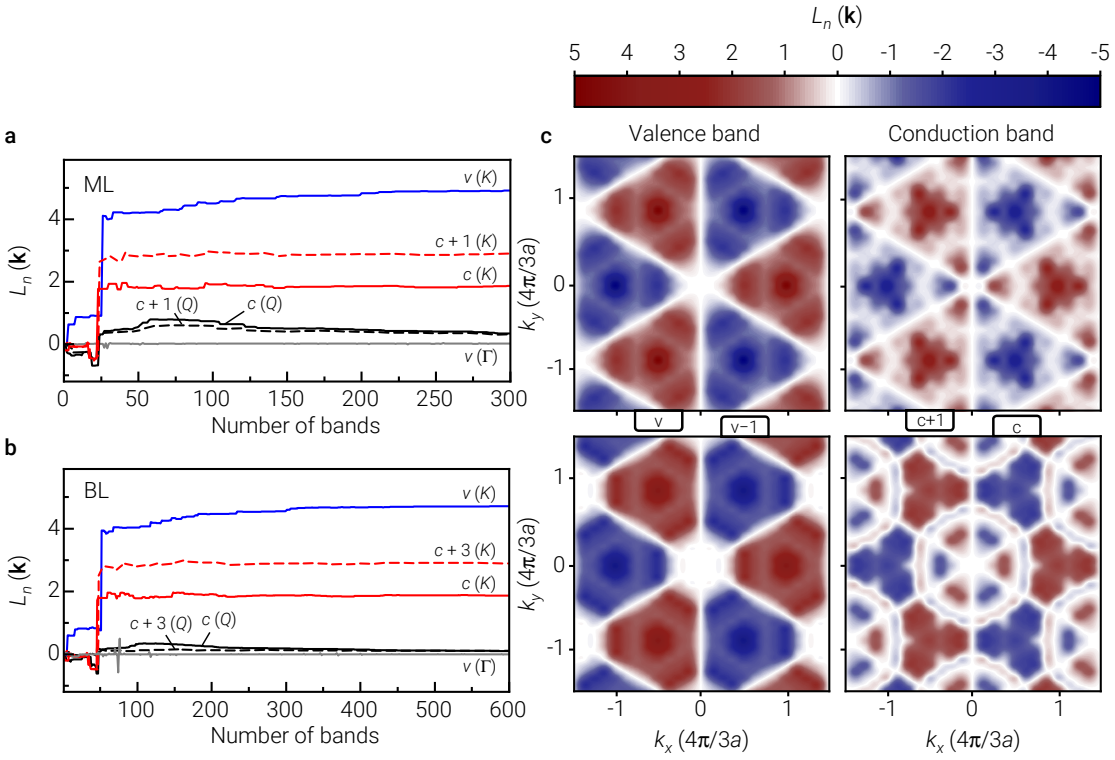

Figure 2.5 Orbital angular momentum of monolayer and bilayer WSe_2 from DFT. a, b Evolution and convergence of orbital momentum from DFT calculations for the highest valence bands at K and Γ as well as the lowest conduction bands at K and Γ in both monolayer and bilayer respectively. **c,** Orbital angular momentum in the first Brillouin zone for the highest valence bands v and $v-1$ as well as the lowest conduction bands c and $c+1$ from DFT calculations including spin-orbit effects.

This gap is closed by going beyond the tight-binding approach and utilizing density functional theory (DFT) to predict g-factors throughout the entire Brillouin zone. As discussed earlier, the valley Zeeman effect originates from the differential shift of the valence and conduction bands for different exciton species. Therefore, to predict the

Table 2.1 Exciton g-factors for monolayer and bilayer WSe_2 from DFT. Exciton g-factors for selected spin-valley configurations of excitons in monolayer and bilayer WSe_2.

Exciton	Valley $(\mathbf{k}_c, \mathbf{k}_v)$	Spin (s_c, s_v)	ML	BL, intralayer	BL, interlayer
X^0	KK	↑↑	-4.0	-3.6	-13.2
D^0	KK	↓↑	10.1	9.7	19.2
K'_L	$K'K$	↑↑	13.6	13.2	3.6
K'_U	$K'K$	↓↑	19.6	19.2	9.7
Q_L	QK	↑↑	9.2	9.2	9.7
Q_U	QK	↓↑	13.2	13.3	13.6
Q'_L	$Q'K$	↑↑	10.2	9.7	9.2
Q'_U	$Q'K$	↓↑	14.5	13.6	13.3
	$K\Gamma$	↑↑	5.8	5.8	3.7
	$K\Gamma$	↓↑	0.3	0.3	9.8
	$K'\Gamma$	↑↑	3.7	3.7	5.8
	$K'\Gamma$	↓↑	9.8	9.8	0.3
	$Q\Gamma$	↑↑	0.7	0.2	0.2
	$Q\Gamma$	↓↑	3.4	3.9	4.1
	$Q'\Gamma$	↑↑	0.6	0.2	0.2
	$Q'\Gamma$	↓↑	4.7	4.1	3.9

g-factor, band energies in the presence of a magnetic field have to be calculated.

The drivation of the band structure starts with a crystal electron in a Bloch state $\psi_{n\mathbf{k}}(\mathbf{r}) = S^{-1/2}\exp(\mathrm{i}\mathbf{k}\mathbf{r})u_{n\mathbf{k}}(\mathbf{r})$, corresponding to energies $E_{n\mathbf{k}}$, with the band number n, the wave vector $\mathbf{k}$, the periodic Bloch amplitude $u_{n\mathbf{k}}(\mathbf{r})$ and the normalization area S. A static magnetic field $\mathbf{B}$ is treated as a weak perturbation. The first-order correction to the electron energy is proportional to $\mathbf{B}$ and given by [90]:

$$V_n(\mathbf{k}) = \mu_B \mathbf{B}\left[g_0\mathbf{s} + \mathbf{L}_n(\mathbf{k})\right], \tag{2.10}$$

with the latter expression usually being called the effective magnetic moment [91, 92], which contains both spin and orbital contributions. The first term includes the free electron Landé factor $g_0 \simeq 2$ and the spin $\mathbf{s} = \sigma/2$, where σ denotes the Pauli matrix. The second term, $\mathbf{L}_n(\mathbf{k}) = \langle\psi_{n\mathbf{k}}(\mathbf{r})|\mathbf{L}|\psi_{n\mathbf{k}}(\mathbf{r})\rangle$, is the orbital angular momentum with the operator $\mathbf{L} = \hbar^{-1}[\mathbf{r}\times\mathbf{p}]$. To find the matrix elements, the calculation is reduced to the interband matrix elements of the space coordinate operator $\mathbf{r}$ [91, 92].

$$\mathbf{L}_n(\mathbf{k}) = \frac{m_0}{\mathrm{i}\hbar^2} \sum_{m \neq n} \left[\xi_{nm}(\mathbf{k}) \times \xi_{mn}(\mathbf{k}) \right] (E_{n\mathbf{k}} - E_{m\mathbf{k}}) \tag{2.11}$$

where m is the sum over all bands with energy $E_{n\mathbf{k}}$ except the band of interest n, and $\xi_{nm}(\mathbf{k}) = \mathrm{i} \langle u_{n\mathbf{k}}(\mathbf{r}) | \partial/\partial \mathbf{k} | u_{m\mathbf{k}}(\mathbf{r}) \rangle$ is the interband matrix element of the crystal coordinate operator.

As for typical experiments, the orientation of the magnetic field is restricted to align with the z-axis with the electron Zeeman splitting defined as the difference between the energy of the electron state with wave vector $+\mathbf{k}$ and spin projection $+s$ along the z-axis and the state with $-\mathbf{k}$ and $-s$:

$$\Delta_n(\mathbf{k}) = V_n(+\mathbf{k}) - V_n(-\mathbf{k}) = 2\mu_\mathrm{B} B \left[g_0 s + L_n(\mathbf{k}) \right]. \tag{2.12}$$

According to Eq. 2.9, the g-factor of electrons in the nth band is written as:

$$g_n(\mathbf{k}) = \frac{\Delta_n(\mathbf{k})}{\mu_\mathrm{B} B} = \pm g_0 + 2L_n(\mathbf{k}), \tag{2.13}$$

with $+(-)$ for $s = +1/2(-1/2)$, corresponding to spin up (down) projections along z denoted as $\uparrow(\downarrow)$, and the explicit expression for the z-component of the orbital angular momentum:

$$L_n(\mathbf{k}) = \frac{m_0}{\hbar^2} \sum_{m \neq n} \left[\left| \xi_{mn}^{(-)}(\mathbf{k}) \right|^2 - \left| \xi_{mn}^{(+)}(\mathbf{k}) \right|^2 \right] (E_{n\mathbf{k}} - E_{m\mathbf{k}}), \tag{2.14}$$

$$\text{where } \xi_{mn}^{(\pm)} = \left(\xi_{mn}^{(x)} \pm \mathrm{i} \xi_{mn}^{(y)} \right) / \sqrt{2}. \tag{2.15}$$

To simplify the calculation for contributions of both conduction (c) band electron with $\mathbf{k}_c, s_c$ and the hole (h) with $\mathbf{k}_h, s_h$ to the exciton g-factor, electron-hole Coulomb interactions are neglected. As a result, the Zeeman splitting is simply the sum of the splitting of electron and hole. Using time-reversal symmetry that relates spin and wave vector of the hole to the corresponding spin and wave vector of the empty electron state in the valence (v) band ($s_h = -s_v$ and $\mathbf{k}_h = -\mathbf{k}_v$), the exciton g-factor are given by:

$$g^{(cv)}(\mathbf{k}_c, \mathbf{k}_v) = g_c(\mathbf{k}_c) - g_v(\mathbf{k}_v). \tag{2.16}$$

Lastly, spin-like (L) and spin-unlike (U) excitons are distinguished, where $s_c = s_v$ and $s_c = -s_v$ respectively. This is defined in relation to the valence band electron with $\mathbf{k}_v = K$ or Γ with spin-up projection $s_v = +1/2$. Their respective exciton g-factors are given by:

$$g_L^{(cv)}\left(\mathbf{k}_c, \mathbf{k}_v\right) = 2\left[L_c\left(\mathbf{k}_c\right) - L_v\left(\mathbf{k}_v\right)\right], \tag{2.17}$$

$$g_U^{(cv)}\left(\mathbf{k}_c, \mathbf{k}_v\right) = 2\left[L_c\left(\mathbf{k}_c\right) - L_v\left(\mathbf{k}_v\right)\right] - 2g_0. \tag{2.18}$$

These relations only depend on the respective orbital momenta $L_c\left(\mathbf{k}_c\right)$ and $L_v\left(\mathbf{k}_v\right)$ of cunduction and valence band as obtained from eq. 2.15 and are numerically determined using DFT.

These computations were performed within the generalized gradient approximation with the PBEsol exchange-correlation functional, as implemented in the Vienna ab initio simulation package. Van der Waals interactions were considered within the DFT-D3 method with Becke-Johnson damping; Spin-orbit interaction was included at all stages. Elementary cells with a vacuum thickness of 30 Å were used in order to minimize interactions between periodic images. Atomic positions were relaxed with a cut-off energy of 400 eV until the change in total energy was $< 10^{-6}$ eV. The band structure of ML (BL) was calculated on the Γ-centered $\vec{k}$ grid of 12×12 divisions with 300 (600) bands.

The convergence of the orbital angular momenta for both ML and BL is seen in Fig. 2.5a, b, as a function of the number of bands included into the sum in eq. (2.15). In Fig. 2.5a results are shown for the top-most valence band state v at K (blue solid line) and the highest valence band state v at Γ (gray solid line) in the monolayer, as well as the two lowest lying conduction band states c and $c+1$ at K and Q (red and black solid and dashed lines). Bands in the bilayer case are double degenerate, thus each $\mathbf{k}$-point of the Brillouin zone has at least two bands with $L_n(\mathbf{k}) = L_{n+1}(\mathbf{k})$ or $L_n(\mathbf{k}) = L_{n-1}(\mathbf{k})$. In Fig. 2.5b, we consider the same $\mathbf{k}$-points for the bilayer as for the monolayer and show the corresponding bands with orbital momenta of the same sign as in the ML case as shown in Fig. 2.5a.

As shown in the graph, convergence of the angular momenta requires taking into account a high number of bands, above 275 for the ML and above 550 for the BL. For the latter, the double number of atoms introduces a factor of two, while otherwise showing similar behavior. Ideally, the values for $v(\Gamma)$ should vanish based on symmetry arguments. However, taking into account only a finite amount of bands, the numerical calculations are still yield values of ± 0.01. Assuming a similar convergence behavior in other orbital momenta, this deviation is used as an estimate for the precision of the model and to assign an error to the corresponding values of the g-factors. For the values given in table 2.1, this bound ranges in the order of $\pm$ 0.05.

As also shown in the graph is, certain bands contribute more strongly to the g-factor

than others. Thus, according to eq. 2.15, the orbital angular momentum is proportional to the product of interband matrix elements which are largest for the fundamental A-exciton transition X^0, in the ML case between bands 24 and 26 or band 23 and 25 for the B-exciton. As shown in Fig. 2.5a, these are exactly the bands providing the largest contribution to the g-factor.

In Fig. 2.5c the DFT results for $L_n(\mathbf{k})$ within the first Brillouin zone are shown for both conduction and valence band. As spin-orbit effects are iconsidered in the calculation, this includes the two highest, spin-split valence (v and $v-1$) and conduction (c and $c+1$) bands. Using these results, the g-factors of the lowest-energy excitons in the ML are calculated using eqs. (2.17), (2.18). Table 2.1 shows all g-factors obtained from these results and includes different configurations of valleys ($\mathbf{k}_c$, $\mathbf{k}_v$) and spins ($\mathbf{s}_c$, $\mathbf{s}_v$, with $\uparrow$ or $\downarrow$ projection along z).

3 Experimental methods

This chapter describes the experimental methods used throughout this thesis. In the first section, an overview of the sample preparation process based on mechanical exfoliation and viscoelastic stamping is given. This is followed by a description of cryogenic confocal microscopy and atomic force microscopy, using electrically actuated quartz tuning forks.

3.1 Fabrication of van der Waals heterostructures

Van der Waals heterostructures are fabricated from individual sheets of different layered materials and are held together by interlayer van der Waals forces, similar to their corresponding bulk material. These individual sheets are as thin as a single layer which are either isolated through exfoliation strating from a bulk crystal [2] or directly grown, using chemical vapor deposition (CVD) [93] or epitaxy [94]. To fabricate a heterostructure these precursors are assembled mechanically, through wet transfer [95] or polymer-assisted viscoelastic stamping[96, 97]. These heterostructures may be embedded into more complex devices to allow e.g. doping control via the field effect. Devices used in this thesis are fabricated using mechanical exfoliation and temperature controlled viscoelastic stamping, combined with UV-lithography, metal deposition and reactive ion etching (RIE), to create field effect devices and suspended monolayer samples for doping and strain tuning respectively.

3.1.1 Mechanical exfoliation

As mentioned in Chapter 2, layered materials are bound strongly in-plane but only weakly held together out-of-plane through van der Waals forces. As a result, it is possible to isolate thin flakes down to the monolayer limit using mechanical exfoliation. This method is performed using adhesive tape [2], and commonly named the "scotch-tape"-method. First, a monocrystalline bulk crystal of the material is placed on a strip of tape and peeled off. Due to the low interlayer force compared to the ad-

hesive strength, a thin flake is readily exfoliated from the bulk. This piece of tape is then placed on another strip and peeled off again, thinning the film further. This step is repeated four to seven times, using a fresh strip of tape for each subsequent exfoliation step, before the contents of the tape are released onto a suitable substrate. The substrate is typically a rectangularly cut wafer of silicon that is covered with thermal oxide (Si/SiO_2). In storage, these wafers are covered with a thick film of photoresist to avoid damage to the polished surface. Before processing, this coating is removed using acetone, followed by a rinse in isopropanol. Both steps can be accelerated using an ultrasonic cleaning bath. Subsequently, each wafer is treated in oxygen plasma (GigaEtch) at 200W for 180s to remove remaining residues and promote adhesion of the 2D materials[98]. Right before bringing the tape into contact, the wafer is heated on a hot plate to between 80 °C and 90 °C.he goal is to keep contamination with air humidity low and to increase the yield of material released from the tape, as the glue of the tape tends to release more easily at elevated temperatures. The exact procedure is varied for different types of tape as glue release, melting and tape deformation may happen at different temperatures. This hot release, while helpful in increasing yield, also results in heightened contamination of the substrate with tape residue. After cooling, the tape is peeled off, releasing material onto the wafer, which is inspected and used for further processing.

3.1.2 Optical characterization

Mechanical exfoliation produces wafers that are filled with small flakes of different shapes and thicknesses as well as varying levels of contamination with tape residue or mechanical damage. Thus, only a small subset of exfoliated flakes is suitable to be used in a sample, which is identified using an optical microscope. The first step is to find flakes of appropriate thickness and lateral dimensions, which have to be large enough in order to increase the chances of finding pristine and homogeneous areas later on. The minimum limit is chosen to be approximately 5 μm × 5 μm.

Layer thickness

The thickness of individual layers of 2D materials is measured using the brightness contrast in an optical microscope [100]. The contrast is calculated within each channel of the RGB-encoded image of a CMOS camera (FLIR Grasshopper GS3-U3-123S6C-C) using the following formula:

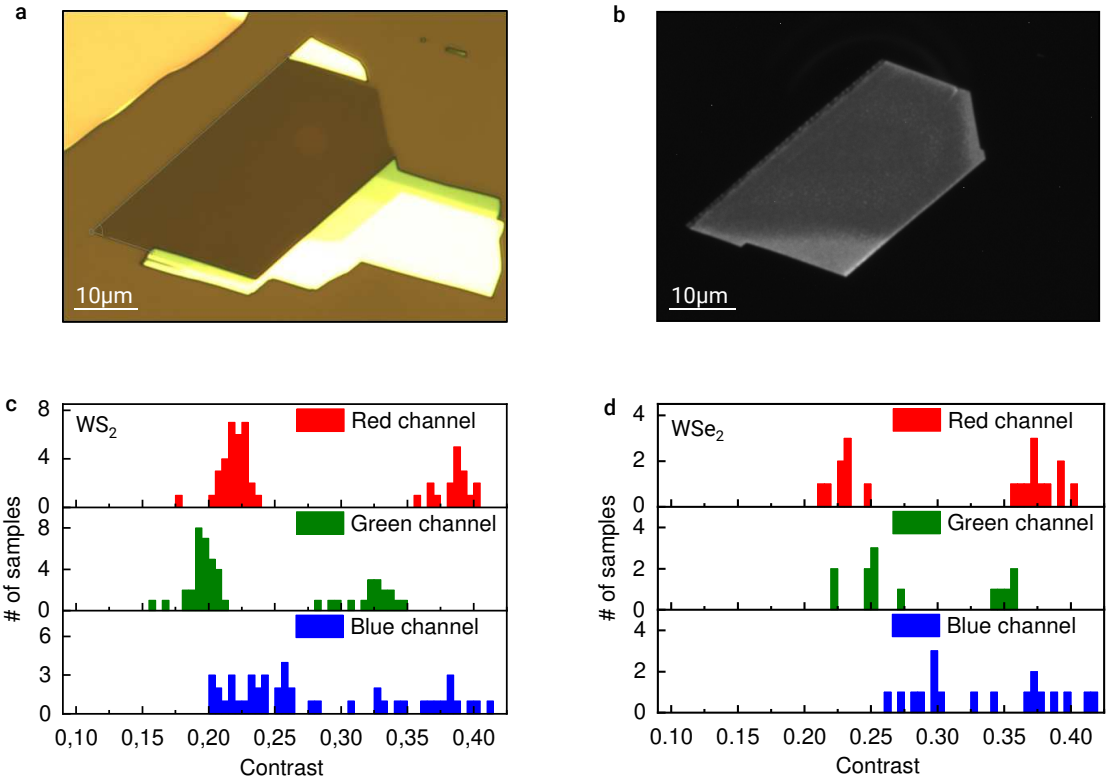

Figure 3.1 Color contrast of 2D materials. **a, b** Brightfield and photoluminescence image of a monolayer of WS_2. **c, d** Histogram showing contrast distribution of samples of WS_2 and WSe_2 respectively [99]. Each count in the histogram represents a sample of a priori unknown thickness. Contrast is measured separately in the red, green and blue channel of the image of a Bayer pattern CMOS color camera, transformed into the RGB color space.

$$C(\lambda) = \frac{R_0(\lambda) - R(\lambda)}{R_0(\lambda)} \tag{3.1}$$

with $R_0(\lambda)$ being the intensity of the light reflected off the substrate background and $R(\lambda)$ of the sample. In practice, these values are read from the brightness histogram of a monochromatic image of flake and substrate. This histogram plots the number of pixels for each intensity value. Thus, two otherwise homogeneous regions of sample and background should correspond to two distinct peaks in the histogram, broadened by both camera noise and inhomogeneities in either sample or lighting. The mode of each peak represents the brightness of the corresponding part of the image, while the area under each curve corresponds to the total amount of pixels. Assuming that de-

viations from this intensity are normally distributed, a Gaussian profile is fitted to each peak and $R_0(\lambda)$ and $R(\lambda)$ is read from the respective mean μ of the distributions. The contrast is a relative value that neither depends on absolute intensities of the light source nor sensitivity of the camera. However, some deviations specific to the experimental setup are to be expected. The biggest source of variation is the choice of substrate. For silicon covered with thermal oxide, the reflectivity $R_0(\lambda)$ strongly depends on the thickness of the transparent oxide layer [101]. Apart from the substrate, variations between different cameras introduce additional errors. While contrast is measured on a monochromatic image, cameras used in optical microscopes record color images encoded into three channels, corresponding to red, green and blue in the RGB-system. The sensor of a color camera consists of an array of light-sensitive pixels that record color information by overlaying a grid of optical band pass filters, a so-called Bayer filter [102]. As the filter bands used for a specific sensor are not standardized, color contrast varies between different camera models as well. Additionally, CMOS pixels tend to exhibit non-linearities at higher output currents [103], culminating in a flat clipping-response at overexposure. Finally, the spectrum of the white light source integrated into the microscope depends on the specific illumination technology, e.g. incandescent lights or light emitting diodes (LED).

Given all these potential sources of variation, it is useful to calibrate contrast values for any given substrate and microscope system. There are two strategies to measure the layer number needed for this calibration. One way is to measure the thickness of different samples directly, for example using an atomic force microscope (AFM). However, within our own experiments, AFM thickness measurements proved unreliable for exfoliated monolayers on SiO_2 substrates [99] The expected thickness of 0.8 nm for a monolayer is often overestimated, without being reliably distinguishable from a bilayer [104, 105]. Possible reasons for this are roughness-induced height noise from either substrate, 2D material or residual water from air humidity, forming a film between flake and substrate.

An alternative method to determine few-layer contrast is to statistically find the lowest contrast for an ensemble of samples of different thickness (see Fig. 3.1 [99]). The contrast of each sample is entered into a histogram that shows clusters around the contrast of a specific layer number. Ideally, this histogram shows an unbroken series of contrast values starting with a monolayer. In first approximation, every layer independently absorbs an equal amount of light. Therefore, every subsequent layer reduces in reflection intensity by the absorption value of a monolayer.

Our analysis shows that, irrespective of the color channel, TMD monolayers show

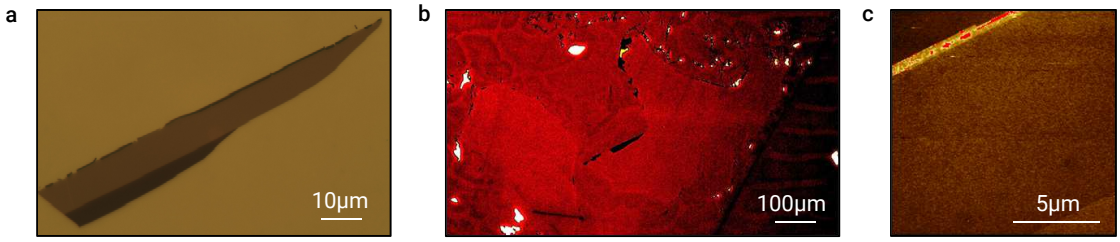

Figure 3.2 Contamination detection through optical contrast. a, Brightfield image of a monolayer $MoSe_2$ in normal contrast. **b,** The same flake and its surroundings on the substrate in strongly enhanced optical contrast. **c,** AFM image from a subsection of the sample.

an optical contrast of 20 % – 25 %, with the highest contrast in the blue channel. For bilayers this contrast lies at 32 % – 38 %. The broad variation corresponds to differences of both color-channel and specific material, with any specific contrast value showing an error of 3 % or lower. The same procedure was also repeated for graphene, yielding values of 8 % – 9 % for a monolayer and 13 – 17 % for a bilayer, again with the highest contrast in blue and individual errors being 2 % or lower.

An additional verification tool for TMD monolayers specifically is photoluminescence (PL) imaging. Because of their efficient radiative exciton recombination, monolayers are identified by their strong luminescence upon excitation with white light of an optical microscope. Compared to bilayers, monolayers show a strong increase in luminescence [106] and are thus easily distinguished from thicker flakes (see Fig. 3.2b).

Hexagonal Boron Nitride

Thickness determination of hBN follows a different pattern compared to TMDs or graphene. As it is a transparent dielectric, the contrast of very thin flakes in the order of monolayers is much smaller and does not monotonically increase for thicker flakes. Instead, it oscillates through constructive and destructive interference, depending on the thickness, which complicates precise thickness determination with optical contrast alone. This can however be supplemented by AFM measurements.

Sample quality

Sample quality is broadly categorized into mechanical damage, such as wrinkles and cracks and contamination with tape residue. Mechanical deformations introduce strain that locally changes the spectrum and brightens defects, while tape residue causes imperfect heterostructure interfaces and a disordered dielectrical environment, prohibiting narrow linewidth spectra. Both of these quality factors are assessed either optically or using AFM. As AFM is generally more time consuming than optical microscopy, suitable sample candidates are first identified optically and only imaged in AFM if they appear pristine.

Fig. 3.2 shows from left to right the same clean flake of $MoSe_2$ in bright field microscopy, a zoomed-out image at high contrast and a section of the flake imaged in AFM. Tape residue on the surface of a thin flake of any 2D material, unless particularly strong, is typically not directly visible. However, if the flake was exfoliated in the last step of the exfoliation series, the sample is unlikely to be contaminated as neither side of the flake were in contact with the tape. This is determined by artificially enhancing the contrast of a bright field microscope image, as is seen in Fig. 3.2b, which helps to visualize subtle brightness differences on the substrate surface. In this mode, areas with tape residue appear slightly darker shaded with additional substructure, while areas that were covered with larger TMD flakes at the time of contact are lighter shaded with clear outlines. Therefore, if a sample candidate is located inside a lighter area, contamination on its surface is unlikely. In Fig. 3.2b, the $MoSe_2$ monolayer flake is located at a border between pristine and contaminated areas. The surface quality of this sample was therefore verified using AFM (Fig. 3.2c). While the multilayer edge of the flake shows a disordered topography with peaks shaded in red, the monolayer area appears to be homogeneous and therefore free of contamination.

3.1.3 Assembly through viscoelastic stamping

Samples used throughout this thesis are all based on heterostructures of WSe_2 and WS_2, encapsulated between two layers of hBN. These types of samples are built using temperature controlled viscoelastic stamping This technique is utilizing an elastic, transparent piece of polydimethylsiloxane (PDMS), covered with a thin film of either polypropylene carbonate (PPC) [96] or polycarbonate (PC) [107] to lift precursor flakes from their initial substrate, assemble the sample heterostructure on the stamp and finally release it onto a suitable substrate.

The process starts by creating a stamp made of PDMS, that is either rectangular or

dome-shaped. Initially, the polymer is prepared by mixing liquid PDMS with a curing agent (Sylgard 184^{TM}) at a ratio of 10:1. To remove air from the viscous mixture, it is placed in a vacuum desiccator for approximately 15 minutes. To create dome-shaped stamps, PDMS is directly applied onto glass slides. In the first step, a droplet of PDMS is deposited on the surface of the slide before being cured with the PDMS facing down for 20 minutes at 140 °C. The stamp should have a height of approximately 3-5 mm. If needed, more PDMS is added after the first droplet has hardened enough to retain its shape. Next, the stamp is left at room temperature overnight or approximately 12 hours.

A rectangular stamp is made by pouring a several millimeter thick film of PDMS into a dish. After hardening, custom pieces of typically no more than 5 mm x 5 mm are cut out using a scalpel and attached to a glass slide using transparent, double-sided adhesive tape.

When using PC for coating, the process starts by preparing a solution of PC by mixing solid polymer in chloroform at a mass fraction of 6 %. The mixture is stirred overnight or for approximately 12 hours at 500 rpm. Immediately before usage, it is again stirred for another 5 minutes. A thin film of PC is prepared by squeezing a drop of solution between two glass slides. After the chloroform has evaporated, the two slides are pulled apart which causes the PC film to stick to only one of the slides. To attach this film to the PDMS stamp, a piece of double-sided adhesive tape with a rectangularly cut out window in the center is placed on the dome-shaped stamp. To pick up the PC film, a second piece of tape with an equally shaped window is placed on top of it. Using a scalpel, parts of the film not covered by the tape are detached. By peeling off the tape, the PC is removed from the glass slide and placed on top of the PDMS stamp.

When using PPC coating, the solid PPC is instead mixed with anisole at a ratio of 1.5:10. This mixture is stirred over night at 180 °C. As PDMS is hydrophobic and PPC hydrophilic, the uncoated stamp is treated with oxygen plasma for 20 minutes at 200 W. This enhances the adhesion between the polymers and prevents unwanted separation of PPC and PDMS during the stamping process. A PPC film is directly spin coated onto the PDMS stamp at 1500 rpm resulting in a layer of 5 μm of thickness.

To assemble a heterostructure, every constituent layer is picked up seperately and stacked on top of each other. The heterostructure is thus first assembled on the stamp itself. The first layer of the stack sticks to the adhesive polymer and every subsequent layer sticks to the previous one, as van der Waals forces between the flat layers are stronger than the force between layer and substrate.

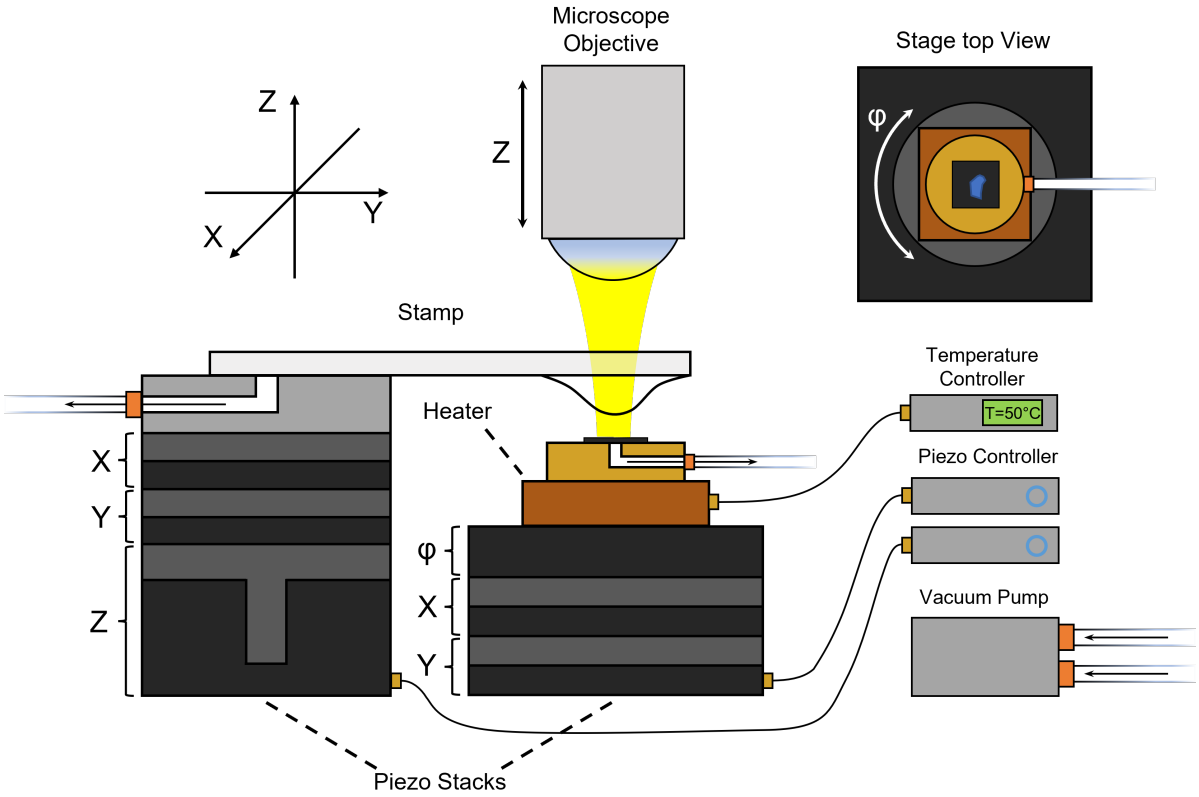

Figure 3.3 Assembly of 2D-heterostructures. The setup consists of two motorized stages powered by piezo-actuators and an optical microscope. The coated PDMS stamp on a glass slide is mounted to the first stage and moves in x/y/z-direction. The other stage holds the sample and moves in x/y-direction only. The optical focus is adjusted by moving the complete microscope head in the vertical z-direction. A ceramic heater is mounted beneath a copper sample holder. Both sample and stamp are held in place using suction. The setup is operated in an inert argon atmosphere. Figure adapted from [108].

The stamping setup is shown in Fig. 3.3. It is designed to move both stamp and sample independently using piezo-actuators (attocube ECSx5050, ECSz5050. ECR5050) while being able to move the focus of an optical microscope (Olympus, custom configuration) between both of them. To achieve this, both the stamp and the microscope itself can move in vertical z-direction. The advantage of this configuration is that during the stamping process, the focus is freely shifted between different planes while sample and stamp are standing still. In addition to movement in the lateral direction, the sample stage can also be rotated with a high degree of precision and is heated to a maximum of 200 °C (Thorlabs TC300 and HT24S/HT19R). Both sample and stamp are held in place using a membrane vacuum pump. The stamping stage is located

in a glovebox (MBraun Unilab+) that is filled with argon gas. The stamp is placed in between the microscope objective and the substrate. Before contact, the substrate is heated to a temperature that depends on the material being picked up. For hBN this temperature lies in-between 40 °C and 60 °C for PPC and up to 80 °C for PC. Both graphene and TMDs require higher temperatures between 100 °C and 120 °C for either PPC or PC. Next, the stamp is slowly brought in contact with the substrate. With a rounded stamp, the first point of contact between substrate and stamp lies in the center of the dome while a rectangular stamp will first touch close to one of its edges. To ensure a controlled stamping process, this point of contact is displaced with regards to the sample location. On contact with the substrate, the temperature of the stamp increases, resulting in thermal expansion and a widening contact area. Therefore, the stamp is allowed to equilibrate for several minutes. Next, the stamp is slowly lowered further, while monitoring the edge of the contact area. Once this edge reaches the sample, lowering of the stamp is slowed down to single steps of the piezo, such that the sample is slowly covered by polymer and the enclosure of potential gas bubbles is minimized. Once the contact interface covers the entire flake, the process is reversed and the stamp is lifted slowly. As the edge recedes, the lift-off of the sample is detected by an increase in translucency caused by the slight angle between beam path and sample and is verified once the separation is large enough for the sample to exit the focal plane of the microscope. Care should be taken to keep track of the location of the sample on the stamp between successive steps as the increase in translucency renders even large heterostructures almost invisible. The stamping process is repeated until all layers of the heterostructure are assembled on the stamp. To deposit the sample on the final substrate, the approach is first repeated as before. However, during lift-off, the sample is heated to a higher temperature in order to melt the polymer. For PPC, this is achieved for as low as at 150 °C, for PC the temperature needs to reach at least 180 °C. At these temperatures, the polymer liquifies while the stamp is slowly raised until the film fully delaminates from the PDMS. The polymer is now covering the sample and is finally removed with an appropriate solvent. A PPC film is dissolved in successive washes with acetone and isopropanol while PC is dissolved with chloroform before rinsing with DI-water. The finished sample is further treated with annealing, which aims at increasing the quality of the van der Waals materials by mobilizing any potential surface contaminations and residues. This is achieved in practice by heating the sample at 200 °C in ultra-high vacuum for 12 h. The annealing process poses a significant risk of damage to the sample and can result in cracks and tears as the individual layers get strained. Therefore, this step is omitted if possible.

3.1.4 Electrostatic doping control

Doping in semiconductor devices can be controlled electronically via the field effect. This is achieved by constructing a heterostructure where an insulating layer is sandwiched between the TMD sample and a conductive layer, made from e.g. doped silicon or few-layer graphene.

When using doped silicon as a substrate, a device is fabricated by lithographically defining a metallic contact with a TMD flake[109] and the substrate. The thermal oxide layer on commercially available silicon wafers offers a high quality gate dielectric. To address the conductive substrate, an electric contact needs to be established with a metallic wire. The substrate used in this thesis is boron-doped Si with 50 nm of thermal oxide which is strongly *p*-doped with resistivity below 1.5×10^{-5} Ωm. However, the interface between metal and silicon is still subject to the Schottky effect.. At room temperature, contact is established by scratching off the thin surface oxide layer on a cleaved edge and attaching a wire using a conducting adhesive such as silver paste. At low temperature however, a metal-semiconductor junction creates an undesired Schottky barrier.

This is avoided by introducing a gradual transition between metal and silicon which is created at the edge of the substrate using local doping. Local doping happens by locally heating the silicon substrate in the presence of boron-doped gold which will diffuse into the surface, creating a doping gradient and preventing a Schottky barrier from forming. In practice, this is achieved using two boron-doped gold wires, which are brought in close contact to the edge of the substrate. Using a 1000 μF capacitor, a voltage of ∼30 V is applied between the wires. When bringing the tips of the wire close enough to the surface, an electric arc will form. For air, the dielectric strength results in a required distance of < 10 μm at 30 V. Under these conditions, the arc will be guided through the substrate from wire to wire. The resulting heat evaporates material at the tip of the gold wire and heats up the substrate locally which results in gold diffusing into the silicon, forming an ohmic contact. On the surface, at the location of the discharge, gold deposits to form small droplets which are contacted to a metal wire using conductive silver paste.

An alternative to a global Si back gate is using few-layer graphene as a gate. In this configuration, the sample consisting of hBN and TMD is sandwiched between one or two few-layer graphene sheets on top or bottom, contacted by lithographically defined metallic electrodes. Additional sheets of graphene are used as contacts for the TMD. A dual-gate arrangement, using both top and bottom gate, allows for the application of an electric field in parallel to doping control. The fabrication follows

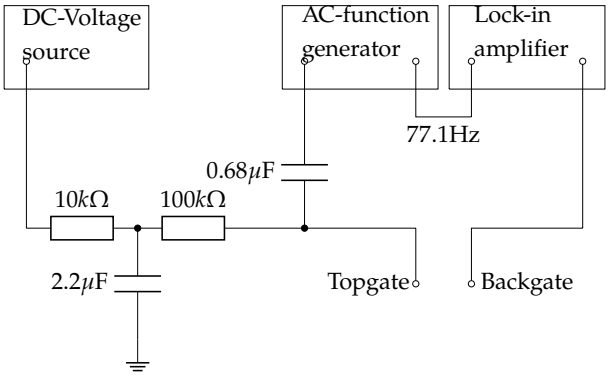

Figure 3.4 Circuit for CV-characterization [110]. Using a lock-in amplifier and a small AC voltage added to a DC voltage even very small resistive currents leaking through the sample dielectric is measured. This way, the maximum gate voltage at the gate is obtained by increasing the DC voltage until the value of the resistive current starts to rise exponentially.

the same exfoliation and stamping process as described before. If a graphene top gate is used, the stamping process is carried out using PC-coated stamps, as PPC is not able to lift graphene directly. When assembling the heterostructure, the top gate is picked up fist, followed by top hBN, contact graphite, TMD-sample, bottom hBN and bottom gate.

In experiment, the charge carrier density is tuned by applying a gate voltage between the sample and one or more of the gates. On a conceptual level the device functions like as a plate capacitor with TMD and gate as the plates and the hBN insulator layer as the dielectric. The maximum gate voltage that allows operation without breakdown is measured using a lock-in technique (see Fig. 3.4) that captures capacitance and resistance at low resistive currents on the order of pA. A small AC signal with an amplitude of 10 mV_{pp} and a frequency of 77.1 Hz is added to a DC voltage using a passive mixing circuit and fed to a lock-in amplifier as a reference. By monitoring the resistive current through the gate at an increasing DC voltage, the breakdown voltage and thus a safe operating range is determined. Close to breakdown, the resistive current rises exponentially. However, at low currents, the breakdown is still reversible and no permanent changes in the dielectric (reaching from lowering of the breakdown voltage to a full short) are induced. As a rule of thumb, the voltage limit is set at a maximum current of 1 nA to ensure safe operation.

3.2 Low temperature confocal spectroscopy

Optical measurements shown in this thesis consist of confocal photoluminescence (PL), differential reflectance (DR) spectroscopy as well as hyperspectral imaging, all performed using a home-built confocal microscope. The optical setup is shown in Fig. 3.5a. Optical excitation is performed using either a home-build cw-laser or a power-stabilized laser diode at a wavelength of either 660 nm or 670 nm, an incandescent halogen white light source (Ocean optics), a supercontinuum laser (NKT SuperK extreme with NKT Varia filter module) or commercial diode lasers at a wavelength of 530 nm or 633 nm. The light source is coupled into a single-mode optical fiber and subsequently coupled and collimated into the excitation arm of the microscope. The light passes a linear polarizer (Thorlabs) and is filtered using a short pass filter (Thorlabs, Semrock) that prevents low-energy Raman luminescence from the optical fiber to enter the setup. A beam sampler in the beam path reflects ∼10 % of the incoming light and passes 90 %, which is monitored using a photodiode behind the sampler and used for optional power-stabilization. If needed, the reflected beam is circularized using a quarter-wave plate and subsequently enters the cryostat through an optical window. The low-temperature part of the optical setup is kept inside helium exchange gas at a pressure of 10-20 mbar (at room temperature before cool-down). Within this work, either a closed-cycle cryostat (attocube atto1000) or a liquid helium bath cryostat were used for cooling. The light is focused onto a diffraction-limited focal spot using a low-temperature apochromat (attocube). The sample is mounted onto a modular piezo nanopositioner (attocube ANP101x, ANP101z, ANS101 xy, ANP51x, ANP51z, ANS50xy, ANS50z) that allows coarse positioning in-plane with a range of 5 mm (3 mm for ANP51x) at a step size of < 1 μm and fine positioning with a range of 30 μm (15 μm) at sub-nm step size. A second set of positioners hosts a quartz tuning fork (QTF) that is used for low-temperature AFM (see Fig. 3.5b). This module is equipped with a diamond tip (see section 3.3.5 and 3.3) that is placed in the beam path of the objective. In this configuration, the top facet of the tip is placed in the focus of the objective to couple light into the 8 μm long parabolic waveguide which is placed in close proximity to the sample. Light that is emitted or reflected from the sample is collected from the same focal spot and is collimated after passing the objective. The beam then passes the beam sampler again which transmits 90% of the signal into the detection arm of the setup. An equivalent beam sampler (rotated by 90 degrees with respect to the previous one) diverts a small part of the signal to a spy camera that is used to inspect the sample. The rest of the signal passes an analyzing section consisting of either a quarter- or half-wave plate and a linear polarizer, that

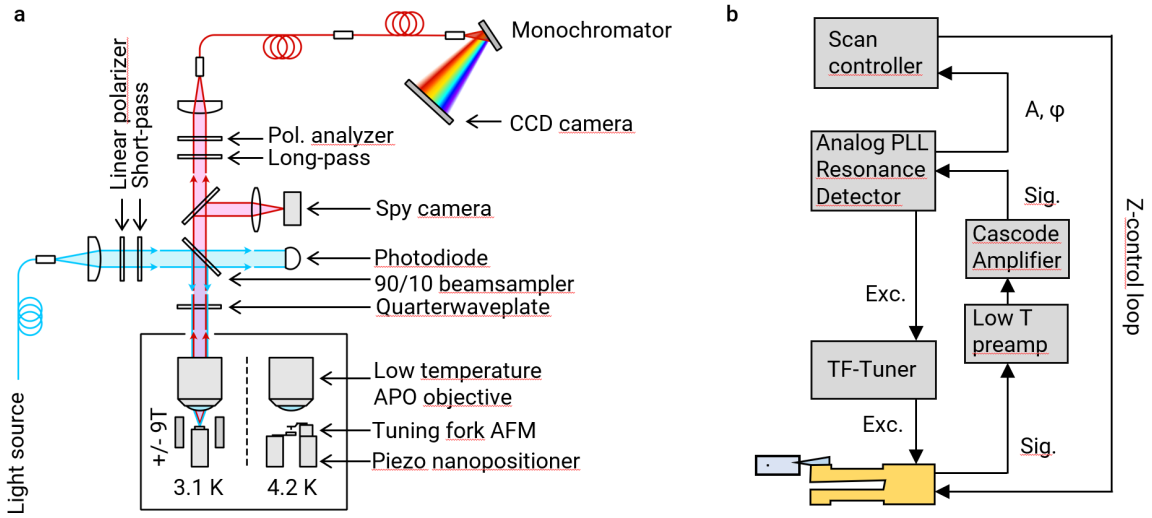

Figure 3.5 Microscopy setup for confocal or tip-assisted optical spectroscopy. a, Schematic of a low-temperature confocal microscope. Light from a narrow or wide band light source is guided through a single-mode optical fiber into one arm of the microscope and is collimated and filtered through a linear polarizer and short-pass filter. A beam sampler reflects up to 10 % through an optional quarter-wave plate and into a low-temperature apochromat which focusses the beam into a diffraction-limited spot on the sample. The sample is mounted on a piezo nanopositioner that can move in all three directions with sub-nm precision. Objective, sample and positioner are located in a closed cycle cryostat at 3.1 K. An alternative setup replaces the objective with a an otherwise similar long working distance apochromat. An additional tuning-fork AFM head is mounted on another nanopositioner next to the sample and is moved independently. This configuration is located inside a helium bath cryostat at 4.2 K. The signal from the sample is collected from the same spot. It first passes the beam sampler a long-pass filter Optionally, a polarization analyzer consisting of wave plate and polarizer is positioned in the beam path as well. Subsequently, the signal is coupled back into a fiber that guides the light into a grating spectrometer. **b,** Schematic of the signal flow of low-temperature tuning fork AFM. A diamond tip is attached to one prong of a quartz tuning fork (gold) which is excited at its mechanical resonance frequency by an analog phase locked loop (PLL) resonance detector. The parasitic capacitance of the tuning fork is compensated by a tuning fork tuner. The electric signal from the tuning fork is amplified by a low-temperature pre-amplifier that is part of a cascode amplifier circuit (see chapter 3.3), that feeds the signal back into the PLL. The PLL can output both frequency and amplitude of the signal to a scan controller that can then lock onto them by varying the vertical distance to the sample.

is aligned with the polarization axis of the excitation beam. Using a long-pass filter, reflected light from the laser is filtered out to allow only PL from the sample to pass. Another collimator focusses the beam into a single-mode optical fiber which guides the signal to a spectrometer consisting of a grating monochromator (ARC Acton 300i, Princeton Instruments Acton SP2500) and a cooled CCD-camera (Princeton Instruments Spec10, Andor iDus). For DR spectroscopy, long-pass and short-pass filter are removed to directly observe the reflected light from the sample.

3.3 Tuning fork atomic force microscopy

Quartz tuning fork atomic force microscopy (QTF-AFM) is a microscopy technique that, similar to AFM, measures sample properties through interatomic forces acting on a tip. However, instead of a cantilever, it uses a piezoelectric quartz tuning fork (QTF) that is sputtered with gold electrodes [111]. Compared to the cantilevers of conventional AFM systems, the comparatively large QTFs have a higher stiffness. Combined with the low mechanical vibration loss of quartz, this results in a high and robust quality factor Q, even at ambient conditions. Commercially available QTFs that are packaged in an evacuated housing show an even higher Q. These devices are broadly used as a frequency standard in e.g. quartz watches, making them available cheaply and in large numbers.

For AFM, the high stiffness has two implications. At a given force acting on the tip, a higher stiffness results in less deflection and therefore a weaker signal [112, 113]. At the same time however, the snap into contact, which is exhibited by softer cantilevers, is reduced. As a result, dynamic mode AFM can be performed at lower oscillation amplitudes. This is beneficial for applications that require the precise positioning of a probe very close to a sample such as scanning near field optical microscopy [114–117] or nano magnetometry [118].

In operation, the main difference between QTF and conventional cantilevers in commercial AFM systems is that a force acting on the piezoelectric quartz directly translates into an electrical voltage and current between the two electrodes. By relying on these electrical signals, all different modes of AFM is realized. However, the low strength of the electrical signal at low forces, combined with the stiffness and high quality factor render QTFs less useful for static and especially useful for dynamic AFM. With an oscillating QTF, sensitive lock-in techniques and other filtering methods are used to detect even very weak signals. DC drifts on the other hand, which can arise from various sources, e.g. slight fluctuations in ambient temperature, play a

minor role.

3.3.1 Mechanical model

A QTF is described as a mechanical oscillator, with a spring constant K and an oscillator mass m. The tip is assumed to move orthogonally to the sample surface, as would be the case in a configuration, where the two prongs of the QTF are aligned on an axis perpendicular to the surface. This case also generalizes to oscillation parallel to the surface. The following mechanical analysis is summarized from [113]. The movement of the tip in z-drection $z(t)$ is described by a driven and damped harmonic oscillator:

$$m\ddot{z} = -K(z - z_0) - \gamma\dot{z} + F_{\text{int}}(z) + F_{\text{exc}}(t), \tag{3.2}$$

with the equilibrium position z_0, the dampening constant γ, the excitation force F_{exc} and the interaction force with the sample F_{int}. When assuming that the dampening and excitation compensate each other, the energy of the system is conserved and is given by the Hamilton function:

$$H = \frac{p^2}{2m} + \frac{m\omega_0^2}{2}(z - z_0)^2 + U_{\text{int}}(z), \tag{3.3}$$

where p is the momentum of the oscillator, $\omega_0 = \sqrt{K/m}$ its undisturbed resonance frequency and $U_{\text{int}} = -\int_{\infty}^{z} F_{\text{int}}(z)dz$ is the interaction potential, derived from the sample-tip interaction force F_{int}. If the external force component f is constant, the interaction potential is linear and is written as:

$$U_{\text{int}} = fz. \tag{3.4}$$

In this case, only the mean position of the oscillator is shifted while the resonance frequency is unaffected. Assuming a force that is linear in z, the potential becomes quadratic.

$$U_{\text{int}} = K_{\text{int}}z^2, \tag{3.5}$$

where K_{int} results in an effective shift of the spring constant K and alters the resonance frequency.

$$\omega = \sqrt{\frac{K + K_{\text{int}}}{m}}, \tag{3.6}$$

which is interpreted as a change in stiffness as the sample forces act on the tip and the TF. This oscillator model gets more complicated when introducing a physical tip that is

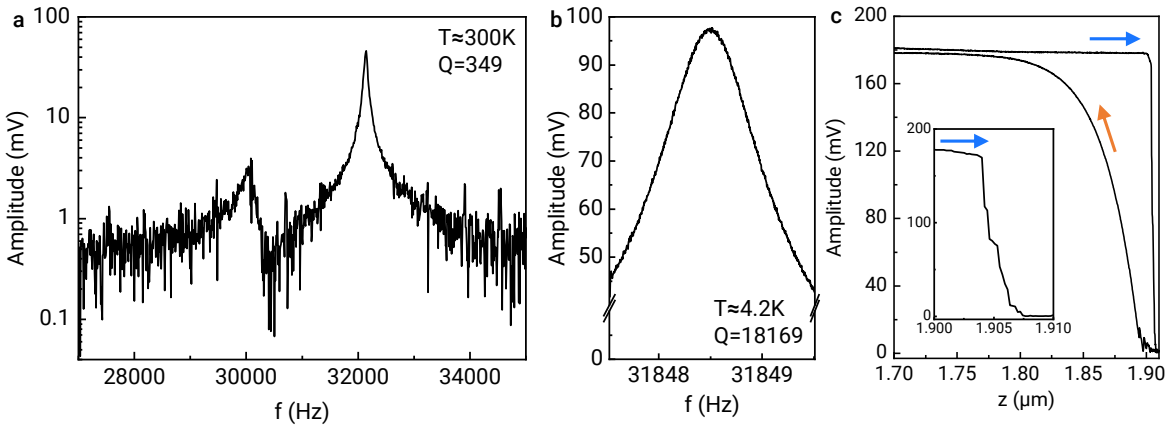

Figure 3.6 Properties of an unbalanced QTF. a, Frequency response of the QTF at room-temperature. **b,** Frequency response of the QTF at liquid helium temperature. **c,** Approach and retraction curve showing amplitude in relation to z-piezo extension and a zoom into the high-extension portion of the approach. Colored arrows indicate the sequence of data acquisition in time. The total acquisition time is 100s.

mounted to only one of the two prongs of the QTF. As the mass of the tip creates an imbalance, describing the QTF by a single harmonic oscillator is insufficient. Therefore, the next step is to describe the QTF using two coupled oscillators with different mass parameters, resulting in two unequal symmetric and antisymmetric modes. However, this description is still unable to explain all experimental observations, specifically a strong difference in quality factor between the synchronous and asynchronous modes. This problem is overcome by introducing a third mass representing the base that connects the two prongs. The synchronous mode, where both prongs move together, also results in movement of the base, dampening the oscillation and thus resulting in a lowered quality factor [113]. In this model, the TF has three oscillation modes: A high frequency, low Q mode for the base movement and the split pair of the synchronous and asynchronous mode. It is found that for a very small imbalance the higher frequency mode can have a quality factor that lies multiple orders of magnitudes higher than the lower one. However, as the mass increases, both Q converge.

In our own experiment we found a quality factor of Q=349 (see Fig. 3.6a) at room temperature for the main higher energy mode, indicating a strong imbalance compared to a typical Q of $\sim$ 10000 for a balanced QTF. However, this significantly alters at experimental conditions near vacuum at low-temperatures. Fig. **??**b shows the resonance curve of the same mode at 4.2 K and helium exchange gas pressure of below 1 mbar with an increased quality factor of Q=18169. The higher quality factor is also

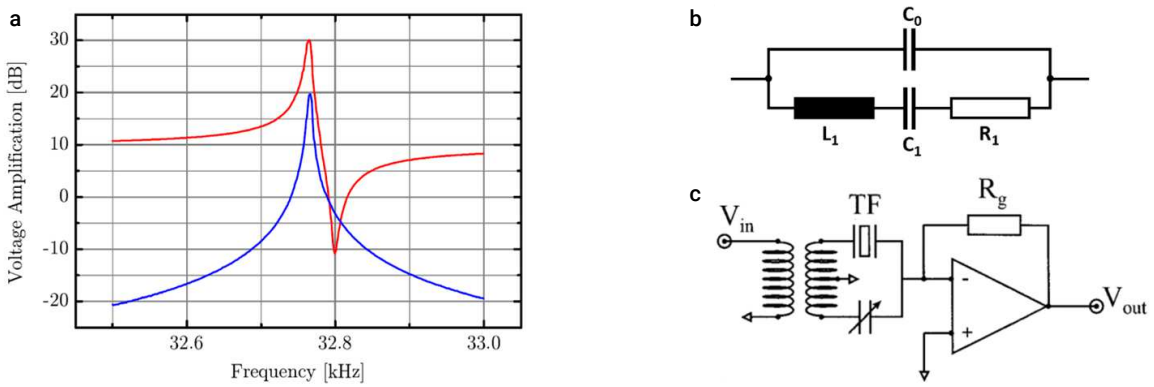

Figure 3.7 Tuning fork tuner. a, Resonance curve for an electrically excited quartz tuning fork with (blue) and without (red) compensation of the TF stray capacitance. **b,** Equivalent circuit of the tuning fork with the mechanical resonance represented by an equivalent RCL-circuit (C_1, R_1 and L_1) and the stray capacitance (C_0). **c,** Schematic for an idealized tuning fork tuner consisting of a transformer with two secondary windings that connect to the TF on one arm and to a variable capacitance on the other.

reflected in the approach behaviour when bringing the tip in contact with the sample (see Fig. 3.6c). The curve shows an approach in a total time of 100 s. As shown in the convex, lower-amplitude retraction section of the approach, the system takes almost 50 s to completely reach the unperturbed amplitude after quenching it on contact, reflecting the slow reactivity of a high Q oscillator.

3.3.2 Electrical model

For dynamic AFM, the QTF has to be excited to oscillate at or close to its resonance frequency ω_0. A conventional AFM cantilever is typically excited mechanically through an oscillating piezo dither. While this is equally feasible with a QTF, the more elegant solution is to use electric excitation. In this configuration, both excitation and signal detection are accomplished using the same electrical connections. This saves space in the closed space of the cryostat and results in a more defined relationship between electrical and vibrational amplitude in contrast to a dither.

When excited electrically, a QTF is modelled using an equivalent circuit, called the Butterworth-Van Dyke equivalent circuit for a piezoelectric resonator (see Fig. 3.7). In this representation, the electro-mechanical QTF resonator is described by an *RCL* resonator that is wired in parallel to a parasitic or stray capacitance. The QTF resonance f_0 and the corresponding quality factor Q are written in terms of the corresponding

inductance and capacitance:

$$f_0 = \frac{1}{2\pi\sqrt{LC}}, \tag{3.7}$$

$$Q = \frac{f_0}{\Delta f} = \frac{1}{R}\sqrt{\frac{L}{C}}. \tag{3.8}$$

The current running through the parasitic capacitance C_p on the other hand is defined by the parasitic resonance:

$$f_p = \frac{1}{2\pi\sqrt{L\frac{C\cdot C_p}{C+C_p}}}, \tag{3.9}$$

As this capacitance is connected in parallel, the response is reversed with respect to the resonance at f_0, thus forming an anti-resonance. As indicated in Eq. 3.9, the relationship between f_0 and f_p only depends on the ratio between C and C_p. The two frequencies align closest when the term $C_p/C + C_p$ is close to unity, which is the case if C_p is much larger than C.

A method to obtain values of R, C and L is the measurement of the impedance of the QTF, previously performed in [119]. The authors of this study used an amplification circuit with a known frequency dependent gain Z_g, which was mounted close to the QTF to measure its frequency response through the resonance. The resulting curve follows a lorentzian lineshape.

$$Y(f) = A\frac{f_0}{Q}f \Bigg/ \sqrt{(f_0^2 - f^2)^2 + \left(\frac{f_0}{Q}f\right)} \tag{3.10}$$

By fitting this line shape to the measured data points, they found values of $A = 17.14$, $f_0 = 32773.3$kHz and $Q = 8552$, resulting in

$$\begin{aligned} R &= Z_g/A = 0.494\text{M}\Omega, \\ L &= RQ/2\pi f_0 = 20.5\text{ kH}, \\ C &= 1/(4\pi^2 f_0^2 L) = 1.14\text{ fF}. \end{aligned}$$

Considering a typical QFT parasitic capacitance of $\sim$ 1 pF, this results in the ratio $C_p/(C + C_p) \sim 0.999$, bringing the anti-resonance f_p in close proximity of below 100 Hz to f_0 (see Fig. 3.7). This poses a challenge to using the QTF in a distance control loop, as neither amplitude nor phase are monotonous upon a shift in its resonance frequency.

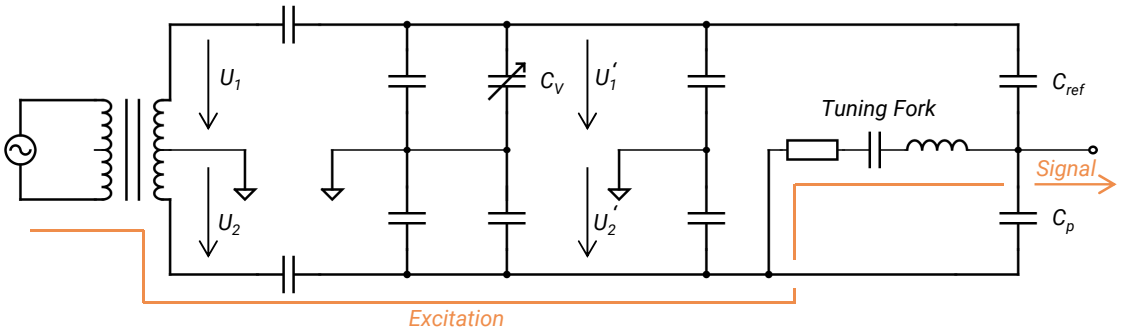

Figure 3.8 Schematic of tuning fork tuner circuit. The excitation signal is coupled into the circuit through a transformer with a center tap to ground, splitting the signal into equal voltages U_1 and U_2, phase-shifted by 180 degrees. The top arm is filtered by a variable capacitor C_V – creating an imbalance between the modified voltages U_1' and U_1' – and a reference capacitor C_{ref}. The bottom arm guides the signal to the tuning fork, represented in the Butterworth-Van Dyke model by an *RCL* oscillator and a parallel parasitic capacitance C_p.

Therefore, the parasitic capacitance is compensated in a process called "tuning". The corresponding principle is illustrated in Fig. 3.7b and a more detailed circuit diagram is shown in Fig. 3.8. The underlying idea is to split the excitation signal in two signals U_1 and U_2 of equal amplitude but phase-shifted by 180 degrees with respect to each other. This is achieved by a transformer that is center tapped to ground. One arm includes a capacitive filter (upper arm in Fig. 3.8), that is tuned by a variable capacitance C_V. From there the signal is guided to a reference capacitance C_{ref}, that is chosen with a value close to that of the C_p, in our case 1 pF. The other arm guides the actual excitation signal that runs through the QTF, depicted in Fig. **??** in its Butterworth-Van Dyke representation. If C_{ref} were to perfectly match the value of C_p, both signals through the upper arm and through C_p would be identical in amplitude and opposite in phase, cancelling at the output node, leaving only the electromechanical signal from the oscillating QTF. However, variations from non-identical tuning forks and additional parasitic capacitances from e.g. long wires prohibit the precise tuning of the circuit purely through the choice of C_{ref} which would anyway be unfeasible to be obtained with an arbitrarily precise value. Instead C_V is used to tune the circuit in situ with the help of a network analyzer, as shown in Fig. 3.7a. The red line shows the frequency response of an untuned QTF circuit whereas the blue line shows the same response with C_V adjusted to eliminate the anti-resonance.

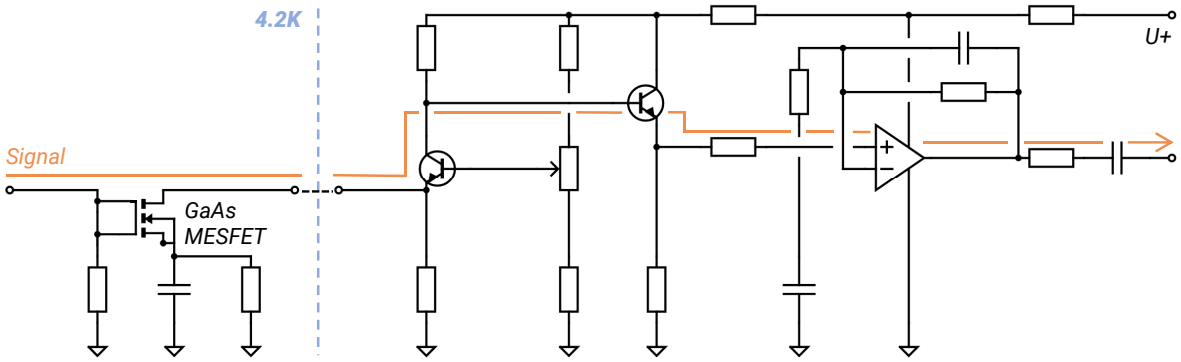

Figure 3.9 Schematic of a low-temperature cascode amplifier. The circuit is divided into two parts. The low-temperature stage consists of a high-impedance pre-amplifier that connects to a low-impedance stage at room temperature. The buffered output from the cascode is then further amplified through an operational amplifier.

3.3.3 Signal detection

A vibrating quartz tuning fork produces small currents in the order of 1 µA or lower [120], depending on the excitation amplitude. As the QTF is separated from ambient conditions by long (1-2m) coaxial cables with a typical capacitance in the order of 50 pF/m. This capacitance limits the bandwidth and this effect is exacerbated by the Miller effect, when the signal is amplified. Therefore the scheme to measure the vibrational signal of the QTF is required to limit the effect of the parasitic capacitance. One approach is to amplify the signal using a charge amplifier. A charge amplifier is a circuit that transforms the total injected charge directly into a voltage. Owing to its design, the input impedance of an ideal charge amplifier is zero and currents generated in the QTF will flow into the amplifier without being affected by any parallel capacitance.In a non-ideal physical implementation, the impedance depends for example on the quality of the operational amplifier used in the circuit. Still, modern operational amplifiers tolerate several thousands of pF of capacitance, corresponding to at least hundreds of meters of cable. However, this does not come without its own limitations. While the parasitic cable capacitance does not impact the signal in a static system, the charge displacement from a cable in motion can easily overpower the small signal from the QTF. Therefore, great care has to be taken to limit the cable length and to keep them mechanically stable. This is achieved by mounting a charge amplifier with a low footprint (e.g. Femto HQA-15M-10T) in close proximity to the cryostat and use short and rigid cables to connect to the microscope system.

An alternative is a specialized amplifying circuit, the so-called cascode amplifier. A

cascode uses a two-stage design to eliminate the Miller effect and as a result allows amplification at a higher bandwidth. The basic design consists of two transistors (Bipolar or field effect), a first stage in common emitter or common source operation and a second operating with a common base or common gate. The second stage has very low input impedance, eliminating the influence of the parasitic capacitance of the signal path between the two stages. The consequence of this is however, that the first high impedance stage of the amplifier has to be as close to the QTF as possible and has thus to be designed for operation at liquid helium temperature. The second stage operates at room temperature and is therefore less constrained. A simplified diagram of the circuit used in this work is shown in Fig. 3.9. The first stage of the cascode is realized by a self-biased GaAs MESFET (Sony SGM2016P) in common source operation. This transistor is chosen for low-temperature operation as normal silicon-based transistors are limited to higher temperatures owing to charge carrier freeze out [121]. While the use of silicon transistors in cryogenic environments is possible in principle, it is required to keep the transistor junction itself at a sufficiently high temperature, for example by supplying the amplifier circuit with operating voltage throughout the cool-down or by including a heating resistor in physical proximity to the transistor. Both of these methods, however, introduce additional complexity and potential sources of error.

From the low-temperature stage, the signal enters the second, low-impedance stage that is realized by one channel of a dual bipolar junction transistor (BJT) in common base operation. From there, the signal runs through the second channel of the BJT which acts as a buffer, and enters an additional amplification stage, realized using an operational amplifier which provides an additional voltage gain of 10.

3.3.4 Distance control

AFM relies on specific methods to accurately position the tip in close proximity to the sample surface with sub-nm precision. Physically, this is achieved through a piezo positioner, that moves the sample in z-direction with respect to the tip (see Fig. 3.5a). Depending on the measurement requirements, this is reversed such that the sample is static and the tip is positioned, respectively. Electronically, the distance is tuned by a *PI*-control loop, relying on either amplitude, phase or frequency as an error signal (see 3.5b). In our experiments, this control loop is implemented by a digital scanning controller (attocube ASC500). The simplest scheme is to excite and detect the response of the QTF at a fixed frequency and directly feed the amplified QTF signal to the control loop. For apparent reasons, this technique only allows amplitude modulation (AM) operation, but is a viable option for both room and low-temperature operation. Addi-

tionally, the amplitude-distance response is strictly monotonous when the excitation is performed at the free resonance frequency of the QTF, lowering the chance of destructive control loop errors that push the tip into the sample. A more complex approach utilizes an analog resonance frequency detector based on a phase-locked loop (PLL). This detector uses an internal control loop to lock the phase angle between excitation and detected signal to a setpoint. This value is tuned by hand to the resonance frequency by maximizing the measured amplitude of the signal, which reaches its peak at the resonance.

The advantage of using this system is twofold. Because the PLL is able to directly measure the resonance frequency of the oscillation, it is possible to use it as feedback for the distance control loop, enabling frequency modulation (FM) operation. Additionally, the amplitude of the signal is always measured at the maximum of the resonance. It therefore drops less quickly under the influence of atomic forces compared to fixed frequency operation where the signal is sampled from the slope as the peak shifts to higher values. This enables operation at a higher dynamic range and lower amplitudes while maintaining a superior signal-to-noise ratio. However, at large tip deflections, the signal eventually drops below the noise level. In this case, the PLL is at risk of locking to a different signal, e.g. from external interference. At this point, the control loop is unrecoverable and depending on the strength of the interfering signal, the piezo will be driven either to minimal or maximum extension, possibly damaging tip or sample. This can partially be mitigated by operating close to the maximum extension of the piezo such that even at maximum extension the force output is limited. In microscopy, this effect is avoided by choosing an appropriate setpoint far above the noise threshold. For typical AM operation, this is chosen to be above 50% of the free amplitude.

Initial approach

The described positioning techniques require that the tip is already in close proximity to the surface of the sample. This distance is given by the maximum range of the scanning piezo, 2 µm in this work. To approach the sample safely, sample and tip are mounted on piezo positioners with a larger stepsize but longer range (see above). Throughout this process the QTF is excited at a fixed frequency while monitoring the amplitude. The approach starts with the sample being moved by a fixed sequence of steps, roughly corresponding to the full range of the scanning piezo. Next, the scanning piezo is extended. The process is repeated until a drop by more than 40 % is detected after which the scanning piezo is disengaged. At this point, the sample is

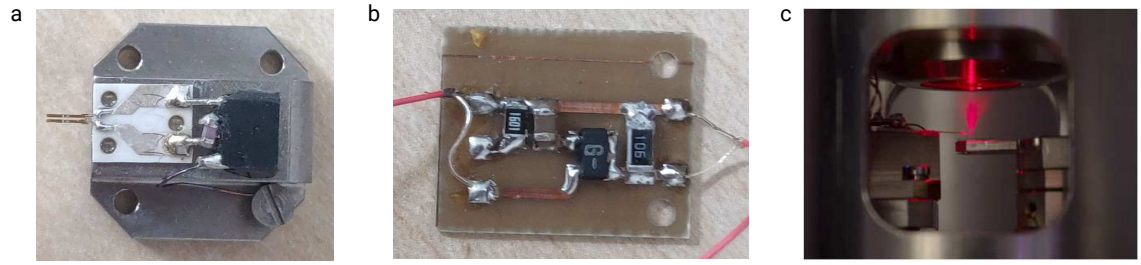

Figure 3.10 Parts used in QTF-AFM. a, Photo of a quartz tuning fork with diamond tip with electrical connections on a titanium holder. **b,** Photo of the low-temperature stage of a cascode amplifier, mounted close to the QTF. **c,** Photo of both sample and QTF mounted in a low-temperature micoscope setup.

in range and the control loop is used to adjust the distance.

3.3.5 Scan head fabrication and assembly

Scanning probe techniques can utilize a wide variety of probes and tips with different properties that depend on the quantity to be measured in experiment. For this thesis, the main goal was to observe the effects of local strain on the optical spectrum of WSe_2 monolayer samples. Standard AFM tips etched from silicon are well suited to apply strain and are commercially available, already mounted to a QTF system (NANOSENSORS Akiyama Probe). However, they are opaque and thus don't allow direct optical observation at the point of strain. An alternative is to use tips made from a transparent material such as diamond [122]. The type of diamond tip used in this work is not only transparent to visible light but also acts as a waveguide that guides light from and to the top and bottom tip facet, increasing excitation and collection efficiency [122]. This tip, which is attached to a scan head, containing QTF, printed circuit board (PCB) and a titanium holder (see Fig. 3.10a) is fabricated by our collaborators [122] (Quantum Sensing Lab, University of Basel). It consists of a micropillar with a length of 6 µm and a parabolic cross section (see Fig. 3.11d). It is attached to a rectangular diamond cantilever with a thickness of 2 µm. At its thickest part, the pillar has a diameter of 900 nm, narrowing gradually towards a flat facet with a diameter of 300 nm. The cantilever is mounted to a narrow glass capillary which in turn is mounted to one prong of a QTF. The QTF itself is soldered to a small PCB that fans out towards two larger solder pads and is used to electrically connect the QTF as described in the previous

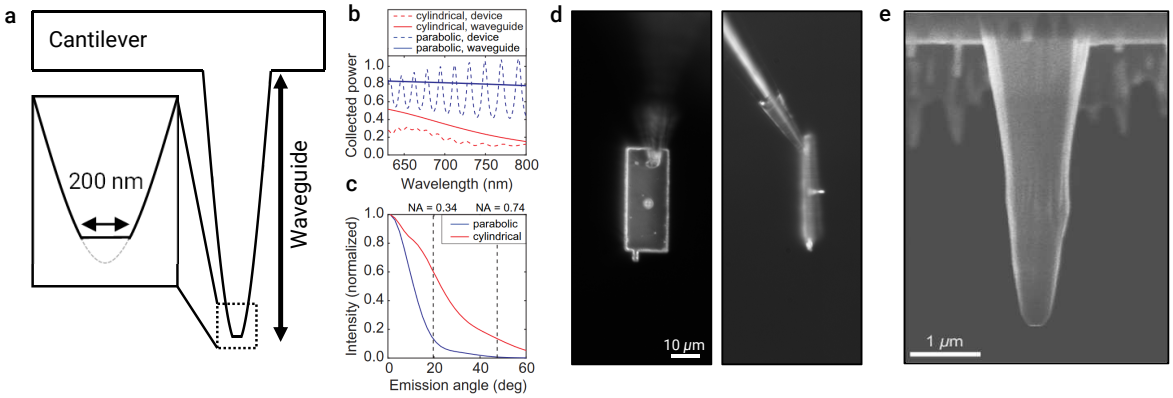

Figure 3.11 Diamond tip properties. **a,** Schematic drawing of a diamond cantilever with a parabolic waveguide. The waveguide ends in a flat facet with a diameter of 200 nm that is close to the focal point of the parabola. **b,** Simulated device performance of a parabolic waveguide (blue) to a cylindrical (red) showing the ratio of power emitted into a NA of 0.8, to the power emitted by a bulk dipole. This ratio is shown for the waveguide alone (solid) and the entire device (dashed) as a function of wavelength. **c,** Normalized, integrated photoluminescence from a N-V emitter implanted below the bottom of the parabolic (blue) and cylindrical (red) waveguide. **d,** Dark field images of the finished device from top (left) and side (right) view. **e,** SEM image of the parabolic waveguide. **b, c, e** Figures adapted from [122]

section. Two pins of a 4-pin connectors are soldered to the pads carrying the excitation and detected signal, respectively. A third pin is coupled to the detection signal with a 1 pF reference capacitor which is directly soldered to the two pins. It carries the phase-shifted excitation signal. The forth pin connects to ground and is in contact with the metallic scan head. When using a charge amplifier (Femto HQA-15M-10T) at room-temperature for signal readout, the head directly connects to four coaxial cables with their shields connected to a common ground. When using a cascode amplifier, the detection signal connects to to the first stage of the amplifier instead (see Fig. 3.10b). Finally, both sample and scan head are mounted to two sets of piezo positioners close to the focus of a long working distance, low-temperature objective (see Fig. 3.10c and 3.2)

Tip fabrication

This paragraph is summarized from [122, 123].

Diamond tips incorporating nitrogen vacancy centers (NV) are primarily used for single-spin magnetic field measurements [122]. The devices used in this thesis originate from the same process, but are made from inert samples that failed to incorporate

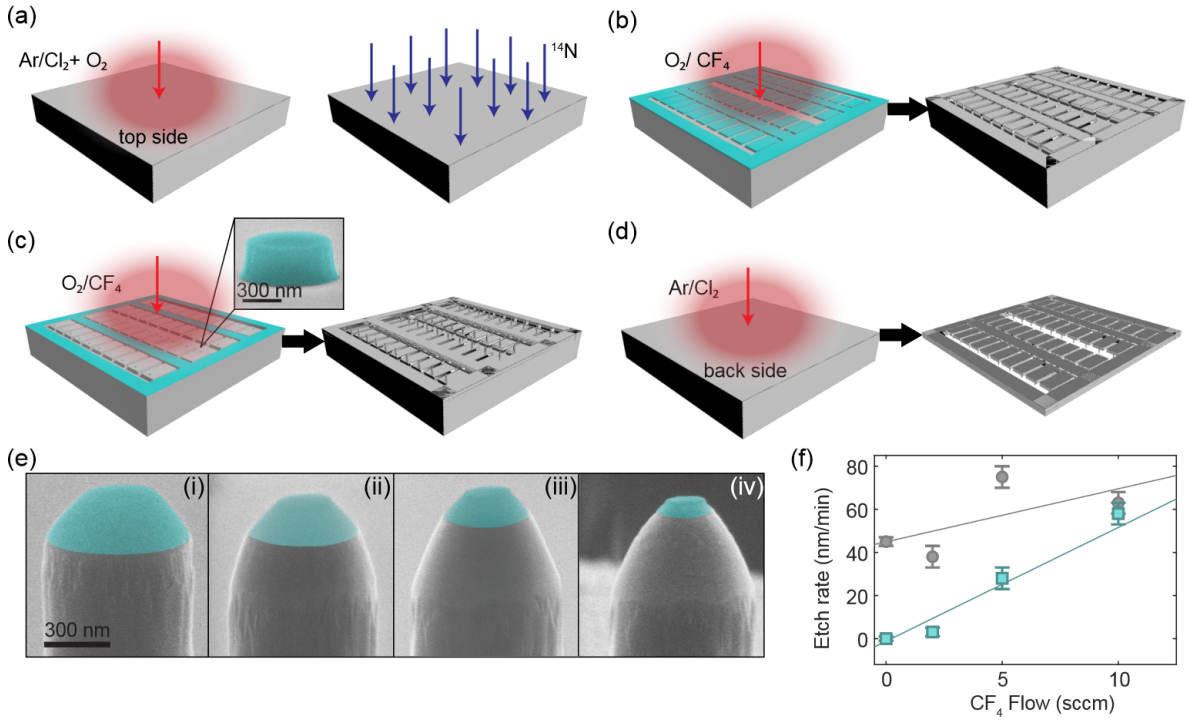

Figure 3.12 Fabrication process for parabolic diamond micro-pillars. a, A raw diamond slab is prepared by a stress-relieving etch of Ar/Cl_2, implanted with ^{14}N and annealed in vacuum at 1200 °C. **b,** The diamond is covered with a flowable oxide polymer mask and patterned by electron-beam lithography to create a cantilever array and holding structure. The diamond is then etched by O_2/CF_4 plasma. **c,** Pillars and holding structure are defined and etched using the same process. Subsequently, using pure CF_4 at variable flow-rates, the rounded tip cross section is defined. **d,** Cantilevers are released from the substerate by Ar/Cl_2 etching. **e, f** Details of the etching process using variable CF_4 flow rates to control mask erosion and thus the tip-shape of the pillar. Figure adapted from [122]

an NV. However, as the pillars allow efficient optical coupling to an emitter close to the bottom facet, they are well suited to study samples in close proximity to the tip. The fabrication process is depicted in Fig. 3.12. The starting point is a diamond slab, that is laser-cut and polished to a thickness of 50 µm (Element Six, $[N] < 5$ ppb, (100) surface). This wafer is thinned down using Ar/Cl_2 plasma and subsequently implanted with 2 $\times 10^{11}$ cm^{-2} ^{14}N at 12 keV and 7° tilt to the sample normal, resulting in an estimated N depth of 20 nm. After the implantation process, the sample is annealed at 1200 °C in vacuum. In the next step, an array of cantilevers and a holding structure is patterned into a ~300 nm thick film of flowable oxide resist (FOX-16, Dow-Corning) using e-beam lithography. Subsequently, the pattern is etched into the diamond via

ICP-IRE to a depth of 2 μm. The pillars are etched from the top using another flowable oxide mask using alternating O_2 and CF_4 etching which results in trapezoidal pillars with a diameter of 900 nm at the base and a length of ∼6 μm. The next step is performed with pure CF_4. By varying the flow rate, the etching of the diamond and the erosion of the flowable oxide resist is varied to control the steepness of the trapezoidal profile. By successively increasing the flow rate the tip is shaped into a rounded dome. The end faced remains flat with a diameter of ∼200 nm. The back side of the cantilevers is still connected to the diamond substrate which is etched down from the back side to release the cantilevers through the previously etched trenches. The only connection to the holding structure is a small holding bar that keeps the cantilevers attached to the structure until they is transferred to a QTF. This is achieved by a narrow glass capillary that is tapered to a point on one end using a capillary puller. The thicker end of the taper is attached to one prong of the QTF at a forward and down facing angle and glued in place with UV-hardening adhesive. Once hardened, the long end of the capillary is carefully broken off. The tip of the capillary is glued to a diamond cantilever in the same way which is afterwards broken out of the panel and ready to be used.

4 Spectroscopy of tungsten dichalcogenides with controlled doping

The following chapter describes experimental results on charge tunable tungsten dichalcogenides. The first section focusses on monolayer and bilayer WSe_2 which is studied by means of spectroscopy in magnetic field. The measured g-factors give insight into the origin of the exciton spectrum which is compared to the theoretical model described in Chapter 2. Subsequently, the spectrum of WS_2 is studied and interpreted leveraging the insights from the previous experiment.

4.1 Spectroscopy of tungsten diselenide mono- and bilayers in magnetic field

Part of this section is adapted from the publication

Förste, J. *et al.* Exciton g-factors in monolayer and bilayer WSe_2 from experiment and theory. *Nat. Commun.* **11,** 4539 (2020)

Spectroscopy in magnetic field represents a powerful tool to study the band structure of TMDs as the splitting of spectral lines, the valley-Zeeman effect (see chapter 2) is characteristic for different species of excitons that have their origin in charge carrier population at different crystal momenta. The experiment described in the following section was used to determine the g-factor for various features in the spectrum of a charge-tunable WSe_2 mono- and bilayer. These values are discussed and compared to DFT calculations (see sec. 2.4) to determine the origin of these spectral lines.

The experiment was performed in a sample of WSe_2 mono- and bilayers in a field-effect structure, allowing electrostatic doping. The sample, as schematically shown in Fig. 4.1a was fabricated from exfoliated WSe_2 and hBN. Gate control was realized using lithographically fabricated gold contacts that were deposited on the substrate prior to the stamping process. The p-doped Si of the substrate was used as a back-

gate. A more detailed description of the fabrication process is presented in Chapter 3.1. Gate voltages are supplied by a precision voltage source (Yokogawa 7653) which allows voltages between ±32V. The maximum applied gate voltage, however, was limited by the dielectric strength of the 50 nm oxide layer of the silicon substrate, which amounted to a boundary of only ±15V. Through the course of this experiment, the sample is cooled to 3.2 K in a closed-cycle cryostat (attocube atto1000) and probed with cw-laser excitation at 1.85 eV, close to the 2s-resonance of the A-exciton and at powers insufficient to excite neutral or charged biexcitons [124–127]. This cryostat is also equipped with a bi-directional superconducting solenoid allowing homogeneous magnetic fields of up to 9 T in the Faraday configration.

The most important points in the Brillouin zone are schematically shown in Fig. 4.1b. Fig. 4.1c,d show the spectrum for representative spots on the sample for both monolayer and bilayer across the neutral and negative charge regime. As can be seen, the transition between neutral and negative doping happens at approximately –5 V, which is consistent with intrinsic, residual *n*-doping of the exfoliated WSe_2 flake [128, 129].

In the monolayer, the neutral regime is characterized by the neutral bright A-exciton (X^0) at 1.72 eV and redshifted peaks labeled M_1^0,M_2^0, and M_3^0 with red-shifts of 35, 60 and 75 meV compared to X^0. The dark exciton (D^0) with a redshift of 42 meV [55, 130, 131] can only be observed as a weak signal at the shoulder of M_1^0. Positive gate-voltages result in the accumulation of electrons in the sample and thus negative doping. This regime is characterized by the appearance of a bright trion doublet (X_1^- and X_2^-) exhibiting an exchange splitting of ∼6 meV [129], the dark trion D^- redshifted by 28 meV in relation to X_1^- [132–135], and a similar series of low-energy peaks, lead by M_1^- at 44 meV redshift [134, 135].

In the bilayer (Fig. 4.1d), the photoluminescence is characterized by multiple peaks that show an energy of >100 meV below X^0. The charging behavior and the onset of the neutral/negative regime is consistent with that of the monolayer case. The peaks, numbered from higher to lower energy B_1^0 through B_3^0, as well as their negatively charged counterparts B_1^- through B_3^-, correspond to phonon sidebands of momentum-indirect excitons. The transition from neutral to negative doping is marked by a global redshift of 22 meV, that, close to the transition in the monolayer, occurs at –7 V. The lowest lying valley in the bilayer is located at the six inequivalent *Q*-points, coinciding with the field-induced electron concentration. The picture is, however,Rlabeled more complicated in the valence band, where in the bilayer, the *K* as well as the Γ valley are energetically nearly degenerate. This complicates the attribution of *QK* or *Q*Γ excitons

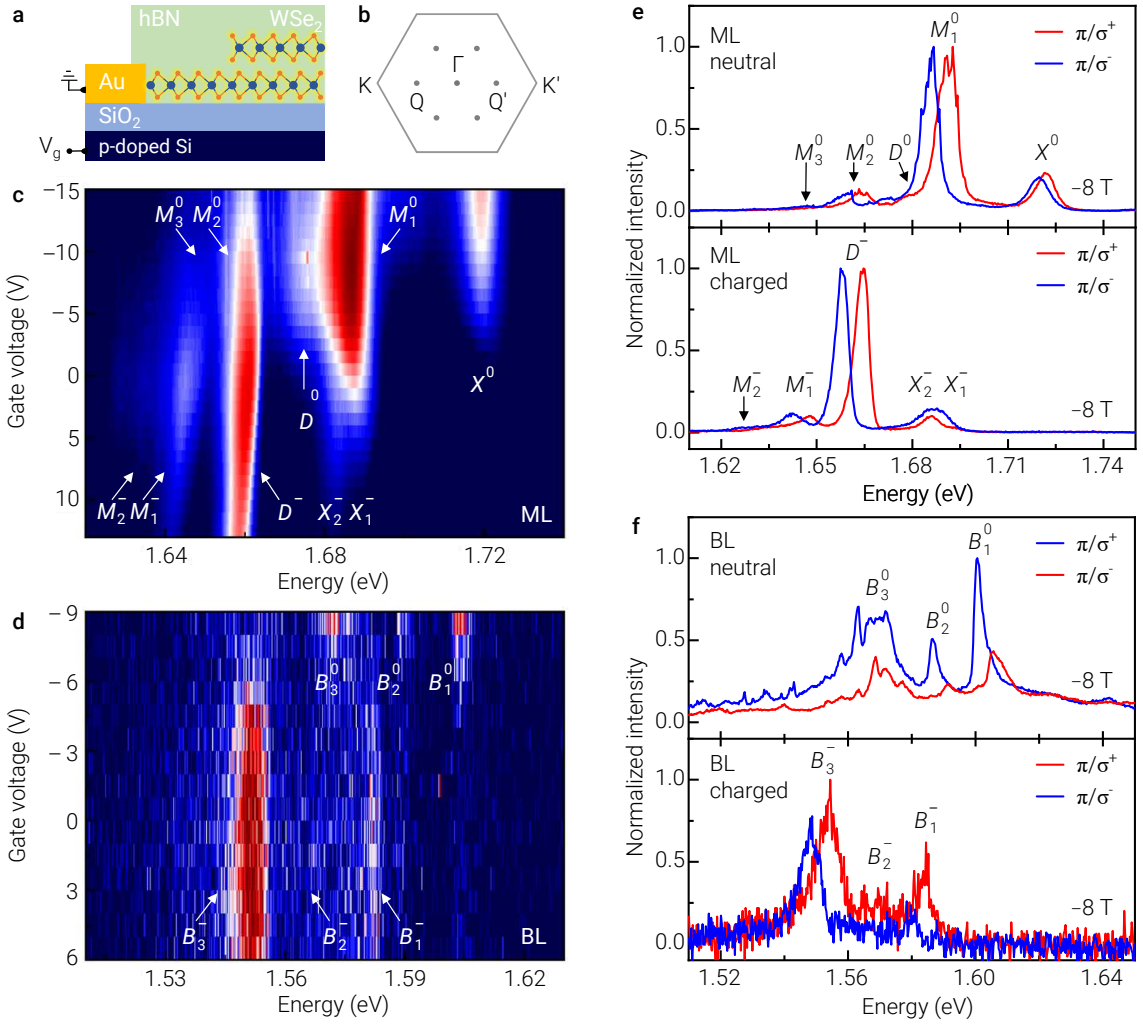

Figure 4.1 Magneto-optic measurements for different doping regimes. **a,** Schematic of the combined WSe_2 mono-/bilayer sample with electrostatic gate control. A gate voltage can be applied between the sample, mechanically contacted through a lithographically fabricated gold electrode, and the *p*-doped silicon substrate, separated by 50 nm of thermal oxide and ~100 nm of hBN. **b,** Schematic of the first Brillouin zone of WSe_2, including the most relevant high symmetry points. **c, d** Logarithmic false-color plot of photoluminescence intensity as a function of gate voltage at representative points on the sample for WSe_2 mono- and bilayer, respectively. The monolayer shows characteristic photoluminescence of the neutral bright (X^0) and dark (D^0) excitons as well as their negative counterparts, the negatively charged exchange split trion doublet $(X_1^-$ and $X_2^-)$ and the dark trion (D^-). Other peaks in the spectrum that belong to the monolayer (M) or bilayer (B) are labelled according to their charge state in the superscript and with increasing numbers from higher to lower photoluminescence energy in the subscript. **e, f** Neutrally and negatively charged spectra at $(+/-)$ 8 T for both mono- and bilayer WSe_2, respectively. Every plot shows the same spectrum measured in the circular right (blue, σ^-) and left (red, σ^+) handed bases upon linear (π) excitation.

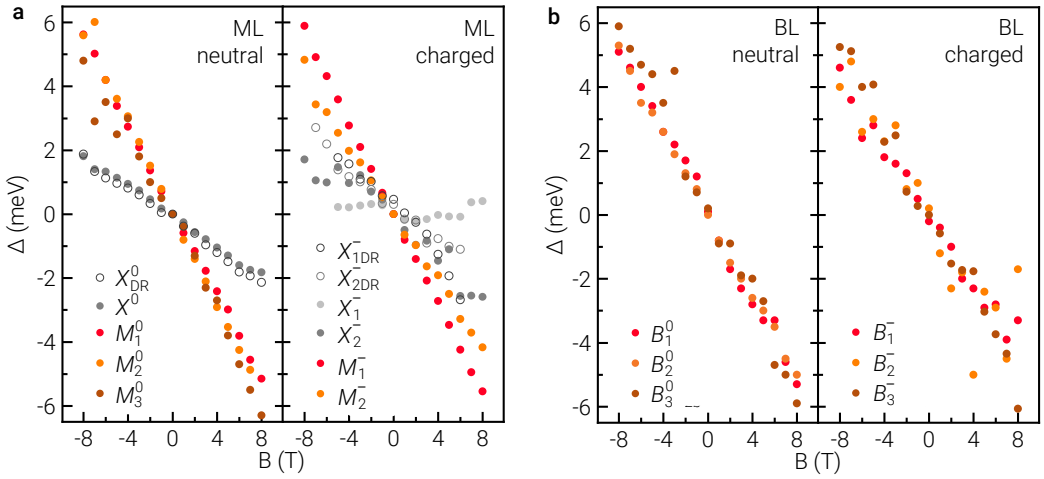

Figure 4.2 Valley Zeeman splitting in monolayer and bilayer WSe_2. **a, b** Valley Zeeman splitting Δ between (+/−) 8 T perpendicular magnetic field for mono- and bilayer respectively in neutral (left subpanel) and negative (right subpanel) regime in photoluminescence (filled circles) and differential reflectivity (empty circles).

and trions to their respective PL peaks as well as their energetic ordering [39].

As discussed in chapter 2, different valleys and thus different exciton species exhibit a differential valley Zeeman response to an applied magnetic field in the form of characteristic exciton g-factors [86, 87, 136–139]. Thus, spectroscopy at magnetic fields is a viable tool to differentiate unknown peaks in the spectrum. Upon linear (π) excitation, defined by a fixed linear polarizer (Thorlabs LP), a superposition of both K and K' valleys is excited, which, in absence of strong valley coherence, decays into an equal mix of right- and left-handed circularly polarized light. To measure the differential energy shift, the PL spectrum is be measured in a circular basis (σ^+, σ^-), defined by a quarter wave plate (B-Halle superachromatic 200-1100 nm) and a linear polarizer (Thorlabs LP) set to the same axis as in excitation. At zero field, all valleys are energetically degenerate with their opposite-valley counterparts and the spectrum looks identical in each measurement basis.

When a magnetic field is applied in the vertical z-direction, as shown in Fig. 4.1e, f, the degeneracy is lifted with the splitting $\Delta_B = E_{\sigma^+} - E_{\sigma^-}$ – with peak energies $E_{\sigma^{+/-}}$ recorded under $\sigma^{+/-}$ polarized detection – at any finite field directly corresponding to the g-factor according to eq. (2.9) . This degeneracy is however lifted upon applying a magnetic field in z-direction as shown in Fig. 4.1e, f. According to eq. (2.9) the splitting $\Delta_B = E_{\sigma^+} - E_{\sigma^-}$ – with peak energies $E_{\sigma^{+/-}}$ recorded under $\sigma^{+/-}$ polarized detection – at any magnetic field can be used to directly obtain the g-factor. Nevertheless,

Table 4.1 Experimental exciton g-factors in charge-controlled monolayer and bilayer WSe_2. Experimental exciton g-factors obtained from magneto-luminescence of neutral and negatively charged monolayer and bilayer WSe_2. DR spectroscopy shows the values: $X^0 : -4.3 \pm 0.1$; $X_1^- : -4.7 \pm 0.3$; $X_2^- : -6.5 \pm 0.4$

ML				BL		
X^0	M_1^0	M_2^0	M_3^0	B_1^0	B_2^0	B_3^0
-4.1	-11.5	-12.6	-11.4	-11.4	-10.8	-12.8
$\pm$0.1	$\pm$0.1	$\pm$0.2	$\pm$0.4	$\pm$0.2	$\pm$0.1	$\pm$0.2
X_1^-	X_2^-	D^-	M_1^-	B_1^-	B_2^-	B_3^-
-4.6	-1.3	-12.2	-9.0	-9.1	-9.8	-11.5
$\pm$0.3	$\pm$0.3	$\pm$0.1	$\pm$0.1	$\pm$0.3	$\pm$1.0	$\pm$0.4

it is useful to measure Δ_B over a wide range of magnetic fields to get a statistically more accurate estimate, while verifying the linear nature of the splitting. This estimate can either be obtained by averaging the g-factor values calculated at every point or perform a linear regression on Δ_B vs B. The slope of the resulting line corresponds to the g-factor.

The splitting Δ_B was measured for all discussed peaks in the PL spectrum between –8 T and +8 T with half-tesla steps. For high oscillator strength transitions of X^0 and $X^{+/-}$ the measurements was also performed using DR spectroscopy. Results for Δ_B are shown in Fig. 4.2 with the corresponding g-factors in table 4.1. In the monolayer, the g-factor for bright and spin-dark excitons and their charged counterparts X^0, D^0, X_1^-, X_2^-, and D^- have been measured repeatedly in various previous studies [21, 55, 86, 87, 132–140]. The results for the bright exciton X^0 agree with these established values as well as values for the trion doublet, when referring to the lower-energy peak X_2^-. The lower PL signal of X_1^- and the broad linewidth of 6 meV in the sample do not align with the expected value and can be discarded in the light of previous, more accurate, measurements. Similarly, the g-factor of the neutral spin-dark exciton D^0 could not be properly determined but was previously measured to have a g-factor of between 9.1 and 9.9 [55, 132, 134, 135]. Inhomogeneous broadening of the strong feature M_1^0 overwhelms the signal in a way that renders tracking the exact peak position and splitting impossible. The chiral phonon replicum of this peak, previously reported at 65 meV below X^0 with the same g-factor is similarly obscured by the strong feature M_2^0, showing a g-factor of 12.9$\pm$0.7 at 60 meV red-shift. This peak is consistent with

previous data as well [134, 135]. The last peak on the red end of the spectrum M_3^0 shows a g-factor indistinguishable from that of M_1^0, which suggest that both peaks draw from the same reservoir in the exciton band structure. For the negative dark trion D^-, a g-factor of –12.2 $\pm$0.1 is measured, which is in conflict with previous data, suggesting an equal g-factor to D [132–135]. However, the peak to the red M_1^- shows a g-factor of –9.0 $\pm$0.1, which is in agreement with the identification as a phonon-sideband of D^- [134, 135]. The latter sources also measure an additional peak, located between M_1^- and D^-, that shows strong luminescence as well as a g-factor of –4.1 [134] and –3.4 [135]. However, in our sample, this peak is consistently absent in the negative doping regime.

An additional mystery shrouds the unambiguous identification of the peak M_1^0. It has been attributed to several origins, including phonon-assisted PL from virtual trions [141], phonon-sidebands of momentum-dark excitons originating in the Q-valley [38], or zero-phonon PL of finite-momentum excitons in spin-like configration [135], in our convention named K_L'.

The results from DFT calculations (see Chapter 2) create a comprehensive model to explain g-factors in the spectrum of WSe_2 mono- and bilayers. The best-studied exciton in monolayer TMDs is X^0, which the DFT-model predicts to have a g-factor of –4.0. This value is in excellent agreement with both our own measurement of –4.1 as well as previous studies [86, 87, 136–139]. As previously discussed, the spin-dark exciton as well as its g-factor could not be properly resolved in this experiment. However, the model – which shows a value of 10.1 – can compared to other measurements showing a value of $\simeq$ 9.4 [55], again reaching good agreement. Both excitons have momentum-indirect counterparts labelled K_L' and K_U' with the electron of the same spin-configration residing in K'. For those, the DFT calculations show large g-factors of 13.6 and 19.6 respectively. The g-factors of excitons involving the Q-valley range between 9.2 and 14.5 This range is similar to the g-factors of D^0 and K_L', which means that unfortunately these species are not clearly distinguishable by their magnetic splitting. Contrasting to that are excitons with a hole in Γ, that – except for the spin-unlike configration with an electron in K' with a g-factor of 9.8 – show relatively small g-factors of <5.8 and are clearly distinct from other exciton species.

In the bilayer case, intralayer excitons show similar values in DFT compared to the monolayer, which is to be expected [142]. Unlike the monolayer however, the bilayer can also form interlayer excitons (e.g. intralayer Q_L with its interlayer counterpart Q_L', intralayer Q_U and interlayer Q_U' and so on). In the DFT model, based on the input from the band structure alone and ignoring Coulomb corrections arising from the

intra-/interlayer nature of the excitons, their g-factors are the same.

While the theoretical predictions for momentum-direct excitons both explain the observed g-factors in our sample and previous measurements, the model can also be utilized to explain the g-factors of previously ambiguous features and thus help with their identification and understanding. In the monolayer, the main unknown is the bright feature M_1^0, and by extension M_3^0. Unfortunately however, the energetic location and g-factor sill leaves ambiguity within our model. Its g-factor of –11.5 is compatible predictions for Q_L and Q'_U in table 2.1 – Both other Q-indirect excitons Q_U and Q'_L can be excluded as their energy lies 250 meV above Q_L and Q'_U [58]. However, as previously noted, another explanation for this feature is zero-phonon emission of spin-like K-indirect excitons [135], which in the notation here corresponds to K'_L. With a g-factor of 13.6 from the DFT model, this is close enough to the observed value. While the previously mentioned low-g-factor peak between M_1^- and D^- is not observed in our sample, the DFT calculations still provide $K\Gamma$ and $Q\Gamma$ as possible candidates for the feature as their small g-factors lie close to what is observed in negatively charged high-quality samples with narrow spectra [134, 135].

In the neutral bilayer, our results suggest ruling out $Q\Gamma$ excitons and instead suggest spin-unlike interlayer QK, as well as intralayer $Q'K$ excitons instead of $K'\Gamma$ as the origin of the peaks B_1^0, B_2^0 and B_3^0. This does not conclude the understanding of the origin of the neutral regime. We can however suggest that, similar to the monolayer, the additional charges in the negative regime do not a alter the g-factor which instead can be attributed to neutral finite-momentum reservoirs.

4.2 Spectroscopy of tungsten disulfide monolayers

WS_2 is one of several tungsten-based TMDs and structurally similar to WSe_2. Therefore it also shows a very similar band structure but at a higher band gap [143], leading to a blue shift of the exciton spectrum with regards to WSe_2. Recently, van der Waals heterostructures made of WS_2 and $MoSe_2$, as well as WS_2 and WSe_2 have attracted high attention due to emerging many-body effects in relation to moiré superlattices [144, 145]. However, compared to WSe_2, the spectrum of WS_2 monolayers has been considerably less studied, especially in charge-controlled devices. In the following section, the spectrum of a WS_2 monolayer embedded in a graphene-based gate structure, allowing both hole and electron doping is shown. Subsequently, similarities and differences to WSe_2 are discussed.

The sample for this experiment was a heterostructure of a monolayer of WS_2 and

$MoSe_2$, respectively, that was encapsulated between two sheets of hBN (see Fig. 4.3a). This chapter focusses on spectroscopy of WS_2 only with experiments performed on $MoSe_2$ and the WS_2 /$MoSe_2$ heterostructure are discussed elsewhere [108, 144, 145]. Electrical contacts and gates were realized using sheets of few layer graphene (see Chapter 3.1) and included both a top gate, bottom gate and an electrical contact to connect to the heterostructure itself. All few layer graphene flakes connected to lithographically defined gold contacts. The top/bottom gate configuration initially allowed independent tuning of electrostatic doping as well as the application of an external electric field. However, the breakdown of one dielectric hBN layer during the course of the experiments resulted in voltages applied to the top gate to charge the heterostructure instead, reducing the tunability for the sample to doping only.

The experiment was performed in a liquid helium cryostat at 4.2 K using a confocal microscope with a long working distance low temperature objective (see Section 3.2). In PL experiments, the sample was excited using a diode laser at a wavelength of 533 nm and laser powers below 100 μW and up to 1 mW for power series. For DR, a pulsed supercontinuum laser (NKT Super K Extreme, Varia) or an incandescent halogen lamp (OceanOptics) were used. Voltages of up to ±10 V were supplied using a general purpose input/output device (National Instruments USB-6363). Using a push-pull configration, differential voltages up to ± 14 V were applied to the heterostructure, limited by the dielectric strength of the bottom hBN layer. The indicated gate voltage V_g was thus the effective voltage being applied to the bottom gate with respect to the heterostructure (see above).

First, the sample was characterized using gate-dependent DR spectroscopy (see Fig. 4.3b) with V_g between − 5 V and 5 V. In DR, the spectrum is defined solely by momentum-direct transitions with high oscillator strength. At zero gate-voltage, the spectrum consisted of the strong neutral exciton resonance X^0 at 2.06 eV and the weaker charged exciton doublet $X^-_{s/t}$ between 2.02 eV and 2.03 eV that expectedly showed a 7 meV exchange splitting [146]. At negative V_g, X^0 increased in strength, while $X^-_{s/t}$ gradually vanished. At roughly $V_g \sim -2.5$ V, X^0 plateaus while $X^-_{s/t}$ is completely absent, indicating neutrality. The opposite was true for positive values of V_g, where $X^-_{s/t}$ gained and X^0 gradually lost in strength, while also shifting to higher energies. This indicates an increase in negative charge carrier density.

Next, the sample was further characterized by PL spectroscopy (see Fig. 4.3d,e), which revealed a more complicated spectrum with multiple additional features appearing below the energy of X^0. The transition between the neutral and negative regime was determined from the previous DR measurement that agreed with the on-

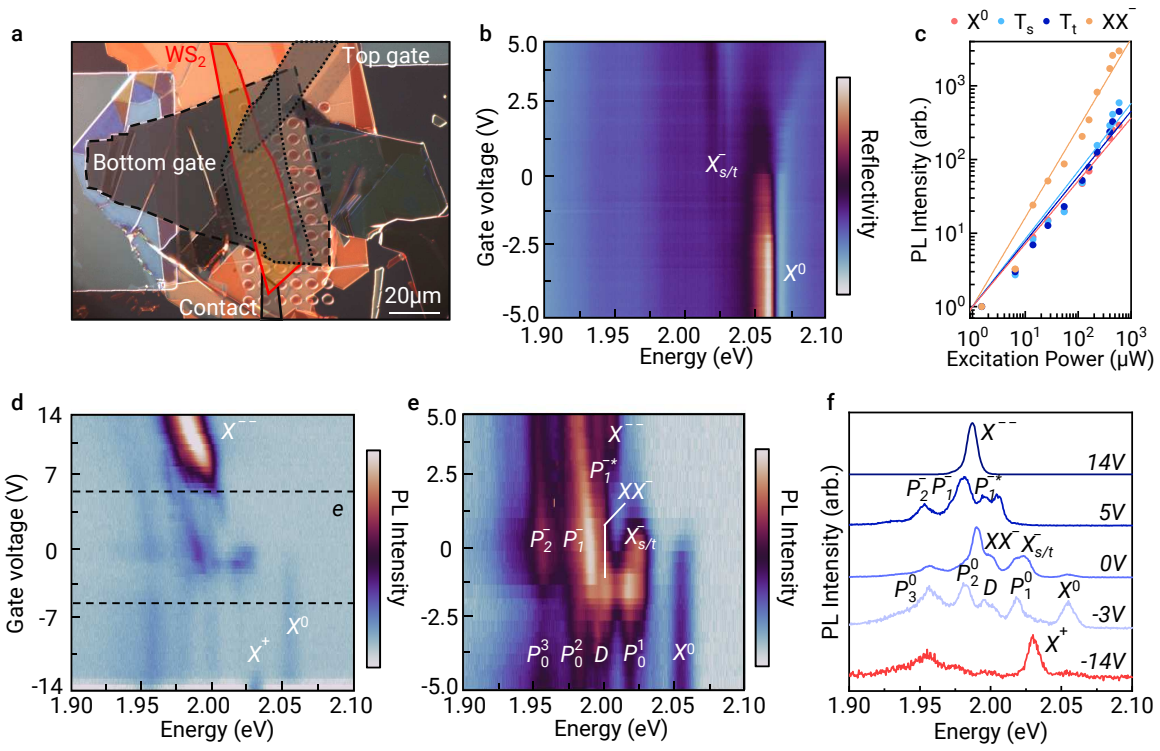

Figure 4.3 Spectroscopy of charge-controlled ML-WS_2. **a,** Differential interference contrast image of WS_2/$MoSe_2$ heterostructure with WS_2 (Graphite) highlighted in red (black). **b,** Differential reflectivity spectrum of ML-WS_2 at different gate voltages. **c,** Photoluminescence intensity of spectral lines of ML-WS_2 at different excitation powers. **d,** Photoluminescence spectrum of ML-WS_2 at different gate voltages. **e,** Detailed photoluminescence spectrum of ML-WS_2 at small gate voltages. **f,** Normalized characteristic photoluminescence spectra of ML-WS_2 in different doping regimes.

set of X^0 and $X^-_{s/t}$ in PL. However, as the range of the gate voltage in the PL measurements reached up to $\pm$ 14 V, 9 V higher in both positive and negative direction, this measurement revealed several distinct charging regimes, invisible in our DR measurement.

First, the extend of the neutral regime that spans the band gap of ML-WS_2 was determined from the intensity of X^0 and corresponded to values of V_g between -4 V and $-$ 13 V. Energetically below X^0, several spectral lines were observed, denoted P^0_1, D, P^0_2 and P^0_3 in decreasing energetic order. P^0_1 at 2.02 eV overlapped energetically with $X^-_{s/t}$ but was still visible in the neutral regime, indicating uncharged excitons as its origin. This feature is well known and also present in WSe_2 [38, 85, 135]. It has for example been linked to phonon sidebands of momentum-indirect excitons in the Q-valley [38]. Other explanations for this spectral line in WSe_2 have been proposed

and can be applied to WS_2 as well (see Chapter 4). Below P_1^0 the spin-forbidden dark exciton D was observed at 2.005 eV with a known bright-dark splitting $\Delta_{X,D} = 55$ meV [38, 131]. As the selection rules allow only in-plane emission [131], the signal picked up by the high NA objective was only margially distinguishable from the background. The features P_2^0 and P_3^0 at 1.98 eV and 1.955 eV, were attributed either to localized emitters [131] or, analogously to WSe_2, to phonon sidebands of momentum-indirect excitons [38, 85, 135].

At gate voltages of V_g above -4V, the spectrum changed, indicating the formation of charged excitons. However, unlike in DR, the charging behavior was more complex and showed different stages. At low negative doping close to the charging threshold, the doublet feature of $X_{s/t}^-$ first appeared as before, accompanied by additional features XX^- and P_1^-. The peak XX^- at 2.005 eV was attributed to the charged biexciton with a splitting of $\Delta_{X,XX^-} = 55$ meV which is close to what is observed in WSe_2 [125, 147, 148]. The absence of the neutral biexciton XX^0 at lower values of V_g was consistent with previous observations as well [125], which show a much lower PL intensity compared to both XX^- and X^0. The feature P_1^- at 1.99 eV showed both high PL intensity as well as a strong redshifting behavior at higher gate voltages. At slightly higher values of V_g, the intensity within the charged exciton $X_{s/t}^-$ shifted from the lower energy singlet trion (X_s^-) towards the high energy triplet (X_t^-) [146]. At the same time, X^0 was lowering in brightness, analogous to the lowering oscillator strength in DR. An additional peak P_2^- appeared at 1.95 eV with a similar redshifting behavior as P_1^-, indicating a potentially similar origin. At even higher values of V_g, X^0 and subsequently $X_{s/t}^-$ disappeared while P_1^- stratified into two distinct peaks P_1^- and P_1^{-*}. This splitting was also consistent with two distinct peaks being present at lower charge carrier densities whose energy shifts have different sensitivities to additional doping. As additional charging is applied an additional strongly redshifting feature X^{--} to the red side of $X_{s/t}^-$ gained in intensity and gradually merged into P_1^{-*} to form a single peak with very high PL intensity. A similar feature has been observed in WSe_2 [47, 125, 132, 133] and is associated with the fine structure of the trion [47] At the onset of X^{--}, P_1^- and P_2^- gradually lost intensity and vanished at even higher charge concentrations. Finally, at higher negative values of V_g below $-$ 13 V, X^0 and other neutral features vanished, indicating the onset of a positive doping regime. This was accompanied by the appearance of the positively charged exciton X^+, that was slightly blueshifted with respect to X^-, which is consistent with measurements in WSe_2 [135].

5 Tip-assisted spectroscopy of WSe_2 monolayers

The following chapter describes experimental results on tip-assisted spectroscopy of suspended monolayer WSe_2 using a transparent diamond tip mounted to a quartz tuning fork (QTF). The first section describes the characterization of the sample with conventional confocal spectroscopy. Next, tip-assisted hyperspectral imaging of the sample is discussed and compared to the previous measurement. Finally, the effects of local force application are presented.

5.1 Sample characterization

The experiments described in this chapter were performed on one sample of ML-WSe_2, encapsulated between two sheets of hBN with a thickness of 82 nm at the bottom and 13 nm at the top, which was fabricated from exfoliated single crystalline flakes through temperature-controlled viscoelastic stamping (see chapter 3.1). A schematic drawing of the sample is shown in Fig. 5.1a and a differential interference contrast (DIC) image in Fig. 5.1c. As the goal of this experiment was the application of localized tensile strain, the device had to preserve the elasticity of the WSe_2. This was achieved by suspending the sample in a microdrum configuration such that the diamond tip was able to press from the top to deform the ML-WSe_2. To suspend the sample, air-holes of approximately 4 μm in diameter were etched through the bottom hBN flake using laser lithography and ICP-RIE with SF_6. The patterned flake was then picked up by the hBN/WSe_2 sub-assembly on the stamp and transferred to a new substrate. The sample was then transferred to the experimental setup as described in Chapter 3.2. In brief, the sample was mounted on a piezo positioner inside a liquid helium cryostat close to the focus of a low-temperature apochromatic objective with a working distance of 5 mm. A second set of positioners was used to mount QTF and diamond tip (see Fig. 5.1b,d and Section 3.3). For measurements, the tip was moved into the beam path with the top facet positioned in the focus of the microscope.

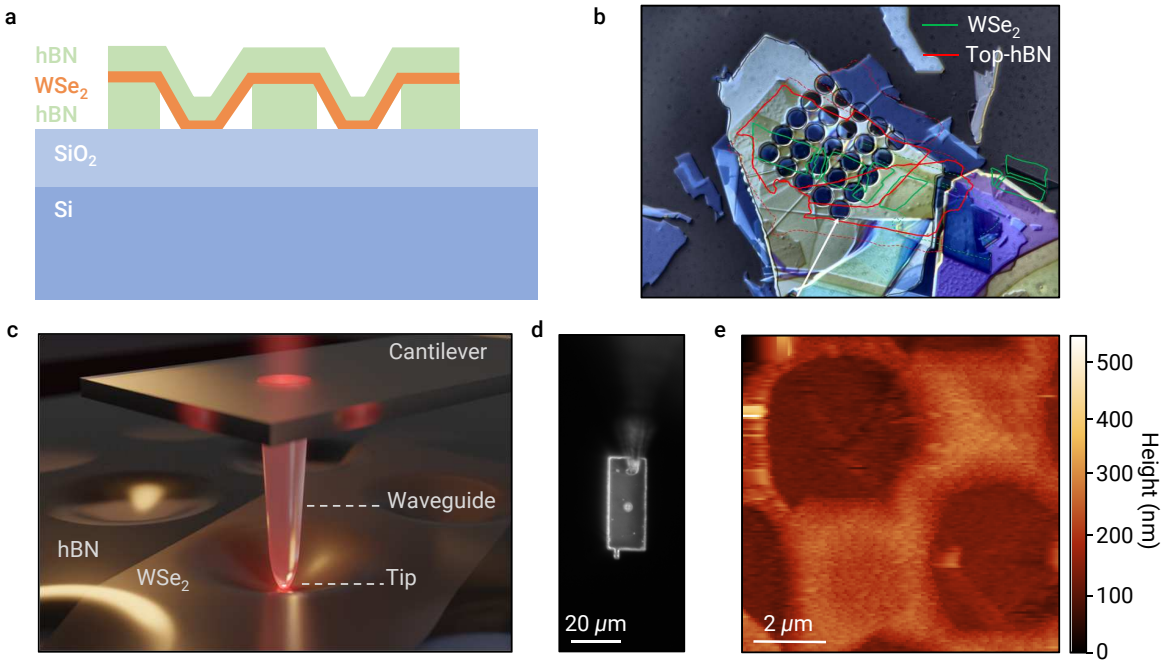

Figure 5.1 Sample layout and QTF AFM characterization. a, Schematic of a WSe_2 monolayer sample suspended over a patterned hBN flake with 4 µm air-holes. The holes extend through the entire bottom layer with a thickness of 82 nm. The WSe_2 layer is capped by another 13 nm thin flake of hBN. **b,** Differential interference contrast image of the sample corresponding to **a**. **c,** Rendering of an illuminated diamond cantilever in contact with a suspended WSe_2 sample. **d,** Top side dark field microscope image of the diamond cantilever. **e,** AM-AFM image of the sample, measured with the diamond tip mounted to a piezo-electric quartz tuning fork.

The sample was first characterized using AFM (see Fig. 5.1e), which showed a height difference between the edges and the center of the air-holes of approximately 100 nm, with a gradual height gradient at the edges and a sharp transition to a flat profile towards the center. This height differential exceeded the depth of the etched air hole of 82 nm, indicating wrinkling at the edges. The plateau in the center further showed that the WSe_2 layer was not fully suspended and instead touched the SiO_2 substrate. Next, the sample was characterized optically in a confocal configuration. Using DR spectroscopy, the A-exciton resonance X^0 (see also Chapter 4) was recorded over the area of the sample which confirmed charge neutrality through the absence of a trion doublet. Due to the patterning of the sample, parts of the ML-WSe_2 were encapsulated between two layers of hBN, partly suspended with hBN on top or sandwiched between hBN on top and SiO_2 on the bottom. The effect of these structural differences on the optical response was characterized using PL spectroscopy. In this configura-

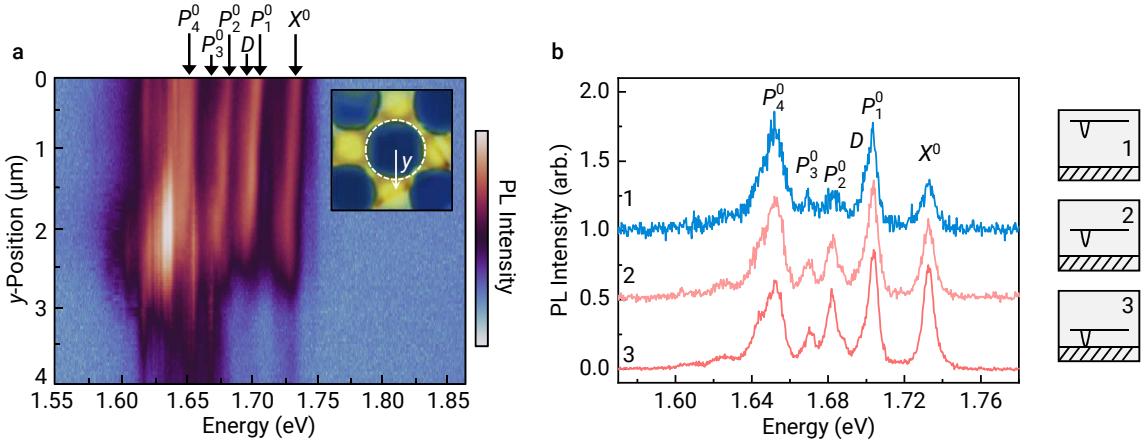

Figure 5.2 Spatial variation of the PL spectrum of partially suspended WSe_2. **a,** Confocal PL line scan of the ML-WSe_2 spectrum over the cross section of an air-hole in the bottom hBN layer. Inset shows a bright-field microscope image of the sample, superimposed with the line of measurement and outline of the air-hole. Depressions are shaded in dark blue, elevations in yellow. **b,** PL spectrum of ML-WSe_2 in the center of an air-hole, recorded through the diamond tip, for three distances between the sample and the tip facet.

tion, the sample was excited using a home-built diode laser at 660 nm, close to the 2s-resonance of WSe_2 [149], or a commercial diode laser with a wavelength of 633 nm (Thorlabs HHL). Excitation laser power was chosen below the threshold, resulting in biexciton luminescence, in this case below 20 µW. A line scan of the spectra along one air-hole is shown in Fig. 5.2a. In the center (at a y-position close to zero) the spectrum consisted of multiple peaks. The bright exciton X^0 at 1.731 eV was significantly blue-shifted compared to typical experiments performed on samples with complete hBN encapsulation, which was consistent with measurements published elsewhere on a hBN/WSe_2/SiO_2 heterostructure [150]. The energetic position of the features P_1^0, P_3^0 and P_4^0 was consistent with the peaks M_1^0 to M_3^0 in Chapter 4, where their assignment is discussed in more detail. The dark exciton D^0, as before, was only detected as a shoulder of P_1^0, as the spectral broadening merged these features. The peak P_2^0 between D^0 and P_3^0 is explained by chiral phonon replicas of D^0 [134]. With increased distance from the center of the air-hole, the spectrum experienced a collective redshift, consistent with the changing dielectric environment from SiO_2 to hBN. Also, closer to the edge of the hole, new, narrow spectral lines appeared that didn't exhibit a redshift. These features were attributed to local disorder, originating from a local region which appeared brighter when being sampled closer to the center of the focal spot. The emergence of this disorder was consistent with the edge of the hBN air

hole, putting the ML-WSe_2 under strain to create local band structure distortions that allowed recombination of otherwise dark exciton populations [60]. Beyond the edge where the WSe_2 was fully encapsulated, PL intensity was significantly reduced with respect to other parts of the sample. This fact likely originated from the fabrication process, specifically surface contamination of the bottom hBN layer [130].

5.2 Tip-assisted microscopy

Following conventional confocal spectroscopy, the sample was studied using PL spectroscopy assisted by the diamond tip which was moved into the focus of the objective (see Fig.5.1b,d). The tip was attached to a rectangular diamond cantilever. Although the tip itself was only 1 μm in diameter, it was easily detectable by monitoring the reflected image from the cantilever using the spy camera of the microscope. When the tip was in focus, the scattered light illuminated the cantilever, causing the rectangular outlines to brighten, similar to the dark-field image shown in Fig.5.1d. Additional fine-tuning of the focal position was possible by monitoring the reflectance spectrum of tip and cantilever. As the top and bottom surface of the diamond form a low finesse Fabry-Perot resonator, the reflection spectrum experiences interference fringes with the free spectral range depending on the thickness of the material. The tip, which had a total length of 8 μm, was considerably thicker than the cantilever with a thickness of 2 μm. Therefore, the periodicity of the interference fringes when focussing the tip was much higher compared to the cantilever. Next, the sample was positioned in close proximity to the tip (see Section 3.3). The first step in the experiment was to understand how the distance between sample and tip affects the spectrum of the transmitted light (see Fig. 5.2b). This measurement was performed at the homogeneous center of an air hole to eliminate lateral displacement affecting the result. At a closing distance between sample and tip and the total PL intensity increased, while the relative intensity of the different spectral lines shifted. As a result, both X^0 and P_2^0 were gaining higher levels of PL intensity with respect to the rest of the spectrum. This was explained by the transmission behavior of the tip that changed once the sample was close enough to evanescently couple PL to the tip. Another explanation was that the near field coupling enhanced spectral lines that would otherwise be suppressed in the far-field such as the z-polarized dark exciton D^0 [55, 130, 131] whose selection rules only allow lateral emission but has been shown to couple to the near field [60]. However, the intensity of D^0 in the shoulder of P_1^0 remained unchanged.

In the next part of the experiment, hyperspectral PL imaging of the sample was per-

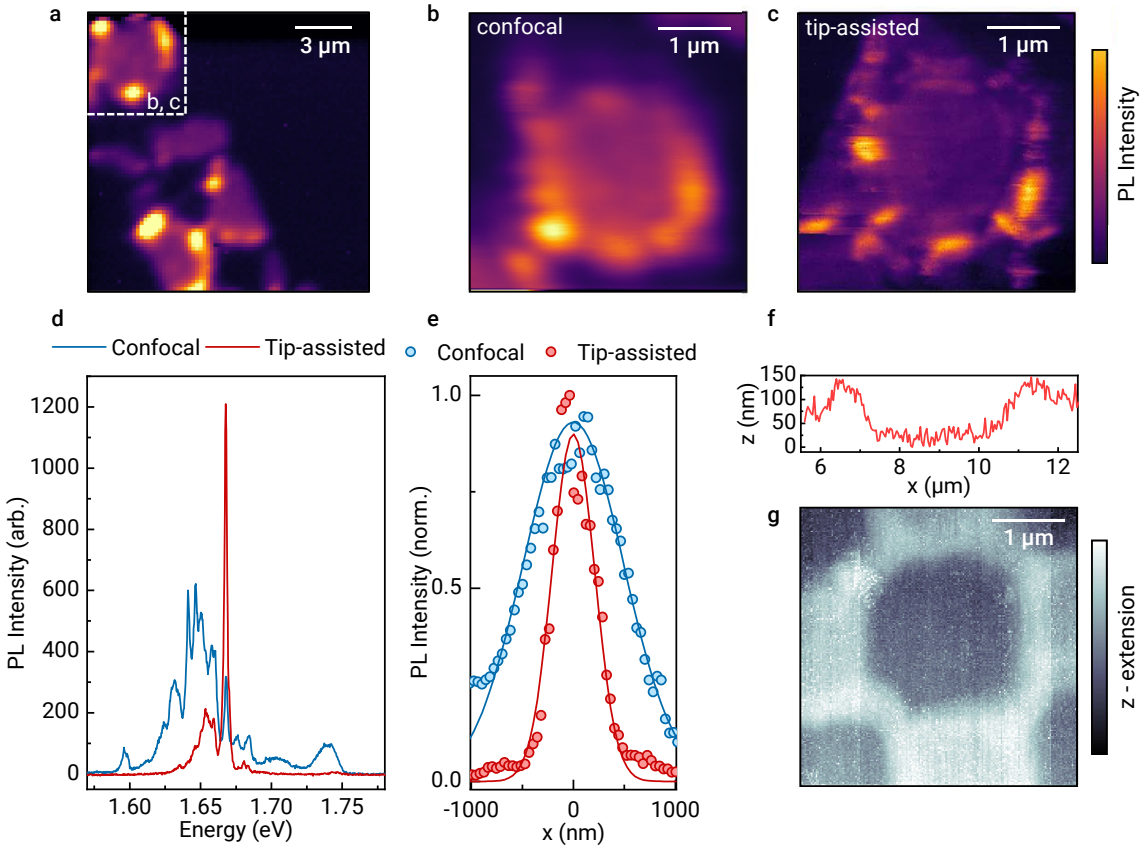

Figure 5.3 Tip-assisted PL spectroscopy of monolayer WSe_2. **a,** Raster-scan image of the confocally measured PL intensity of a suspended monolayer WSe_2 sample. **b, c** Raster-scan image of the PL intensity measured confocally (b) and through a parabolic diamond tip (c). **d,** Selected PL spectrum measured at the same sample location confocally (blue) and tip-assisted (red). **e,** PL intensity of a single emitter (sharp line at 1.67 eV in **d**) along one spatial axis measured confocally (blue) and through the tip (red). The confocal and tip-assisted profiles show a FWHM of 1160 nm and 439 nm, respectively.

formed in a confocal configuration and subsequently by sampling the tip transmission (see Fig. 5.3). First, the area of interest on the sample was imaged confocally as a reference at the full range of the scanning piezos of 15 μm × 15 μm at a large step size (see Fig. 5.3a). Subsequently, a smaller section of this area with a size of 7 μm × 7 μm was scanned at a low stepsize of 40 nm confocally and tip-assisted, with the distance between sample an tip controlled using FM-feedback. The resulting images of total PL intensity in confocal and tip-assisted configuration are shown in Fig. 5.3b,c, respectively. Strikingly, the tip-assisted image showed significantly more detail compared to the confocal configuration. This relative improvement was quantified by analyzing a single point emitter, characterized by a narrow line in the ML-WSe_2 spectrum. The lateral distribution of its respective PL intensity was then used to estimate the point-spread-function (PSF) of both imaging configurations. Multiple suitable features were located on the edges of the air-hole and were compared by plotting the total intensity at each sampled point across one lateral axis (see Fig. 5.3d,e). While the ideal intensity distribution of a point-like light source is described by the Airy disk, a Gaussian distribution approximated the main mode of the distribution well enough to estimate the full-width at half-maximum (FWHM) which was used as a figure of merit for the lateral resolution. As shown in 5.3b, the confocally imaged point-emitter yielded a FWHM of 1160 nm, in line with expectations for the used diffraction-limited objective. Imaged through the diamond tip, the profile narrowed to 439 nm for the same emitter, showing an approximately 2.5-fold improvement in lateral resolution.

5.3 Strain-dependent spectroscopy

In the next step, the diamond tip was used to measure the spectral response of suspended ML-WSe_2 under local strain. This was achieved by decreasing the tip-sample distance to the point where the elastic sample was deformed by the resulting force. As shown before, elastic areas of the sample were located around the edges of the air holes and identified by their PL spectrum, specifically by the energetic position of X^0 at approximately 1.72 eV and the absence of bright, disorder-induced features in the low-energy range of the spectrum. Local force was applied in an open-loop or closed-loop configuration. In open-loop mode, strain was applied by moving the sample closer to the tip while recording the spectrum depending on the applied piezo voltage. This method does not rely on complex electronic control and was limited in its dynamic range only by the maximum extension of the piezo, as well as the destruction threshold of the glass-capillary, that connected the diamond tip to the QTF.

In contrast, when operating in closed-loop mode, the interaction between sample and tip was tuned by stabilizing the QTF amplitude with respect to a setpoint. In this case, the amplitude corresponded to the force acting on the QTF. This was advantageous because the applied force was tunable reproducibly and small perturbations of tip-sample distance were corrected by the control loop in real time. However, this approach was limited by the relationship between the applied force and the vibrational amplitude of the QTF, specifically by the fact that the highest possible force in closed-loop mode corresponded to the lowest detectable amplitude of the tuning fork. In our system, this limit was reached at the noise floor of approximately 2 mV which corresponded to approximately 1 % of a typical measured free amplitude of 300-400 mV. While this ratio was improvable by increasing the excitation amplitude of the QTF, this method was ultimately limited in its potential force output by the steep amplitude of the QTF in close proximity to the sample (see Fig. 3.6 in Section 3.3). An additional issue was that the relationship between force and amplitude varied between different QTF. With a tip mounted on one prong of the tuning fork, its mechanical resonance split into two modes, which resulted in the motion of the tip either in-plane or out-of-plane, respectively. The relative frequency shift of both modes as well as its sign varied between different QTF and was indistinguishable a priori. While all QTFs performed well for AFM operation, some QTF experienced a much steeper drop in amplitude on approach and were thus too sensitive to apply significant force in a closed-loop configuration. As a result, measurements requiring large force were performed in an open-loop configuration.

5.3.1 Closed-loop strain control

In the first experiment, strain-dependent PL spectroscopy was performed in a closed-loop configuration (see Fig. 5.4). Operating in AM mode, the amplitude setpoint was gradually lowered such that the force between tip and sample increased. The excitation of the QTF was set to a free amplitude of 400 mV, corresponding to an initial approach setpoint of 300 mV. The excitation wavelength was 635 nm. At maximum amplitude (see Fig. 5.4a,c), the observed energetic position of X^0 was unusually high at approximately 1.748 eV. This discrepancy was explained by inaccurate calibration of the spectrometer caused by a software error. Therefore, only relative energy positions were considered in the interpretation within this section and the problem was absent in later stages of the experiment. Upon lowering the amplitude setpoint, the spectrum of the sample gradually shifted to lower energies, indicating an increase in tensile strain (see also Chapter 2). The level of strain was monitored through the

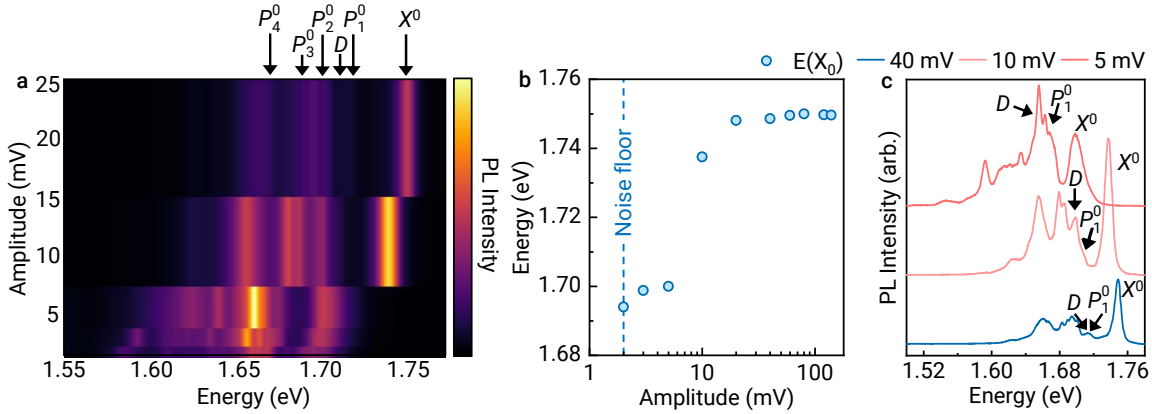

Figure 5.4 Closed-loop control of elastic strain. a, Photoluminescence spectrum of monolayer WSe_2 at increasing strain. Lower QTF amplitudes indicate less separation between sample an tip and thus a larger force. **b,** Spectral position of the bright exciton X^0 depending on QTF amplitude. The dashed line indicates the noise floor, where further increase in force does not create additional electronic feedback. **c,** Selected spectra of monolayer WSe_2 at different TF amplitudes.

energy shift of the peak position of X^0 (see Fig. 5.4). Initially, a lower amplitude setpoint lead to an increase of PL intensity for X^0, indicating a higher coupling between tip and sample. At amplitudes below 20 mV, the PL intensity of X^0 increased sharply, accompanied by a redshift. At the maximum closed-loop strain at the noise-limited amplitude of 2 mV, this redshift amounted to 53 meV. The relative energetic positions of the lower energy spectrum, as identified previously, are shown in Fig. 5.4a. As before, D_0 was not distinguishable from the peak P_1^0 at low strain. On contact however, concurrent to the redshift of X^0, the relative intensity within the rest of the spectrum realigned as well. Notably, the intensity of D^0 substantially increased with respect to P_1^0 which was explained through near field coupling of the tip, allowing the laterally emitting light from the z-polarized D_0 to radiate directly into the tip [60]. At higher strain, the intensity of D^0 increased even further. This coincided with the initial energetic position of the peak P_4^0. Unfortunately, an operational error subsequent to this measurement caused the tip to be pressed into the substrate, resulting in the loss of the tip as well as damage to this region of the sample.

5.3.2 Open-loop strain control

The experiment was continued with a new QTF at other regions of the sample. This particular QTF proved to be more sensitive to forces on contact and was therefore

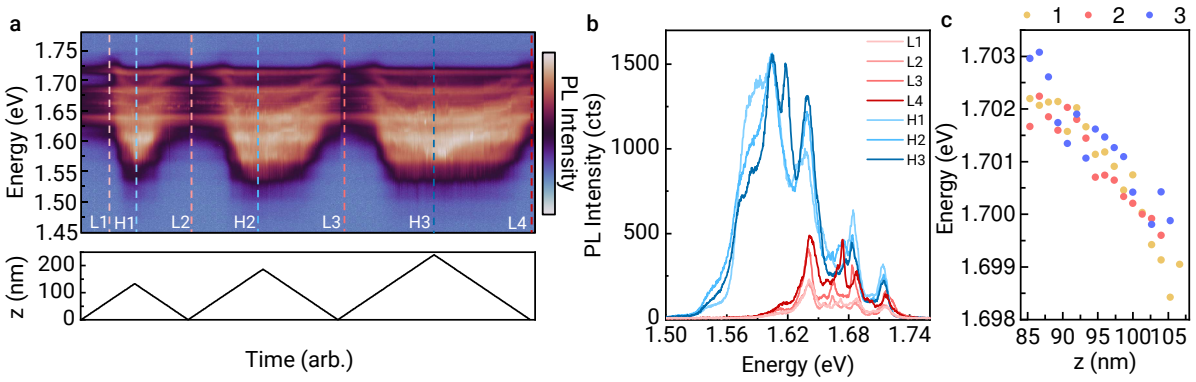

Figure 5.5 PL spectrum of elastically strained WSe_2. **a,** PL spectrum of monolayer WSe_2 at different levels of localized strain. The bottom panel shows the extension of the vertical piezo, with high extension corresponding to high strain. The point of highest applied force was increased between all of the three consecutive extension profiles. Between every strain-release cycle, the tip was fully retracted. **b,** PL spectra of monolayer WSe_2 extracted from **a** at low and high strain. Low (High) spectra are indicated by an L (H) and colored in shades of red (blue), with the number indicating the ordering in time within the strain profile. **c,** Peak position of X^0 extracted from **a**. The position of the lower lying branch of the split X^0 spectrum is recorded at strain values where the peak can be clearly discriminated clearly from the background.

operated in open-loop configuration. As before, the sample was approached by decreasing the distance gradually while monitoring the vibrational amplitude. Once the sample was in range of the scanning piezo, the distance was controlled through the piezo voltage only, without using feedback from the QTF. The tip was then positioned over another region of suspended WSe_2. First, the strain response was examined by applying small force inputs that were iteratively increased to higher values (see Fig. 5.5). This was achieved by cycling the extension of the scanning piezo to successively higher voltages while recording the PL spectrum. Unlike in the previous experiment, no global redshift of the entire spectrum was observed but rather a splitting of the recorded spectrum in two separate branches. The lower energy branch exhibited a low response to strain, while the higher energy branch experienced a substantial redshift.

At higher strain, the lower-energy part of the spectrum experienced a significant increase in intensity consistent with the sample behavior in the previous experiment. At even higher force, the redshift of the spectrum saturated and stayed flat for higher extensions of the piezo. This saturation happened at approximately 100 nm of piezo

extension beyond the point of contact (bottom panel of Fig. 5.5a) and is thus attributed to the suspended WSe_2 touching the bottom of the hBN air hole. The close correspondence between piezo extension and depth of the hole also indicates that the stiffness of the sample was much lower than that of the QTF.

Fig. 5.5b,c show spectra and the position of X^0 against z-extension. Throughout all three cycles, the strain behavior of the spectrum stayed largely identical (see Fig. 5.5b,c), demonstrating that the sample remained mostly elastic and any strain was reversible. Specifically, the position of X^0, as measured by tracking the lower, red-shifting branch in the initial parts of the force curve is identical in all three approaches.

5.3.3 Discussion

The main effect of local force application in the presented experiments was a strain-related redshift as well as a significant increase in PL intensity. As the interaction between tip and suspended sample resulted in tensile strain, the redshift was expected [60, 73, 74, 82]. In the later part of the experiment, the strain response showed a splitting of the spectrum into a more (less) sensitive lower (higher) energy branch. This behavior was not present in the first experiment and was therefore likely related to the measurement technique itself. The most likely explanation was that the spectrum in the second case was sampled from regions of differential strain across the tip cross section. The geometry of the tip incorporates a sharp edge where the flat tip facet transitions into the more rounded, parabolic profile. Theoretical predictions have shown, that this geometry leads to significantly increased strain at these edges [60] compared to the flat facet. It is possible that depending on the positioning of the tip in the focus of the objective, the sampled spectrum incorporates more or less contributions from edge or facet. Another possibility is, that the positioning of the tip with regards to the edge of the air hole has a similar effect.

The reason for the increase in PL intensity is explained with the hybridization of dark defect-related states with the spin-dark exciton D^0 [82]. Point defects in the form of selenium vacancies introduce two lower-energy states slightly below the conduction band edge [82, 151, 152]. The corresponding exciton states are formed between an electron localized in the selenium vacancy, pairing with a valance band hole [82]. Although their radiative recombination is allowed from a symmetry perspective, their low density results in a low PL signal [82]. Under strain, valence band and defect states show significantly less sensitivity than the conduction band [58, 73, 151]. As a result, D^0 as well as its intervalley counterpart, the spin-like, momentum-indirect KK'-exciton, experience a stronger redshift than the defect-related excitons and be-

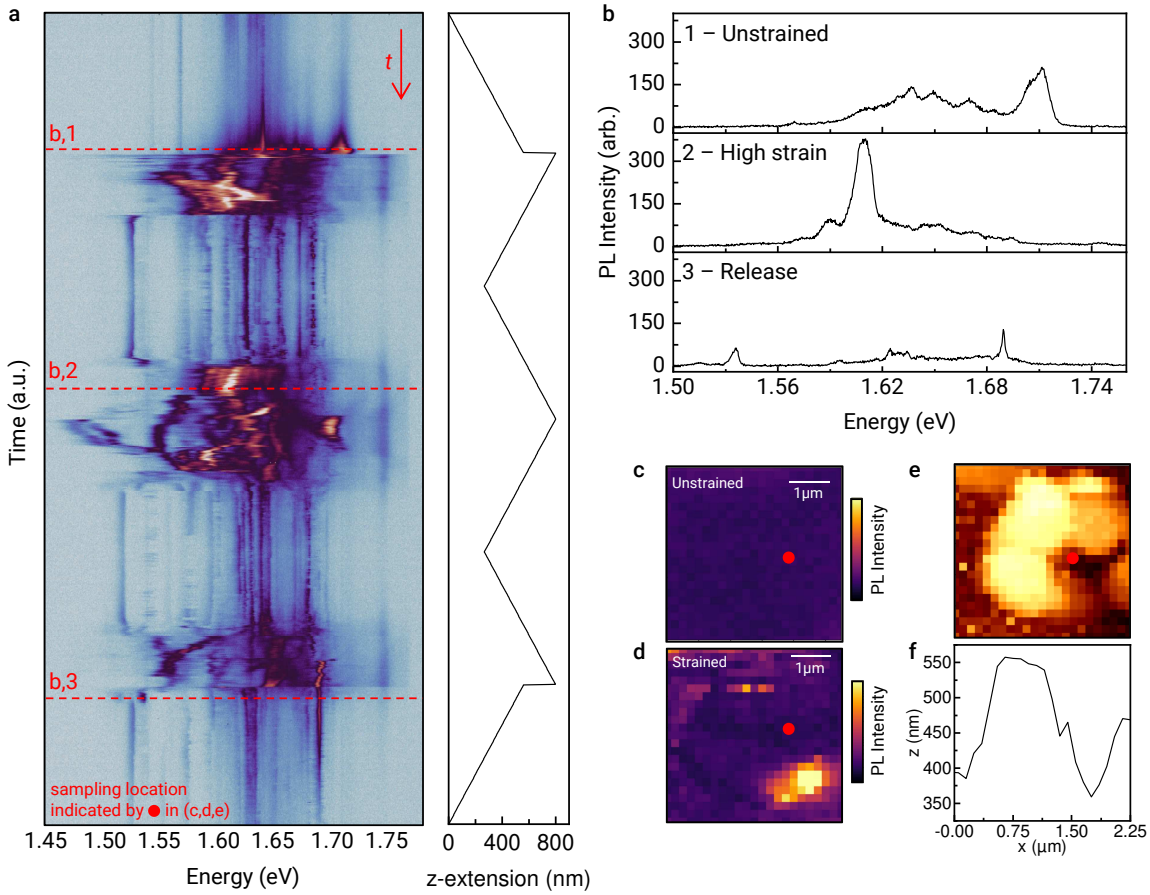

Figure 5.6 PL spectrum of inelastically strained WSe_2 a, PL spectrum of monolayer WSe_2 at different levels of localized strain. The right panel indicates extension of the vertical piezo corresponding to the applied force. As indicated, the same strain profile is applied three consecutive times before releasing the tip completely. **b,** PL spectra of monolayer WSe_2 (indicated in line-cuts in **a**) unstrained (1), under high localized strain (2) and after the final release (3). **c, d** Photoluminescence image of the sample surface before (c) and after (d) localized strain application. **e,** AFM-measured topography of the same area. **f,** Line-cut through the AFM image from left to right through the point of contact.

come degenerate with the first state at ∼1 % of strain [82] (this value is dependent on temperature and therefore only a rough estimate). According to [82], the KK'-exciton, whose zero-phonon line is energetically degenerate with D^0, hybridizes with the defect and thus not only is allowed to recombine, but gains multiple orders of magnitude in oscillator strength. While these findings suggest that the KK'-exciton is the main contributor to the increase in PL, the hybridization between the defect-related states and D^0 has to be taken into account as well. In fact, for strong straining with a tip, it was found that the polarization behavior of the strained spectra suggests strong contributions from normally z-polarized excitons [60].

5.3.4 Inelastic strain

The next step was to apply higher force beyond the range of elasticity through larger extensions of the piezo scanner (see Fig. 5.6). Upon initial approach (see Fig. 5.6a) the spectral response behaved as before. Next, upon a sudden (unintentionally steep) increase in piezo extension, the spectrum changed substantially. PL from X^0 disappeared while the strained spectrum increased in intensity and now comprised of several spectral lines that experienced different sensitivity to additional strain, manifesting both in redshifts and blueshifts at various magnitudes. On retraction of the tip, the spectrum experienced another sudden modification, showing a collection of narrow, darker spectral lines, some of which experienced spectral and temporal jitter consistent with the formation of strain-induced localized emitters. Upon repeated approaches, the spectrum changed again, displaying bright PL of differentially shifting features as observed during the first approach. This spectrum, while similar in behavior, showed distinct differences between consecutive approaches with various features appearing and disappearing in sharp transitions. Fig. 5.6b shows a comparison between the unstrained spectrum, the brightest peak at high strain and the spectrum upon final release of the tip at the end of the force-curve. The unstrained spectrum (1) showed strong luminescence of X^0 and broader, low intensity features. The brightest feature in the series (2) was located at 1.61 eV and showed a redshift at increasing strain Further, this peak was only observed upon contact between tip and sample. The spectrum on retraction (3) showed generally lower PL intensity and a collection of narrow peaks as described before. After the completion of the force curve, the area around the point of contact was raster-scanned through the tip to obtain a high resolution PL image of the sample region (see 5.6c,d,e,f) as well as information on the topography from the force feedback. The lateral step-size was chosen to be 85 nm while keeping the tip-sample distance constant using FM feedback. When comparing the PL intensity

before and after inelastic straining, the appearance of a bright spot close to the point of contact in the energy range of the previously mentioned bright feature between 1.60 and 1.61 eV was observed (see Fig. 5.6c,d). The lateral distribution of intensity showed that this feature is smaller than the lateral resolution of the system, suggesting a single localized emitter or group of emitters (also see Section 5.2). The location of this emitter was not centered at the site of the strain measurement itself but was instead displaced by approximately 1 μm. When viewed through the simultaneously recorded topography (see Fig. 5.6e,f), the point of contact appeared as a depression compared to the surrounding area and is encircled by a ring-shaped deformation that extended up to over 300 nm above the height in the center. This suggests that upon high strain the hBN-WSe_2 heterostructure was perforated by the diamond tip, forcing the elastic material to be displaced sidewards leaving a hole surrounded by elevated wrinkles. The tips lateral diameter of 300 nm at the facet is compatible with that assumption. A comparison of the topography to the PL image shows, that the bright emitter is located in a ridge next to the point of contact. This strain-mediated emission from wrinkled WSe_2 monolayers is also found in other experiments that show these can host bright single photon emitters [61].

5.4 Summary and conclusion

In summary, a combination of a diamond tip mounted to a QTF and a cryogenic confocal microscope was utilized to study the PL spectrum of ML-WSe_2 under local strain. Under tensile strain, the spectrum experienced a redshift and, most notably, a relative increase in intensity of the spin-forbidden dark exciton D_0. The evolution of this peak is explained by the hybridization of D^0 and the momentum-indirect KK'-exciton with dark states originating from selenium vacancies, as previously observed, in homogeneously strained WSe_2 monolayers [82]. Upon increased force, the spectrum changed permanently and showed several peaks of differing intensity and varying degrees of temporal and spectral jitter. Furthermore, coupled AFM and PL measurements through the tip revealed that these features have their origin in wrinkles introduced by the tip piercing through the sample.

6 Summary and perspectives

Within this thesis, mono- and bilayers of WSe_2 and WS_2 encapsulated in hBN were studied by means of optical spectroscopy. Samples for this work were prepared using mechanical exfoliation and viscoelastic stamping. Charge control was established using the doped silicon substrate as a gate or few-layer graphene which was directly integrated into the TMD/hBN heterostructure. Suspended monolayer samples were fabricated from a patterened bottom hBN layer, which was etched using reactive ion etching.

The first experiment described in Chapter 4 focused on the study of the PL and DR spectrum of mono- and bilayer WSe_2 in magnetic field. The device performance, using the substrate for doping control, allowed tuning of the charge carrier density between the neutral and negative regime. The magnetic shift of the entire spectrum was measured in different circular bases and quantified by the exciton g-factor. These values were complemented by a numerical model based on density functional theory (DFT), which was used to predict g-factors at multiple points in the Brillouin zone. First, this included the K and K' points, resulting in values for the bright exciton X^0 and the spin-dark exciton D^0 which were in agreement with measurements in this work and other experiments. Further, g-factors for spin-like and spin-unlike momentum-indirect configurations of the two valleys were predicted as well as momentum-indirect excitons involving the Q-valleys in the conduction band and the Γ-valley in the valence band. The range of g-factors for Q-momentum excitons and momentum-indirect excitons involving K and K' turned out to be too similar to be distinguished in the spectrum. The comparatively low values for Γ-momentum excitons however was used to rule out these exciton species in the bilayer spectrum and narrow the assignment of spectral lines down to intralayer and interlayer excitons between K/K' and Q.

Next, a monolayer of WS_2, embedded into a $WS_2/MoSe_2$ heterostructure was studied spectroscopically at different charge carrier densities. The improved field effect structure of this device, using few layer graphene instead of silicon, enabled a wide ranging of charge carrier densities including positive doping as well as several distinct negative doping regimes, previously not studied in WS_2. The spectrum at these dop-

ing levels behaved almost identical to WSe_2, confirming that, apart from a different band gap, the similarities of the two materials also hold at high doping levels.

The third experiment, described in Chapter 5, focused to study the spectrum of locally strained monolayer WSe_2 using a quartz tuning fork atomic force microscope. The sample for this experiment consisted of an hBN-encapsulated WSe_2 monolayer, that was partially suspended over air holes etched into the bottom hBN layer using reactive ion etching. A transparent diamond tip, attached to a quartz tuning fork, was placed in the focus of a long working distance objective, which allowed to apply force to the sample while studying the optical spectrum at the same time. The tip with a length of 8 µm further acted as an aperture, improving the spatial resolution of the microscope by a factor of ~ 2.5. By bringing the tip in contact with the sample, localized strain was applied over suspended parts of the sample while recording the spectrum. The spectrum showed a red-shifting behavior with the energy of the bright exciton X^0 shifting by approximately 50 meV, indicating moderate tensile strain. It was found that this shift was limited by the depth of the air hole and that at this point, the modification of the spectrum was reversible, leaving the potential of higher strain by improving the design of the sample. Apart from the red shift, the spectrum showed rising photoluminescence at increasing strain. This effect is in agreement with previous work on globally, biaxially strained monolayer WSe_2 [82] and coincides with the dark exciton D^0 being red-shifted to the energy of defect-related states, that are shown to be less sensitive to strain and thus are able to hybridize when overlapping with D^0. At higher force, the tip irreversibly deformed the sample around the point of contact and modified the spectrum to show a set of narrow spectral lines. Subsequent combined AFM and PL measurements revealed that the tip action on the sample resulted in pronounced wrinkles, that host regions of bright photoluminescence. The dimensions of these emitters were shown to be smaller than the resolution limit of the microscopy system.

In conclusion, the studies contained in this work used various spectroscopic methods to gain a deeper insight into excitonic processes of tungsten-based 2D materials and further provide interesting directions for future research. The DFT-based numerical model to determine exciton g-factors provided a powerful tool to interpret the spectrum of WSe_2, but the corresponding framework can be translated to other systems as well. A similar model was for example used successfully in the study of moiré excitons in $WSe_2/MoSe_2$ heterobilayers [153].

The technique used for strain measurements in this work provides a versatile tool for spectroscopic studies that is not limited to WSe_2 monolayers. While a lot of techniques

have been deployed to apply strain on 2D TMDs in conjunction to spectroscopy, many of them were limited to ambient temperatures [75, 78–80, 154] or didn't allow strain control in-situ [81]. One study achieved a high range of strain at cryogenic temperatures by embedding WSe_2 in a microdrum and using a gate to apply strain electrically [82]. A drawback of this otherwise elegant approach is the reliance on charging the sample to apply force, prohibiting the study of strain and doping separately. Recently a study succeeded to apply local strain using a standard AFM tip at cryogenic temperatures, but relied on the suspension of the sample on a TEM-grid [155], complicating sample design and assembly. Another recent experiment similar in scope to the work in this thesis used a tapered fiber to apply strain to a suspended sample [60]. This technique allows spectroscopy and application of strain simultaneously similar to our experiment. An advantage of our approach however is the ability to perform AFM measurements in-situ and the ability to seamlessly switch between using the tip and a conventional microscopy system.

Irrespective of the specific technique, there is still a high potential for future discoveries with regards to strain in 2D materials. For example, most previously referenced studies as well as the experiments for this thesis focussed on monolayer 2D materials only. However, a great deal of interest in the study of 2D materials in general focuses on emerging phenomena in van der Waals heterostructures[156]. Studies achieving tunable strain on these types of devices is very sparse with first steps being done in experiments done at room temperature [157]. Expanding our technique to suspended $WS_2/MoSe_2$ heterostructures in a dual gate device was explored towards the end of this thesis and would be a logical next step.

Danksagung

An dieser Stelle, kurz vor 1 Uhr Nachts, nach fast sechs Jahren Doktorarbeit, ist es an der Zeit, all denen zu danken, die mich auf diesem Weg begleitet und ihn erst möglich gemacht haben. An erster Stelle Alex Högele, der mir die letzten sieben Jahre eine wissenschaftliche Heimat gegeben hat und ohne dessen Unterstützung ich nicht an diesen Punkt gekommen wäre. Stephan Manus, der die meisten essentiellen Geräte meiner Doktorarbeit entwickelt, gebaut oder repariert hat (inklusive des "Manus Grunt Master") und mir mehr als einmal einen Grundkurs in Elektrotechnik gegeben hat. Patrick Maletinsky für die lange Unterstützung meines AFM-Projekts und Jodok Happacher für seine Masterarbeit, seine technische Unterstützung und vermutlich unzählige Stunden bei der Fabrikation von Spitzen. Anvar Baimuratov und meinen Koautoren Nikita Tepliakov und Stanislav Kruchinin für ihre theoretischen Berechungen. Victor Funk, von dem ich nicht nur das Basteln mit Klebeband und Stempel sowie Spektroskopie gelernt habe, sondern der auch während der gesamten Doktorarbeit in meinem Team war, sei es beim Bauen einer Glovebox, der Fabrikation von Proben oder der Versorgung des Lehrstuhls mit koffeinhaltigen Heißgetränken. Michael Förg, ohne dessen Initative die Nanophotonics Gaming Group nicht endstanden wäre, die die Ausgangssperre in der Pandemie um einiges erträglicher machte. Jessica Lindlau, für viel viel Geduld und ihre gute Betreuung. Andre Neumann, unter anderem für das Rätsel des Gerrymandering-Algorithmus, was mich jetzt seit Jahren begleitet. Johannes Scherzer, meinem ersten erfolgreichen Latte-Art Lehrling, für viele entspannte Gespräche über Musik. Borislav Polovnikov für viele wunderbare und entspannte Gespräche über vermutlich alles andere. Farsane Tabataba-Vakili für viele gute Spieleabende und die Unterstützung wenn ich gerade keine Lust auf die Mensa hatte. Anvar Baimuratov für Einblicke in russischen Rap. Lukas Krelle für die geteilte Leidenschaft für guten Kaffee und viele leckere Sommerrollen. Jonathan Noé für die langen, ausschweifenden Gespräche beim morgendlichen Cappuccino (mit Zucker). Manuel Nutz für vieles was mit Physik, Technik und genereller Erklärerei zutun hat, aber vor allem für die Geschichte des magischen Schalters. Jonas Göser für all die zufälligen Programmierdisukssionen, wenn ich gerade Ablenkung vom harten

Laboraltag brauchte. Lukas Husel, der immer als Joker zur Seite stand, wenn es im Labor eine Sackgasse gab. Hyowon Jeong und Markus Fitz, mit denen ich das erste mal Lehrer spielen durfte. Matthias Lösche für die Rohfassung seines ersten Albums. Franzi für all deine seelische Unterstützung bis an diesen Punkt, für Figure 3.1 und für das Mysterium des explodierenden Wafers! Christian Mohl für sein unermütliches Streben nach Perfektion und das Durchhalten trotz durchgebrannter Gates und platzender Proben. Zhijie Li und Shen Zhao für entspannte Abende bei Suppe, Wurst und chinesischem Reality TV. Subhradeep Misra für ausnahmslos gute Laune. Ismail Bilgin, ohne den hier nichts wachsen würde. Anna Rupp für die Hilfe bei meinen Ausschweifungen in die Pigmentchemie am Elektronenmikroskop. Tim Wedl, mit dem ich noch etwas ausgiebiger über die Fliegerei unterhalten muss. Julian Trapp für die Gen-Z Perspektive im Büro und den stetigen Nachschub an frisch gewachsenem Material. Arthur Ermatov für all die guten Gespräche bei Kaffee, Kakao, selbst gemachtem Pesto, Sauce Hollondaise, Sushi, Pizza und vielem mehr. Samarth Vadia, mit mir verbunden durch unsere gemeinsame Zeit in Russland und unsere geteilte Leidenschafft für die Pflege der elbischen Sprache. Bert Lorenz, Dayse Ferreira e Silva und Martina Jüttner dafür, dass der Lehrstuhl in den gesamten sechs Jahren nicht im Chaos versunken ist. Anton Heindl, für all die technische Unterstützung, insbesondere, wenn es mal schneller gehen musste als die Werkstatt. Philipp Altpeter, dem unermütlichen Beschützer des Reinraums. Christian Obermayer, dem ich noch eine Probe Manganblau geben muss. Dem ganzen Team von Linque: Tibor, Lukas, Lucas, Laszlo, Julius, Anna und Deniz. Und am Ende meinen Eltern, meiner Familie, meinen Freunden und all den lieben Menschen, die mir in der langen Zeit Rückendeckung gegeben haben.

Bibliography

1. Kroemer, H. Quasi-Electric Fields and Band Offsets: Teaching Electrons New Tricks (2000).
2. Novoselov, K. S. *et al.* Electric Field Effect in Atomically Thin Carbon Films. *Science* **306,** 666–669 (Oct. 22, 2004).
3. Geim, A. K. & Novoselov, K. S. The rise of graphene. *Nat. Mater.* **6,** 183–191 (Mar. 2007).
4. Bolitin, K. I., Ghahari, F., Shulman, M. D., Stormer, H. L. & Kim, P. Observation of the fractional quantum Hall effect in graphene. *Nature* (2009).
5. Moses, A. J. The Crystallization of Molybdenite. *Am. J. Sci.* (1904).
6. Dickinson, R. G. & Pauling, L. The crystal structure of molybdenite. *J. Am. Chem. Soc.* **45,** 1466–1471 (June 1, 1923).
7. Winer, W. O. Molybdenum disulfide as a lubricant: A review of the fundamental knowledge. *Wear* **10,** 422–452 (Nov. 1, 1967).
8. Kam, K. K. & Parkinson, B. A. Detailed photocurrent spectroscopy of the semiconducting group VIB transition metal dichalcogenides. *J. Phys. Chem.* **86,** 463–467 (Feb. 1, 1982).
9. Hovel, H. J. Photovoltaic materials and devices for terrestrial solar energy applications. *Sol. Energy Mater.* **2,** 277–312 (Apr. 1, 1980).
10. Roxlo, C. B., Chianelli, R. R., Deckman, H. W., Ruppert, A. F. & Wong, P. P. Bulk and surface optical absorption in molybdenum disulfide. *J. Vac. Sci. A* **5,** 555–557 (July 1, 1987).
11. Mattheiss, L. F. Band Structures of Transition-Metal-Dichalcogenide Layer Compounds. *Phys. Rev. B* **8,** 3719–3740 (Oct. 15, 1973).
12. Mak, K. F., Lee, C., Hone, J., Shan, J. & Heinz, T. F. Atomically Thin MoS_2: A New Direct-Gap Semiconductor. *Phys. Rev. Lett.* **105,** 136805 (Sept. 24, 2010).
13. Splendiani, A. *et al.* Emerging Photoluminescence in Monolayer MoS_2. *Nano Lett.* **10,** 1271–1275 (Apr. 14, 2010).

14. Zhao, W. *et al.* Evolution of Electronic Structure in Atomically Thin Sheets of WS_2 and WSe_2. *ACS Nano* **7,** 791–797 (Jan. 22, 2013).
15. Chernikov, A. *et al.* Exciton Binding Energy and Nonhydrogenic Rydberg Series in Monolayer WS_2. *Phys. Rev. Lett.* **113** (Aug. 13, 2014).
16. Hanbicki, A., Currie, M., Kioseoglou, G., Friedman, A. & Jonker, B. Measurement of high exciton binding energy in the monolayer transition-metal dichalcogenides WS_2 and WSe_2. *Solid State Commun.* **203,** 16–20 (Feb. 2015).
17. Mak, K. F., McGill, K. L., Park, J. & McEuen, P. L. The valley Hall effect in MoS_2 transistors. *Science* **344,** 1489–1492 (June 27, 2014).
18. Schaibley, J. R. *et al.* Valleytronics in 2D materials. *Nat. Rev. Mater.* **1,** 16055 (2016).
19. Novoselov, K. S., Mishchenko, A., Carvalho, A. & Neto, A. H. C. 2D materials and van der Waals heterostructures. *Science* **353,** aac9439 (July 29, 2016).
20. Zhang, X.-X., You, Y., Zhao, S. Y. F. & Heinz, T. F. Experimental Evidence for Dark Excitons in Monolayer WSe_2. *Phys. Rev. Lett.* **115,** 257403 (25 Dec. 2015).
21. Zhang, X.-X. *et al.* Magnetic brightening and control of dark excitons in monolayer WSe_2. *Nat. Nanotechnol.* **12,** 883–888 (Sept. 2017).
22. Pletikosić, I., Ali, M. N., Fedorov, A. V., Cava, R. J. & Valla, T. Electronic Structure Basis for the Extraordinary Magnetoresistance in WTe_2. *Phys. Rev. Lett.* **113,** 216601 (Nov. 19, 2014).
23. Li, T. & Galli, G. Electronic Properties of MoS_2 Nanoparticles. *J. Phys. Chem. C* **111,** 16192–16196 (Nov. 1, 2007).
24. Gilleo, M. A., Bailey, P. T. & Hill, D. E. Free-Carrier and Exciton Recombination Radiation in GaAs. *Phys. Rev.* **174,** 898–905 (Oct. 15, 1968).
25. Spitzer, W. G. & Whelan, J. M. Infrared Absorption and Electron Effective Mass in *n*-Type Gallium Arsenide. *Phys. Rev.* **114,** 59–63 (Apr. 1, 1959).
26. Bonnet, D. & Meyers, P. Cadmium-telluride—Material for thin film solar cells. *J. Mater. Res.* **13,** 2740–2753 (Oct. 1, 1998).
27. Nathan, M. I., Dumke, W. P., Burns, G., Dill, F. H. & Lasher, G. Stimulated Emission of Radiation from GaAs *p-n* Junctions. *Appl. Phys. Lett.* **1,** 62–64 (Nov. 1962).
28. Quist, T. M. *et al.* Semiconductor Maser of GaAs. *Appl. Phys. Lett.* **1,** 91–92 (Dec. 1962).
29. Hall, R. N., Fenner, G. E., Kingsley, J. D., Soltys, T. J. & Carlson, R. O. Coherent Light Emission From GaAs Junctions. *Phys. Rev. Lett.* **9,** 366–368 (Nov. 1, 1962).

30. Bohr, N. I. On the constitution of atoms and molecules. *London Edinburgh Philos. Mag. & J. Sci.* **26,** 1–25 (July 1, 1913).

31. Yang, X. L., Guo, S. H., Chan, F. T., Wong, K. W. & Ching, W. Y. Analytic solution of a two-dimensional hydrogen atom. I. Nonrelativistic theory. *Phys. Rev. A* **43,** 1186–1196 (Feb. 1, 1991).

32. Lindlau, J. *Optical spectroscopy of charge-tunable atomically thin semiconductors at cryogenic temperatures* PhD thesis (München, 2019).

33. Beal, A. R. & Hughes, H. P. Kramers-Kronig analysis of the reflectivity spectra of 2H-MoS_2, 2H-$MoSe_2$ and 2H-$MoTe_2$. *J. Phys. C* **12,** 881 (Mar. 1979).

34. Gao, L., Lemarchand, F. & Lequime, M. Exploitation of multiple incidences spectrometric measurements for thin film reverse engineering. *Opt. Express* **20,** 15734–15751 (July 2, 2012).

35. Laturia, A., Van de Put, M. L. & Vandenberghe, W. G. Dielectric properties of hexagonal boron nitride and transition metal dichalcogenides: from monolayer to bulk. *npj 2D Mater Appl* **2,** 6 (Mar. 8, 2018).

36. Lynch, J., Guarneri, L., Jariwala, D. & Van de Groep, J. Exciton resonances for atomically-thin optics. *J. Appl. Phys.* **132,** 091102 (Sept. 7, 2022).

37. Nam, S. B. *et al.* Free-exciton energy spectrum in GaAs. *Phys. Rev. B* **13,** 761–767 (Jan. 15, 1976).

38. Lindlau, J. *et al.* Identifying optical signatures of momentum-dark excitons in transition metal dichalcogenide monolayers. *arXiv:1710.00988* [*cond-mat*] (Oct. 3, 2017).

39. Lindlau, J. *et al.* The role of momentum-dark excitons in the elementary optical response of bilayer WSe_2. *Nat. Commun.* **9,** 2586 (July 3, 2018).

40. Gunawan, O., Habib, B., De Poortere, E. P. & Shayegan, M. Quantized conductance in an AlAs two-dimensional electron system quantum point contact. *Phys. Rev. B* **74,** 155436 (Oct. 30, 2006).

41. Yao, W., Xiao, D. & Niu, Q. Valley-dependent optoelectronics from inversion symmetry breaking. *Phys. Rev. B* **77,** 235406 (June 4, 2008).

42. Rycerz, A., Tworzydło, J. & Beenakker, C. W. J. Valley filter and valley valve in graphene. *Nat. Phys.* **3,** 172–175 (Mar. 2007).

43. Xiao, D., Yao, W. & Niu, Q. Valley-Contrasting Physics in Graphene: Magnetic Moment and Topological Transport. *Phys. Rev. Lett.* **99,** 236809 (Dec. 7, 2007).

44. Cao, T. *et al.* Valley-selective circular dichroism of monolayer molybdenum disulphide. *Nat. Commun.* **3,** 887 (June 6, 2012).

45. Zeng, H., Dai, J., Yao, W., Xiao, D. & Cui, X. Valley polarization in MoS_2 monolayers by optical pumping. *Nat. Nanotechnol.* **7,** 490–493 (Aug. 2012).

46. Xiao, D., Liu, G.-B., Feng, W., Xu, X. & Yao, W. Coupled Spin and Valley Physics in Monolayers of MoS_2 and Other Group-VI Dichalcogenides. *Phys. Rev. Lett.* **108** (May 7, 2012).

47. Jones, A. M. *et al.* Optical generation of excitonic valley coherence in monolayer WSe_2. *Nat. Nanotechnol.* **8,** 634–638 (Sept. 2013).

48. Xu, X., Yao, W., Xiao, D. & Heinz, T. F. Spin and pseudospins in layered transition metal dichalcogenides. *Nat. Phys.* **10,** 343–350 (May 2014).

49. Kumar, N. *et al.* Second harmonic microscopy of monolayer MoS_2. *Phys. Rev. B* **87,** 161403 (Apr. 15, 2013).

50. Malard, L. M., Alencar, T. V., Barboza, A. P. M., Mak, K. F. & de Paula, A. M. Observation of intense second harmonic generation from MoS_2 atomic crystals. *Phys. Rev. B* **87,** 201401 (May 13, 2013).

51. Zeng, H. *et al.* Optical signature of symmetry variations and spin-valley coupling in atomically thin tungsten dichalcogenides. *Sci. Rep.* **3,** 1608 (Apr. 11, 2013).

52. Wang, G. *et al.* Giant Enhancement of the Optical Second-Harmonic Emission of WSe_2 Monolayers by Laser Excitation at Exciton Resonances. *Phys. Rev. Lett.* **114,** 097403 (Mar. 4, 2015).

53. Alidoust, N. *et al.* Observation of monolayer valence band spin-orbit effect and induced quantum well states in MoX2. *Nat. Commun.* **5,** 4673 (Aug. 22, 2014).

54. Kormányos, A. *et al.* Monolayer MoS_2: Trigonal warping, the Γ valley, and spin-orbit coupling effects. *Phys. Rev. B* **88,** 045416 (July 9, 2013).

55. Robert, C. *et al.* Fine structure and lifetime of dark excitons in transition metal dichalcogenide monolayers. *Phys. Rev. B* **96** (Oct. 9, 2017).

56. Robert, C. *et al.* Measurement of the spin-forbidden dark excitons in MoS_2 and $MoSe_2$ monolayers. *Nat. Commun.* **11,** 4037 (Aug. 12, 2020).

57. Hsu, W.-T. *et al.* Evidence of indirect gap in monolayer WSe_2. *Nat. Commun.* **8** (Dec. 2017).

58. Deilmann, T. & Thygesen, K. S. Finite-momentum exciton landscape in mono- and bilayer transition metal dichalcogenides. *2D Mater.* **6,** 035003 (Apr. 5, 2019).

59. Srivastava, A. *et al.* Optically active quantum dots in monolayer WSe_2. *Nat. Nanotechnol.* **10,** 491–496 (June 2015).

60. Gelly, R. J. *et al.* Probing dark exciton navigation through a local strain landscape in a WSe_2 monolayer. *Nat. Commun.* **13,** 232 (Jan. 11, 2022).

61. Iff, O. *et al.* Strain-Tunable Single Photon Sources in WSe_2 Monolayers. *Nano Lett.* **19,** 6931–6936 (Oct. 9, 2019).

62. Parto, K., Azzam, S. I., Banerjee, K. & Moody, G. Defect and strain engineering of monolayer WSe_2 enables site-controlled single-photon emission up to 150 K. *Nat. Commun.* **12,** 3585 (June 11, 2021).

63. Luo, Y., Liu, N., Li, X., Hone, J. C. & Strauf, S. Single photon emission in WSe_2 up 160 K by quantum yield control. *2D Mater.* **6,** 035017 (May 2019).

64. Sun, Y., Thompson, S. E. & Nishida, T. Physics of strain effects in semiconductors and metal-oxide-semiconductor field-effect transistors. *J. Appl. Phys.* **101,** 104503 (May 15, 2007).

65. Wee, C., Maikop, S. & Yu, C.-Y. Mobility-enhancement technologies. *IEEE Circuits Devices Mag.* **21,** 21–36 (May 2005).

66. Griffith, A. in (1921).

67. Hopcroft, M. A., Nix, W. D. & Kenny, T. W. What is the Young's Modulus of Silicon? *J. Microelectromech. S.* **19,** 229–238 (Apr. 2010).

68. Bertolazzi, S., Brivio, J. & Kis, A. Stretching and Breaking of Ultrathin MoS_2. *ACS Nano* **5,** 9703–9709 (Dec. 27, 2011).

69. Falin, A. *et al.* Mechanical Properties of Atomically Thin Tungsten Dichalcogenides: WS_2 , WSe_2 , and WTe_2. *ACS Nano* **15,** 2600–2610 (Feb. 23, 2021).

70. Peng, Z., Chen, X., Fan, Y., Srolovitz, D. J. & Lei, D. Strain engineering of 2D semiconductors and graphene: from strain fields to band-structure tuning and photonic applications. *Light Sci. Appl.* **9,** 190 (Nov. 23, 2020).

71. Midtvedt, D., Lewenkopf, C. H. & Croy, A. Strain–displacement relations for strain engineering in single-layer 2d materials. *2D Mater.* **3,** 011005 (Feb. 2016).

72. Tran, T. N., Dang, M. T., Tran, Q. H., Luong, T. T. & Dinh, V. A. Band valley modification under strain in monolayer WSe2. *AIP Adv.* **12,** 115023 (Nov. 2022).

73. Shi, H., Pan, H., Zhang, Y.-W. & Yakobson, B. I. Quasiparticle band structures and optical properties of strained monolayer MoS_2 and WS_2. *Phys. Rev. B* **87,** 155304 (Apr. 9, 2013).
74. Yang, C.-X., Zhao, X. & Wei, S.-Y. Manipulation of electronic structure in WSe_2 monolayer by strain. *Solid State Commun.* **245,** 70–74 (Nov. 1, 2016).
75. He, K., Poole, C., Mak, K. F. & Shan, J. Experimental Demonstration of Continuous Electronic Structure Tuning via Strain in Atomically Thin MoS_2. *Nano Lett.* **13,** 2931–2936 (June 12, 2013).
76. Hui, Y. Y. *et al.* Exceptional Tunability of Band Energy in a Compressively Strained Trilayer MoS_2 Sheet. *ACS Nano* **7,** 7126–7131 (Aug. 27, 2013).
77. Aslan, B., Deng, M. & Heinz, T. F. Strain tuning of excitons in monolayer WSe_2. *Phys. Rev. B* **98,** 115308 (Sept. 27, 2018).
78. Schmidt, R. *et al.* Reversible uniaxial strain tuning in atomically thin WSe_2. *2D Mater.* **3,** 021011 (June 2016).
79. Island, J. O. *et al.* Precise and reversible band gap tuning in single-layer $MoSe_2$ by uniaxial strain. *Nanoscale* **8,** 2589–2593 (Jan. 29, 2016).
80. Wang, Y. *et al.* Strain-induced direct–indirect bandgap transition and phonon modulation in monolayer WS_2. *Nano Res.* **8,** 2562–2572 (Aug. 1, 2015).
81. Ahn, G. H. *et al.* Strain-engineered growth of two-dimensional materials. *Nat. Commun.* **8,** 608 (Sept. 20, 2017).
82. Hernández López, P. *et al.* Strain control of hybridization between dark and localized excitons in a 2D semiconductor. *Nat. Commun.* **13,** 7691 (Dec. 12, 2022).
83. Branny, A., Kumar, S., Proux, R. & Gerardot, B. D. Deterministic strain-induced arrays of quantum emitters in a two-dimensional semiconductor. *Nat. Commun.* **8,** 15053 (May 22, 2017).
84. So, J.-P. *et al.* Electrically driven strain-induced deterministic single-photon emitters in a van der Waals heterostructure. *Sci. Adv.* **7,** eabj3176 (Oct. 20, 2021).
85. Förste, J. *et al.* Exciton g-factors in monolayer and bilayer WSe_2 from experiment and theory. *Nat. Commun.* **11,** 4539 (2020).
86. Aivazian, G. *et al.* Magnetic control of valley pseudospin in monolayer WSe_2. *Nat. Phys.* **11,** 148–152 (Feb. 2015).
87. Srivastava, A. *et al.* Valley Zeeman effect in elementary optical excitations of monolayer WSe_2. *Nat. Phys.* **11,** 141–147 (Feb. 2015).

88. Madéo, J. *et al.* Directly visualizing the momentum-forbidden dark excitons and their dynamics in atomically thin semiconductors. *Science* **370,** 1199–1204 (Dec. 4, 2020).

89. Koperski, M. *et al.* Optical properties of atomically thin transition metal dichalcogenides: observations and puzzles. *Nanophotonics* **6,** 1289–1308 (Nov. 1, 2017).

90. Landau, L. D. & Lifshitz, E. M. *Quantum Mechanics - 3rd Edition* (Jan. 1, 1981).

91. Bir, G. L., Pikus, G. E., Hensel, J. C. & Louvish, D. *Symmetry and strain-induced effects in semiconductors* trans. by Shelnitz, P. 484 pp. (Wiley, New York, 1974).

92. Roth, L. M., Lax, B. & Zwerdling, S. Theory of Optical Magneto-Absorption Effects in Semiconductors. *Phys. Rev.* **114,** 90–104 (Apr. 1, 1959).

93. Chen, J. *et al.* Chemical Vapor Deposition of High-Quality Large-Sized MoS_2 Crystals on Silicon Dioxide Substrates. *Adv. Sci* **3,** 1500033 (Aug. 2016).

94. Zhai, W. *et al.* Epitaxial growth of wafer-scale single-crystal transition metal dichalcogenide monolayers for future electronics. *Matter* **5,** 2405–2408 (Aug. 3, 2022).

95. Li, H. *et al.* A Universal, Rapid Method for Clean Transfer of Nanostructures onto Various Substrates. *ACS Nano* **8,** 6563–6570 (July 22, 2014).

96. Pizzocchero, F. *et al.* The hot pick-up technique for batch assembly of van der Waals heterostructures. *Nat. Commun.* **7,** 11894 (June 16, 2016).

97. Castellanos-Gomez, A. *et al.* Deterministic transfer of two-dimensional materials by all-dry viscoelastic stamping. *2D Mater.* **1,** 011002 (2014).

98. Huang, Y. *et al.* Reliable Exfoliation of Large-Area High-Quality Flakes of Graphene and Other Two-Dimensional Materials. *ACS Nano* **9,** 10612–10620 (Nov. 24, 2015).

99. Haslinger, F. *Characterization of Graphene, Semiconductor Monolayers and Heterostructures with complementary Imaging Techniques* BA thesis (LMU München, Nov. 2020).

100. Bing, D. *et al.* Optical contrast for identifying the thickness of two-dimensional materials. *Opt. Commun. Optoelectronics and Photonics Based on Two-dimensional Materials* **406,** 128–138 (Jan. 1, 2018).

101. Zhitao, H., Jinkui, C., Fantao, M. & Rencheng, J. Design and simulation of blue/violet sensitive photodetectors in silicon-on-insulator. *J. Semicond.* **30,** 104008 (Oct. 2009).

102. Bayer, B. E. *US Patent* 3971065A (1976).

103. Soman, M. *et al.* Non-linear responsivity characterisation of a CMOS Active Pixel Sensor for high resolution imaging of the Jovian system. *J. Inst.* **10,** C02012 (Feb. 2015).

104. Nemes-Incze, P., Osváth, Z., Kamarás, K. & Biró, L. P. Anomalies in thickness measurements of graphene and few layer graphite crystals by tapping mode atomic force microscopy. *Carbon* **46,** 1435–1442 (Sept. 1, 2008).

105. Xiao, Y., Zheng, W., Yuan, B., Wen, C. & Lanza, M. Highly Accurate Thickness Determination of 2D Materials. *Cryst. Res. Technol.* **56,** 2100056 (2021).

106. Funk, V. *Spectroscopy of momentum-dark excitons in layered semiconductors* PhD thesis (LMU München, 2017).

107. Purdie, D. G. *et al.* Cleaning interfaces in layered materials heterostructures. *Nat. Commun.* **9,** 5387 (Dec. 19, 2018).

108. Mohl, C. *Spectroscopy of Strain Effects in WSe_2 Monolayer and Doping Characteristics of $MoSe_2/WSe_2$* MA thesis (LMU München, 2022). 75 pp.

109. Nutz, M. *Optoelectronic Studies of Molybdenum Disulfide Field-Effect Devices* PhD thesis (LMU München, Nov. 17, 2014).

110. Förste, J. *Spectroscopy of gate-tunable thin films of tungsten-diselenide* MA thesis (LMU Munich, Munich, June 2018).

111. Günther, P., Fischer, U. C. & Dransfeld, K. Scanning near-field acoustic microscopy. *Appl. Phys. B* **48,** 89–92 (Jan. 1, 1989).

112. Rychen, J. *et al.* Operation characteristics of piezoelectric quartz tuning forks in high magnetic fields at liquid helium temperatures. *Rev. Sci. Instrum.* **71,** 1695–1697 (Apr. 1, 2000).

113. Rychen, J. *Combined Low-Temperature Scanning Probe Microscopy and Magneto-Transport Experiments for the Local Investigation of Mesoscopic Systems* PhD thesis (Zurich, 2001).

114. Karrai, K. & Grober, R. D. Piezoelectric tip-sample distance control for near field optical microscopes. *Appl. Phys. Lett.* **66,** 1842–1844 (Apr. 3, 1995).

115. Ruiter, A. G. T., Veerman, J. A., Werf, K. v. d. & Hulst, N. F. v. Dynamic behaviour of tuning fork shear-force feedback. *Appl. Phys. Lett.* **71,** 28–30 (1997).

116. Ruiter, A. G. T. *et al.* Tuning fork shear-force feedback. *Ultramicroscopy* **71,** 149–157 (Mar. 1, 1998).

117. Atia, W. A. & Davis, C. C. A phase-locked shear-force microscope for distance regulation in near-field optical microscopy. *Appl. Phys. Lett.* **70,** 405–407 (Jan. 27, 1997).

118. Maletinsky, P. *et al.* A robust scanning diamond sensor for nanoscale imaging with single nitrogen-vacancy centres. *Nat. Nanotechnol.* **7,** 320–324 (May 2012).

119. Grober, R. D. *et al.* Fundamental limits to force detection using quartz tuning forks. *Rev. Sci. Instrum.* **71,** 2776–2780 (July 1, 2000).

120. Gritsenko, I. A., Zadorozhko, A. A., Rudavskii, E. Y., Chagovets, V. K. & Sheshin, G. A. Transition to Turbulence and Critical Velocity in Superfluid Solution of 3He in 4He. *J. Low Temp. Phys.* **158,** 450–455 (Feb. 1, 2010).

121. Bradley, L., Atkinson, G. J., Horsfall, A. B. & Donaghy-Spargo, C. M. Evaluating Suitable Semiconducting Materials for Cryogenic Power Electronics. *J. Eng.* **2019** (Apr. 4, 2019).

122. Hedrich, N., Rohner, D., Batzer, M., Maletinsky, P. & Shields, B. J. Parabolic Diamond Scanning Probes for Single-Spin Magnetic Field Imaging. *Phys. Rev. Appl.* **14,** 064007 (Dec. 2, 2020).

123. Appel, P. *et al.* Fabrication of all diamond scanning probes for nanoscale magnetometry. *Rev. Sci. Instrum.* **87,** 063703 (June 2016).

124. You, Y. *et al.* Observation of biexcitons in monolayer WSe_2. *Nat. Phys.* **11,** 477–481 (June 2015).

125. Barbone, M. *et al.* Charge-tuneable biexciton complexes in monolayer WSe_2. *Nat. Commun.* **9,** 3721 (Dec. 2018).

126. Steinhoff, A. *et al.* Biexciton fine structure in monolayer transition metal dichalcogenides. *Nat. Phys.* **14,** 1199–1204 (Dec. 2018).

127. Li, Z. *et al.* Revealing the biexciton and trion-exciton complexes in BN encapsulated WSe_2. *Nat. Commun.* **9,** 3719 (Dec. 2018).

128. Mak, K. F. *et al.* Tightly bound trions in monolayer MoS_2. *Nat. Mater.* **12,** 207–211 (2013).

129. Courtade, E. *et al.* Charged excitons in monolayer WSe_2: Experiment and theory. *Phy. Rev. B* **96,** 085302 (2017).

130. Zhou, Y. *et al.* Probing dark excitons in atomically thin semiconductors via near-field coupling to surface plasmon polaritons. *Nat. Nanotechnol.* **12,** 856–860 (2017).

131. Wang, G. *et al.* In-Plane Propagation of Light in Transition Metal Dichalcogenide Monolayers: Optical Selection Rules. *Phys. Rev. Lett.* **119** (July 26, 2017).

132. Liu, E. *et al.* Gate tunable dark trions in monolayer WSe_2. *Phys. Rev. Lett.* **123,** 027401 (July 9, 2019).

133. Li, Z. *et al.* Direct Observation of Gate-Tunable Dark Trions in Monolayer WSe_2. *Nano Lett.* **19,** 6886–6893 (Oct. 2019).

134. Liu, E. *et al.* Valley-selective chiral phonon replicas of dark excitons and trions in monolayer WSe_2. *Phys. Rev. Research* **1,** 032007 (Oct. 25, 2019).

135. He, M. *et al.* Valley Phonons and Exciton Complexes in a Monolayer Semiconductor. *arXiv:2001.01769* [*cond-mat*] (Jan. 6, 2020).

136. Wang, G. *et al.* Magneto-optics in transition metal diselenide monolayers. *2D Mater.* **2,** 034002 (June 2015).

137. Mitioglu, A. A. *et al.* Optical Investigation of Monolayer and Bulk Tungsten Diselenide (WSe_2) in High Magnetic Fields. *Nano Lett.* **15,** 4387–4392 (July 8, 2015).

138. Stier, A. V. *et al.* Magnetooptics of Exciton Rydberg States in a Monolayer Semiconductor. *Phys. Rev. Lett.* **120,** 057405 (Feb. 1, 2018).

139. Koperski, M. *et al.* Orbital, spin and valley contributions to Zeeman splitting of excitonic resonances in $MoSe_2$, WSe_2 and WS_2 Monolayers. *2D Mater.* **6,** 015001 (Oct. 2018).

140. Molas, M. R. *et al.* Brightening of dark excitons in monolayers of semiconducting transition metal dichalcogenides. *2D Mater.* **4,** 021003 (2017).

141. Van Tuan, D., Jones, A. M., Yang, M., Xu, X. & Dery, H. Virtual Trions in the Photoluminescence of Monolayer Transition-Metal Dichalcogenides. *Phys. Rev. Lett.* **122,** 217401 (May 2019).

142. Arora, A. *et al.* Zeeman spectroscopy of excitons and hybridization of electronic states in few-layer WSe_2, $MoSe_2$ and $MoTe_2$. *2D Mater.* **6,** 015010 (Nov. 2018).

143. Dias, A. C., Qu, F., Azevedo, D. L. & Fu, J. Band structure of monolayer transition-metal dichalcogenides and topological properties of their nanoribbons: Next-nearest-neighbor hopping. *Phys. Rev. B* **98,** 075202 (Aug. 3, 2018).

144. Polovnikov, B. *et al. Coulomb-correlated states of moiré excitons and charges in a semiconductor moiré lattice* Sept. 29, 2022.

145. Polovnikov, B. *et al.* Field-Induced Hybridization of Moiré Excitons in $MoSe_2/WS_2$ Heterobilayers. *Phys. Rev. Lett.* **132,** 076902 (7 Feb. 2024).

146. Vaclavkova, D. *et al.* Singlet and triplet trions in WS_2 monolayer encapsulated in hexagonal boron nitride. *arXiv:1802.05538* [*cond-mat*] (Feb. 15, 2018).

147. Le, L. V., Kim, T. J., Kim, Y. D. & Aspnes, D. E. Detection of the Biexciton of Monolayer WS_2 in Ellipsometric Data: A Maximum-Entropy Success. *Phys. Status Solidi B* **260,** 2200271 (2023).

148. Conway, M. A. *et al.* Direct measurement of biexcitons in monolayer WS_2. *2D Mater.* **9,** 021001 (Jan. 2022).

149. He, K. *et al.* Tightly Bound Excitons in Monolayer WSe_2. *Phys. Rev. Lett.* **113** (July 10, 2014).

150. Zinkiewicz, M. *et al. The effect of dielectric environment on the neutral and charged dark excitons in WSe_2 monolayer* Jan. 20, 2022.

151. Linhart, L. *et al.* Localized Intervalley Defect Excitons as Single-Photon Emitters in WSe_2. *Phys. Rev. Lett.* **123,** 146401 (14 Sept. 2019).

152. Linhart, L. *et al.* Electronic and Magnetic Properties of Defected Monolayer WSe_2 with Vacancies. *Nanoscale Res. Lett.* **129** (14 2019).

153. Förg, M. *et al.* Moiré excitons in $MoSe_2$-WSe_2 heterobilayers and heterotrilayers. *Nat. Commun.* (2021).

154. Hasz, K., Hu, Z., Park, K.-D. & Raschke, M. B. Tip-Enhanced Dark Exciton Nanoimaging and Local Strain Control in Monolayer WSe_2. *Nano Lett.* **23,** 198–204 (2023).

155. Moon, H. *et al.* Dynamic Exciton Funneling by Local Strain Control in a Monolayer Semiconductor. *Nano Lett.* **20,** 6791–6797 (2020).

156. Mak, K. F. & Shan, J. Semiconductor moiré materials. *Nat. Nanotechnol.* (2022).

157. Hu, J. *et al.* Moiré-Assisted Strain Transfer in Vertical van der Waals Heterostructures. *Nano Lett.* **23,** 10051–10057 (2023).